TECHNISCHE UNIVERSITÄT MÜNCHEN

Lehrstuhl für Informatikanwendungen in der Medizin & Augmented Reality

Quantification of Molecular Probes in Optoacoustic Tomography

Thomas Jetzfellner

Vollständiger Abdruck der von der Fakultät für Informatik der Technischen Universität München zur Erlangung des akademischens Grades eines

Doktors der Naturwissenschaften

genehmigten Dissertation.

Vorsitzender: Univ.-Prof. Dr. Johann Schlichter

Prüfer:

1. Univ.-Prof. Dr. Nassir Navab
2. Univ.-Prof. Vasilis Ntziachristos, Ph.D.
3. apl. Prof. Dr. Karl-Hans Englmeier, Ludwig-Maximilian-Universität München

Die Dissertation wurde am 29.09.2011 bei der Technischen Universität München

eingereicht und durch die Fakultät für Informatik am 03.05.2012

angenommen.

FAKULTÄT FÜR INFORMATIK

DER TECHNISCHEN UNIVERSITÄT MÜNCHEN

Ph.D. Thesis

Quantification of Molecular Probes in Optoacoustic Tomography

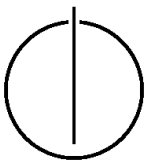

Author: Thomas Jetzfellner

Referees: Prof. Dr. Vasilis Ntziachristos (TUM)

Prof. Dr. Nassir Navab (TUM)

Prof. Dr. Karl Hans Englmeier (LMU)

Abstract

The detection and quantification of molecular targets by means of optical imaging modalities constitutes a highly topical research field of the last years. Utilizing light instead of hazardous ionizing radiation, which is typically used in X-ray based imaging methods, enables the investigation of effects of prototype drugs in small animals, following day by day the evolution of the disease *in vivo*. Until now, most applications kept focusing largely on microscopy due to the imposed depth limitation by light scattering and absorption. Among the available optical imaging techniques, optoacoustic tomography allows the visualization of biomarkers with never-before-seen performance. The imaging is performed by illuminating the object or region of interest with short high-power laser pulses, thus creating an instantaneous temperature elevation and thermal expansion within the target. The resulting broadband ultrasonic waves carry information on the underlying optical absorption coefficient variations, local light fluence, and thermoelastic properties of the object. They provide resolutions in the range of 20-200 μm and high contrast, and thus the ability for volumetric quantitative molecular imaging in human tissue, entire organs or small animals. In optoacoustic tomography the quantification of molecular targets is mainly biased by the light attenuation of the tissue, but also by the limitation of the sensitivity field of the employed ultra sound transducers. The methods I present are able to correct for these quantification problems, which typically arise in optoacoustic tomography. It is possible to detect molecular targets in tissue even in low concentrations. The performance of the employed algorithms is presented in simulations, as well as phantom and in an animal studies.

Für Julia, meinem Stern des Morgens

und des Abends

und

Für meine Eltern

und all die Menschen,

die mich auf dieser langen Reise begleitet haben.

„Great discoveries and improvements invariably involve the cooperation of many minds."

Alexander Graham Bell

Acknowledgement

Many people helped me helped me in working on the experiments or results presented in this thesis.

First of all, my deepest thanks go to my advisers, Prof. Dr. Vasilis Ntziachistons from the faculty of electrical engineering of the Technical University of Munich, Prof. Dr. Karl-Hans Englmeier from the medical faculty of the Ludwig Maximilian University Munich and Professor Dr. Nassir Navab from the faculty of informatics of the Technical University of Munich for accepting me as their PhD student, for enabling the creation of this work, and for giving me the freedom to proceed in any way possible without too many bound constraints. It was a great pleasure to work in the group of Dr. Daniel Razansky. For experimental support when animals were concerned, I have to acknowledge the help and expertise of Dr. Volodymyr Ermolayev and Sarah Glasl.

Among my colleagues I have to thank Marcus Freyer and Peter Hamm. Special thanks are going to Alexander Dima for his great first implementation of the interpolated model matrix inversion scheme. Additionally I have to thank my other office colleagues Miguel Angel Araque Caballero and Andreas Bühler for the inspiring discussions within the last years.

Last but not least I thank all other people who helped me in completing my thesis especially Dr. Willi Schork, Dr. Harry Höllig and Dr. Neal Burton.

Contents

1. Introduction

Optical imaging technologies are fundamental tools in biomedical research to detect and quantify molecular targets in tissue. They have a very broad field of application e.g. the general visual inspection, advanced microscopic techniques and deep tissue imaging [1]. The endogenous tissue contrast provides information about tissue anatomy, function and disease-related structural and physiological characteristics [1]. Information about molecular changes and gene expression are typically provided by the use of fluorescence and bioluminescence technologies, which can be visualized by direct and indirect imaging methods [1]. Optical modalities typically use light in the visual, the near infrared (NIR) or the infrared (IR) spectrum [1, 2]. Importantly, the use of light avoids the hazardous effects of other modalities that use ionizing radiation.

Among optical imaging techniques, microscopy is most common one used for imaging living tissue [1]. It provides very high resolution and can resolve objects of submicron size, which cannot be achieved by other imaging technologies like Magnet Resonance Imaging (MRI), Computed Tomography (CT), Positron Emission Tomography (PET) and Single-Photon Emission Computed Tomography (SPECT). The microscopic modality has the longest history among optical imaging techniques and was invented by Hans Janssen and Hans Lippershey in 1590 [3]. Microscopes are used to observe living cells, tumor cells, cells marked with molecular probes, blood vessels, lymphatic cells etc. *in vitro* and *in vivo* [1]. Additionally, hyper spectral approaches can be used to differentiate between oxy- and deoxygenated hemoglobin to provide functional information of the tissue. Although microscopy provides high resolution and good contrast, it is very limited in terms of imaging depth by light absorption and scattering. To overcome this limitation several advancements, which increased the penetration depth where introduced. State of the art confocal laser scanning microscopes (CLSM) can penetrate tissue up to depth of 100 μm [1, 2, 4]. However,

even the recent developments like the multiphoton laser scanning microscope (MPLSM) extend the penetration depth approximately 500 μm [1].

To overcome the limiting imaging depth of microscopy several approaches were developed. For example, optical coherence tomography (OCT) is able to detect the presence of a light scatterer in a depth between 0.5-2 mm [5, 6]. For deep tissue imaging up to several centimeters, light absorption is one of the main hindrances. This problem can be reduced by using near infrared (NIR) light excitation, which can penetrate the desired deep tissue regions[7, 8]. A second problem for imaging the whole body of small animals is the light scattering effect of tissue. The scattering of photons in tissue, also known as "photon diffusion", limits the application of optical imaging technologies for biomedical applications. Light loses its initial directionality due to photon diffusion, which limits the quantification ability and resolution [1]. Instead of imaging in the microscopic range, imaging in the macroscopic range can provide optical information of deep tissue regions. For example epi-illumination or transillumination imaging are photographic methods, which can be easily implemented [8].

By using more complex tomographic approaches and a sophisticated modeling of the light fluence in tissue, it is possible to increase resolution and improve quantification capabilities. One modality implementing this, is the fluorescence molecular tomography (FMT) [9-11]. Here a fluorescent target is excited at a specific wavelength. The fluorescent probe which is intended to be observed converts the light and emits it at a different wavelength. The difference between the maxima of excitation and emission spectra is called the stokes shift and must be known *a-priori*, because appropriate filters are necessary to extract the fluorescent signals. These signals are recorded tomographically at several detector positions. To reconstruct their origin within the measured object, inversion schemes are needed which account for the light propagation in tissue. These inversion problems are typically ill posed

and regularization algorithms are needed to provide an optimum performance. This can be done by providing *a-priori* information for the light fluence model used in the inversion. This information is typically provided by other modalities like computed tomography (CT) [12, 13]. To minimize the computational requirements, hybrid systems can be used where complex image registration is not required [13]. Ale *et al*. showed in [12] a good performance increase for FMT by using segmented CT data. Here, bone, heart and lungs were segmented and appropriate optical properties assigned for the light fluence model. The drawback of using the X-ray based CT is hazardous ionizing radiation. Besides FMT other optical tomographic approaches exist such as optical projection tomography (OPT) [14] or diffuse optical tomography (DOT) [15]. However, these modalities are limited in penetration depth, resolution or to *ex vivo* applications.

A new fast-evolving non-invasive imaging method providing high resolution and a good contrast for *in vivo* imaging is optoacoustic tomography (OAT) sometimes termed photoacoustic tomography (PAT) or thermoacoustic tomography (TAT) [16-19]. The imaging is performed by illuminating the object or region of interest with short high-power laser pulses, thus creating an instantaneous temperature elevation and a thermal expansion within the target. The subsequently generated broadband ultrasonic waves (typically in the 0.05–10 MHz range) carry information on the optical properties of the measured object like the underlying optical absorption coefficient variations, local light fluence, and thermoelastic properties of the object. These characteristics are used for spectral analysis [20-22] as well as in the field of non-destructive testing [21]. In the last decade OAT was broadly embraced in biomedical applications [17, 23-26]. For tomographic imaging, the optoacoustic responses are recorded around the object and reconstruction of the image is subsequently performed by using optoacoustic inversion schemes [17, 26-31]. The resulting reconstructed image represents local laser energy deposition within the object.

Conventional ultrasound imaging attains only a relative low contrast between different soft tissues. Optoacoustic tomography visualizes optical contrast which is significantly better in distinguishing different tissues and biomarkers, including oxygenated and deoxygenated forms of hemoglobin or endogenously or extrinsically administered absorbers. The weak scattering of ultrasonic waves in biological tissues provides a resolution similar to that achieved with ultra-sound; i.e. it can reach 20-200 μm depending on the penetration depth and the corresponding frequency spectrum employed. By combining optical contrast with ultrasonic diffraction-limited resolution, optoacoustics hold a great promise for future biomedical applications [32]. Besides intrinsic measurements of morphology and disease-related vascular changes [33-35], various contrast media approaches have also been developed for enhancement of detection sensitivity and specificity of the method, including dyes [36], light-absorbing nano-particles [37], and chromogenic substrates [38]. More recently, by applying illumination at several optical wavelengths, multispectral optoacoustic tomography (MSOT) was able to resolve distribution of fluorescent molecular agents [39] and fluorescent proteins [40] with both high sensitivity and spatial resolution in optically opaque organisms and tissues [32].

The quantification of molecular probes for full body small animal imaging is biased by the effect of light attenuation. Within tissue, light is typically attenuated by approximately two orders of magnitude per centimeter even for the NIR spectrum. The detection of low concentrations of probes in depths beyond 1 cm in tissue is very difficult without using methods to compensate for the light attenuation [32]. Additionally OAT reconstructions are usually very sensitive to various instrumentation and configuration-related parameters, such as the shape of an object‘s illumination, transducer layout, its frequency response and sensitivity fields, as well as laser source stability. If these deviations become substantial,

unquantified or generally erroneous reconstructions may arise. These effects depend on the characteristics of the optoacoustic systems [32].

This work focuses on methods, which provide the functionality to correct for the effect of light attenuation and inhomogeneous surface illumination. Most algorithms are based on the recently published interpolated-model-matrix inversion scheme (IMMI) for optoacoustic tomography [31] which will be discussed in detail in chapter 3. I developed a modified version of IMMI which is able to correct for the influence of inhomogeneous surface illumination for certain imaging scenarios. Furthermore, chapter 3.3 will give a discussion about the commonly used back-projection algorithm, which holds several drawbacks related to reconstruction artifacts for quantified imaging. Chapter 4 presents commonly used methods to correct for the influence of the light attenuation in optoacoustic tomography. Additionally, I adopted an iterative algorithm and developed a new ratiometric approach, both of which depict a rather satisfying performance. All the methods were tested experimentally on phantoms and on animals. The results are shown in chapter 5 and discussed in chapters 5 and 6.

2. Optoacoustic tomography

The following chapter will give a brief introduction about the light tissue interaction and describing the optoacoustic effect. For the general background a historical review of the developments since the discovery of the optoacoustic effect by Bell *et al*. [41] is given. It will be followed by an overview over modern optoacoustic systems and a discussion of quantification problems in optoacoustic tomography.

2.1 Light tissue interaction

The light spectrum observable by a typical human eye is only a small spectral band between 390 to 750 nm of the electromagnetic spectrum (Figure 1). This spectrum is called the visible spectrum, or visible light or simply light and corresponds to a frequency range of 400 – 790 THz. The characteristics of light can be described in the form of a waves and particles [1]. The visible light is a non-ionizing electromagnetic radiation, which under normal circumstances represents no danger for tissue. However, the use of a focused laser as a light source does pose a risk of harm depending on the energy used. The American National Standards Institute (ANSI) defined the maximal permissible exposure (MPE) for human skin to 20 mJ/cm^2 for a single nanosecond pulse at wavelengths within the visible light spectrum[19].

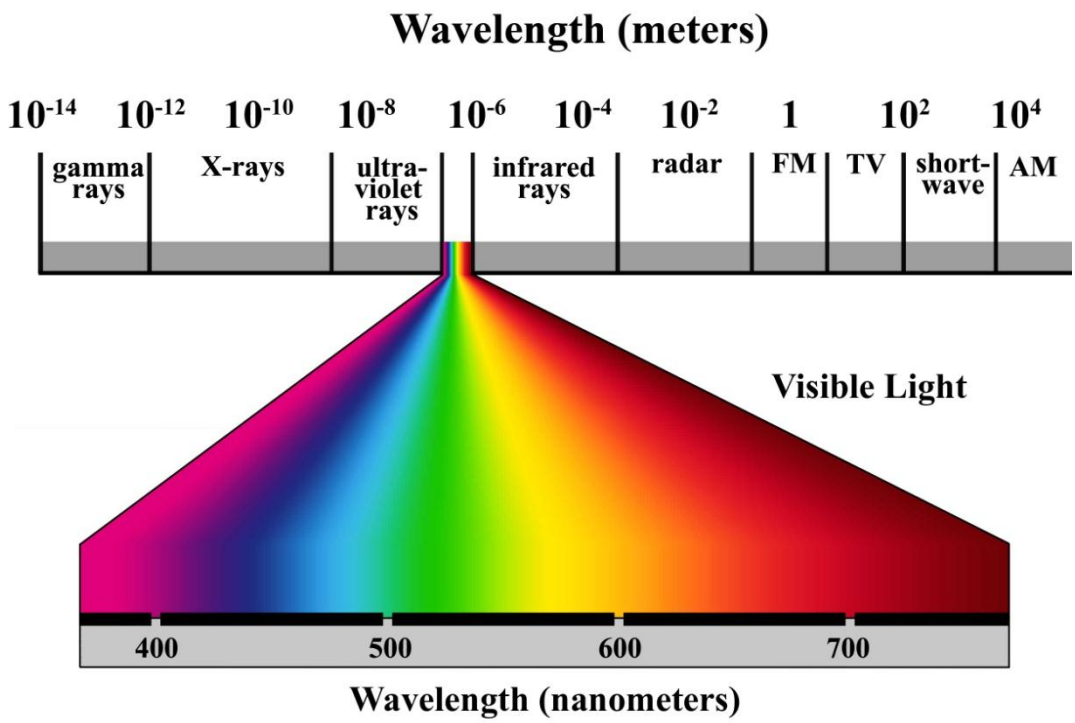

Figure 1: Electromagnetic spectrum and visible light

The behavior of light depends on the structure and physical properties of the area it travels through. The geometric relationship between the light and the object with which it interacts indicates the description suitable of assessing the behavior of light. Thus, atomic and microscopic interactions are described by the particle nature (photons) and at a macroscopic scale wave properties are used [1].

2.1.1 Light scattering

The scattering of light is the redirection of electromagnetic radiation in matter. There are two different types of scattering. The first scattering type is the elastic or Rayleigh scattering. Here no energy transfer occurs between photons and matter, i.e. the wavelength of the photon is not changing. The second scattering type is called inelastic or Raman scattering. In this case an energy transfer occurs resulting in photons with longer wavelength and lower energy. For biomedical applications investigating tissue properties, Rayleigh scattering is the primary scattering type, while Raman scattering is only observable for high incident light

intensities[1]. To depict the effect of light scattering, a scattering-only object was built and illuminated by a laser source. Figure 2 showcases the loss of the directionality of the laser beam after several millimeters. Due to the light scattering properties of the phantom, the red light appears like a diffusive cloud.

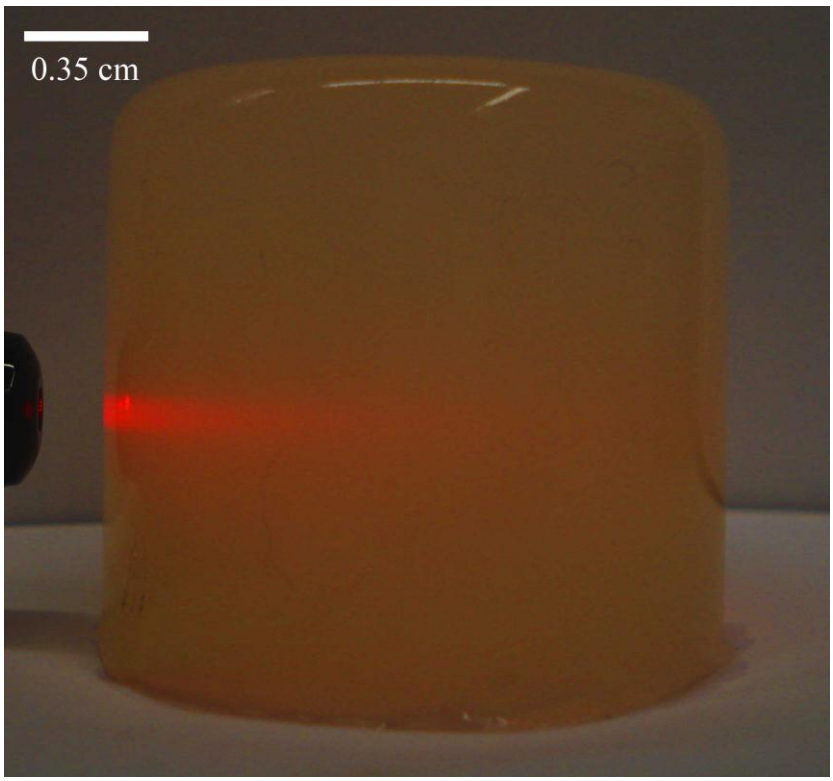

Figure 2: Demonstration of light scattering with a scattering phantom

2.1.2 Light absorption

Light absorption in optical imaging is the second main hindrance for deep tissue imaging. In contrast to scattering, which manifests in the loss of the directionality of the photons resulting in blur and reduced resolution, light absorption blocks the photon propagation (Figure 3).

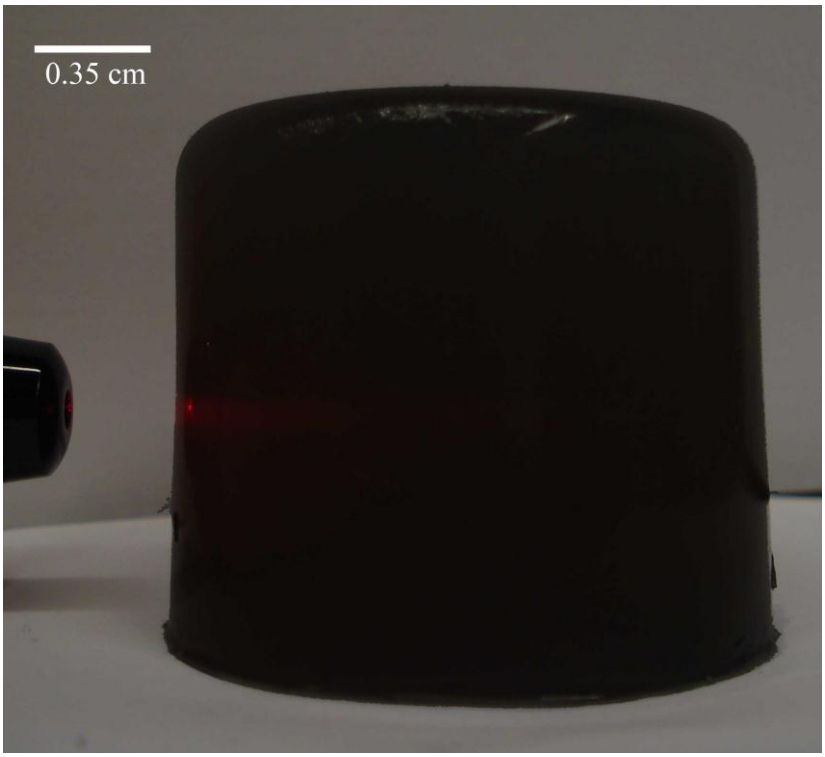

Figure 3: Absorption of a laser beam after several millimeters in a highly absorbing media.

In contrast to conventional optical imaging technologies, optoacoustic tomography relies on the effect of light absorption. The absorption of light (photons) and its thermal conversion is the fundamental principle of the optoacoustic effect. The light absorption occurs by inducing electrons from a single ground electronic level S_0 to an excited state S_n (n>1) (Figure 4). The excited molecule is energetically unstable in its new state and therefore it will return to its ground state S_0. This is done by two steps. First the excited molecule in the state S_n dissipates its energy partially in the surrounding environment by reaching the lowest excited

state S_1 [42]. The second part is the most interesting for molecular imaging. The S_1 electron reaches the ground state S_0 through one of the following competitive processes (Figure 4):

a) Fluorescence by emitting a photon.

b) Energy absorption, which is conducted by the molecules as heat.

c) Energy transfer to molecules nearby.

d) Transition to an excited energetically unstable triplet state T_1 of lower energy than S_1.

To reach the ground state form a T state several processes can occur (Figure 4):

- Phosphorescence
- Dissipation as non radiative energy.
- Energy transfer to another molecule by distance or collision.

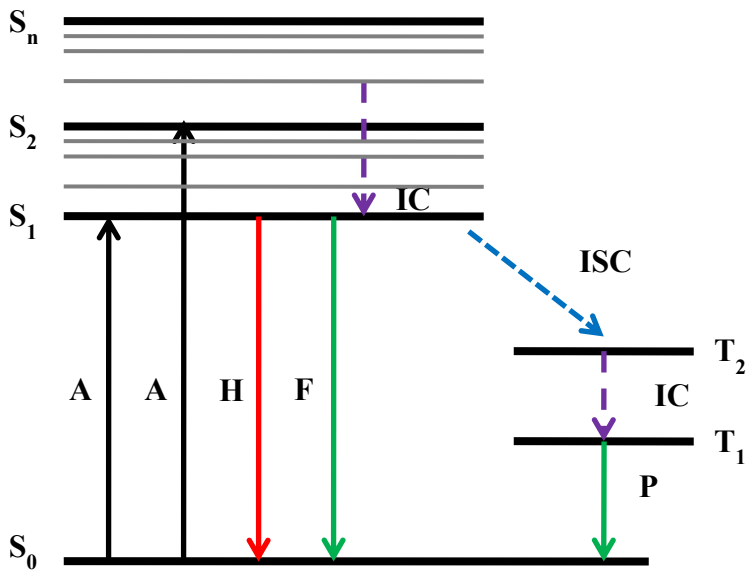

Figure 4: Jablonski Diagram IC: Internal conversion, ISC: Intersystem crossing, H: Heat dissipation, A: Absorption, F: Fluorescence, P: Phosphorescence, S: Singlet states, T: Triplet states

The transitions between excited singlet states S => S or triplet states T => T are called internal conversions. Intersystem crossing is the transition between the excited singlet state

and their corresponding triplet state S_n => T_n [42]. There is a differentiation between absorbing-only and photon-emitting molecules. A photo-emitting molecule is always also an absorbing molecule and called a fluorophore. The term ‚chromophores' describes molecules, which are solely photons absorbing photons.

The light absorption in tissue represents a fundamental limitation for optical imaging technologies in the biomedical field. The most dominant absorber in tissue is hemoglobin, which attenuates light by approximately two orders of magnitude after one centimeter. In detail the spectral characteristics of hemoglobin vary in the visible light spectrum and depend additionally on the oxygenation state of the hemoglobin. Figure 5a shows the absorption spectrum for oxygenated (HbO_2) and deoxygenated (Hb) blood using data from W. B. Gratzer, Med. Res. Council Labs, Holly Hill, London and N. Kollias, Wellman Laboratories, Harvard Medical School, Boston. In many practical cases a separation between oxygenated and deoxygenated hemoglobin is not needed and the spectrum of the whole blood volume has to be considered (Figure 5b). For optical imaging the NIR region (800 – 1000 nm) of the blood spectrum is of special interest, because the light absorption is relatively weak and the spectrum has no fast spectral variations. Light of that spectrum can reach deep tissue regions. Additionally, the detection of molecular markers is easier by using spectral difference methods due to the flat spectrum.

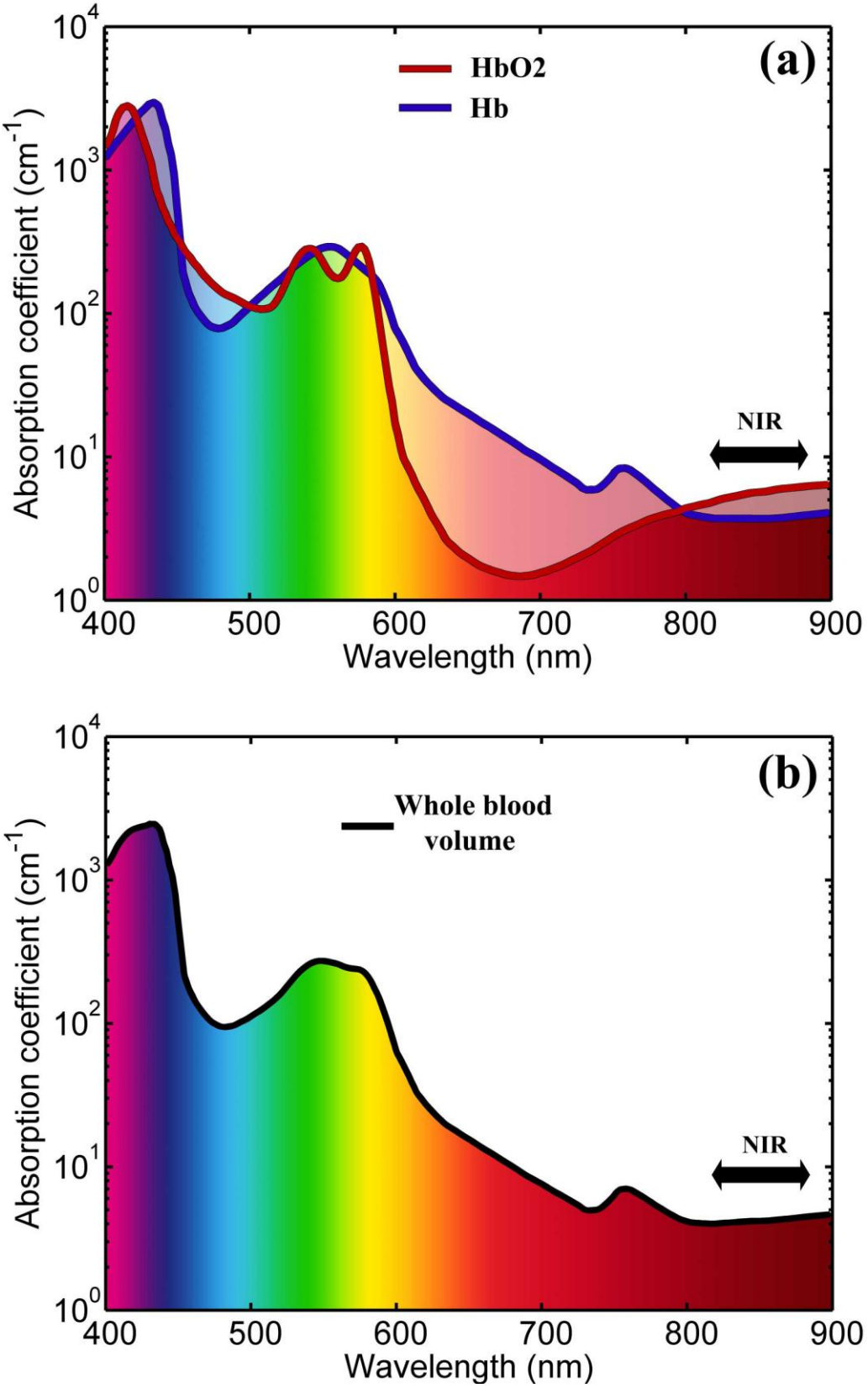

Figure 5: (a) absorption spectrum of oxygenated (HbO_2) and deoxygenated blood (Hb) (b) absorption spectrum of the whole blood volume (Reprinted with permission from [43]. Copyright 2011, Royal Society of Chemistry).

2.1.3 Optoacoustic effect

Optoacoustic imaging is based on the absorption and heat conversion of electromagnetic energy (particularly of light) in matter with subsequent of acoustic detection. The generation of the acoustic waves is achieved by illuminating the object or region of interest with short high-power laser pulses, thus creating an instantaneous temperature elevation and thermal expansion within the matter due to light absorption (Figure 6).

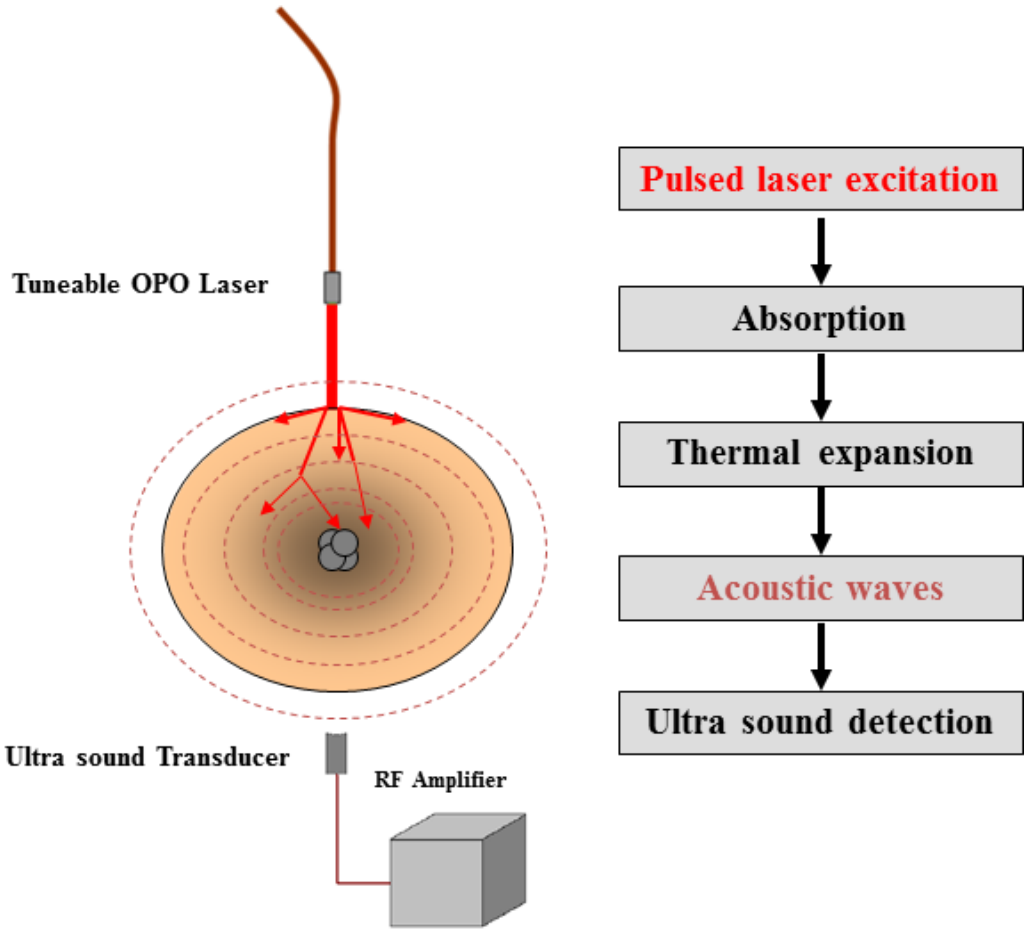

Figure 6: Optoacoustic signal generation

To neglect heat conduction, thermal confinement is ensured by choosing laser pulses in nanosecond range. To record the acoustic waves, ultrasound transducers must be used with a bandwidth suitable for covering the appropriate acoustic spectrum. While the typical frequency range for OAT lies between 0.05 MHz – 10 MHz, for optoacoustic microscopy frequencies up to 100 MHz are relevant. The recorded signal is a time derivative of the

original pressure generated by the thermally induced vibration of the absorbing matter. Figure 5a depicts the recorded ideal signal generated by a delta function. The signal has an N shape, which is a typical characteristic for point sources in optoacoustics. Displaying a signal in its integrated form is also a common representation of measured optoacoustic waves (Figure 7a/b).

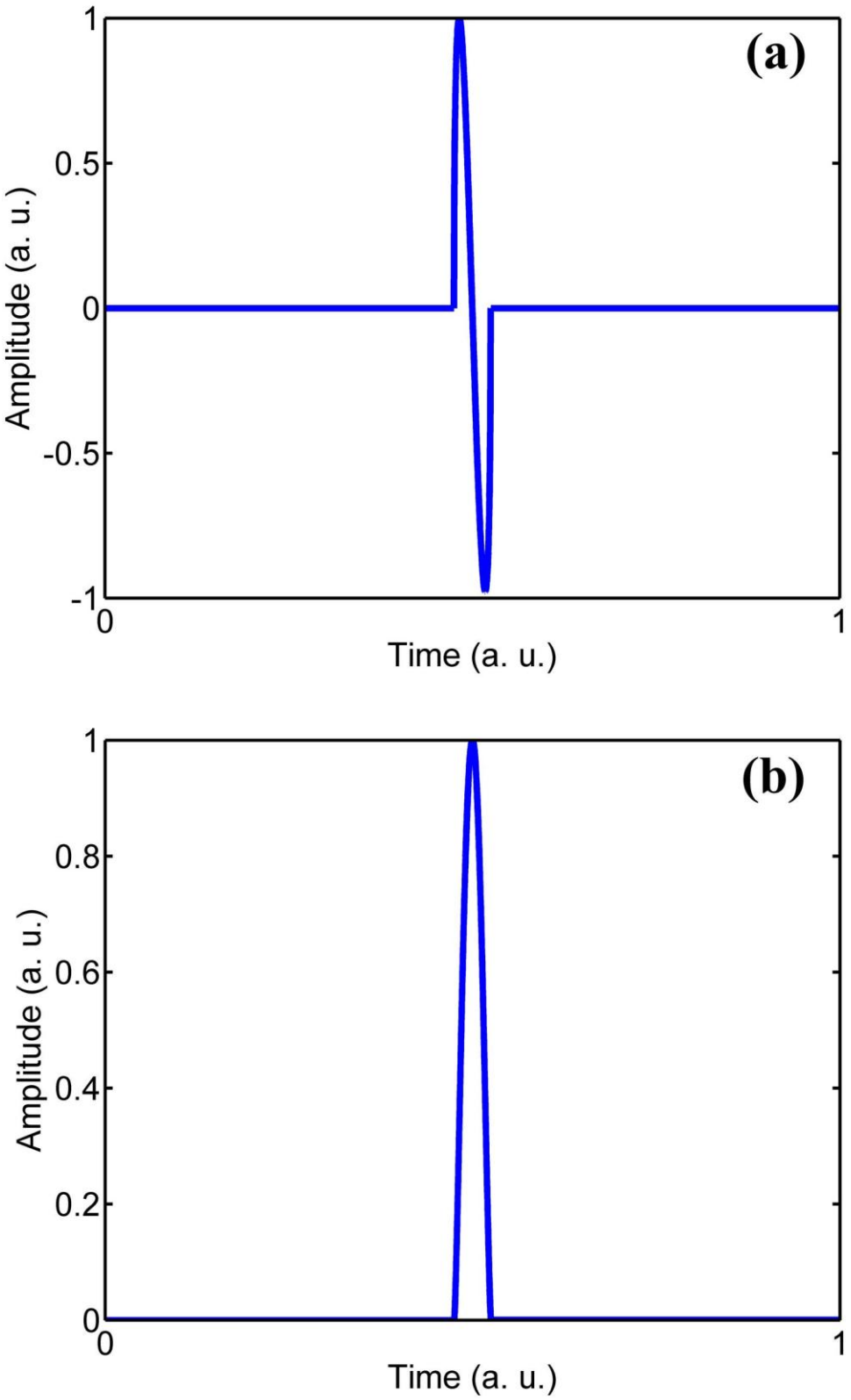

Figure 7: (a) ideal signal generated for a point source measured by a transducer (b) integrated signal of figure 5a

2.2 Historical review of optoacoustics

In 1880 Alexander Graham Bell discovered the optoacoustic effect. He showed that thin discs emit sound when exposed to a beam of sunlight that was rapidly interrupted by a rotating slotted disk. Here, the absorbed energy from light is transformed into kinetic energy by the thermal expansion. The result of the heat dissipation, which was described in the previous section, is the generation of pressure wave, which was perceived by Mr. Bell.

The basic setup, which was used by Bell is shown in Figure 8 [41]. The interruption of the sunlight was performed by two similarly perforated discs, one of which was set in rapid rotation, while the other remained stationary.

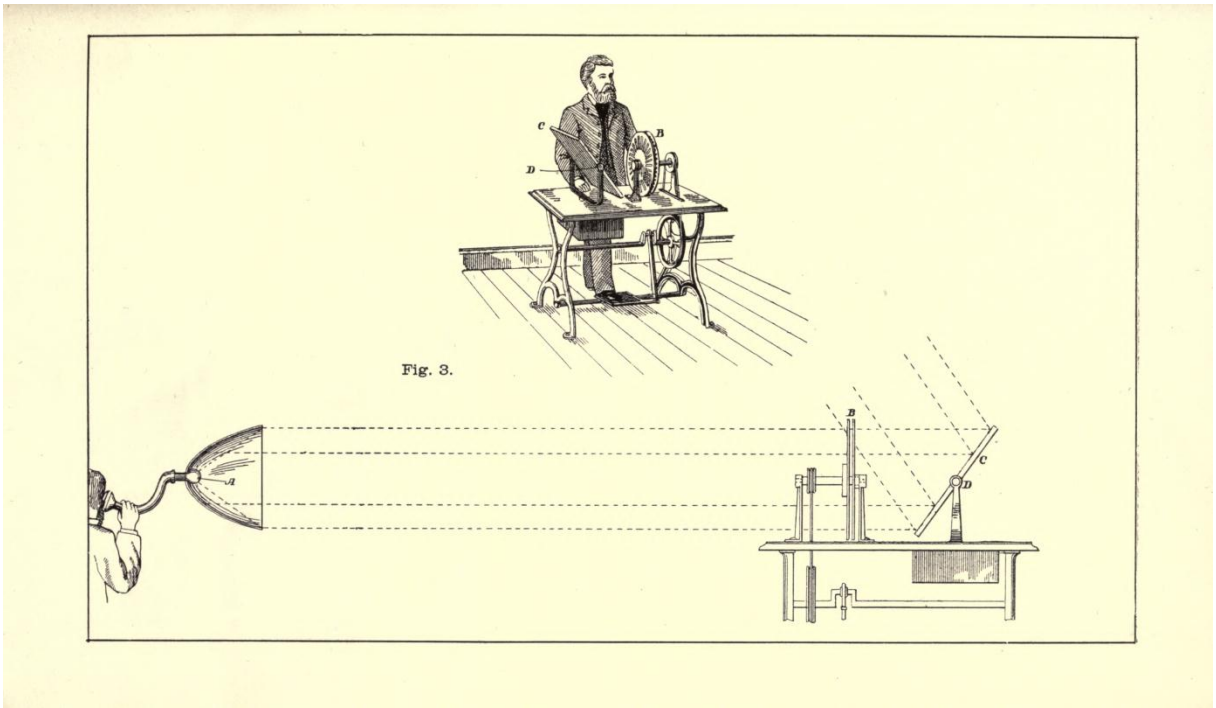

Figure 8: Basic setup Alexander Graham Bell used in 1881 (Reprinted with permission from [41]. Copyright 1881, Science).

The optoacoustic effect enjoyed great attention after its discovery, but the practical application for example in spectroscopy was not done for over a half of a century. This was due to the lack of intense light sources and precise methods of measurement during Bell´s time.

In 1938 M.L. Viengerov was the first who revived the optoacoustic effect for gas analysis, which remained the most widespread application for the following decades [20]. The development of lasers in the 1970s provided high intensity light, which eliminated one of the main issues for a wide spread application. L. B. Kreuzer reported in 1971 about the application of optoacoustics in detecting gas constituents by using a laser-induced optoacoustic effect [44]. The optoacoustic effect found broad practical applications in physics, chemistry, biology, engineering and medicine [20, 45].

Although the application of the optoacoustic effect in biology and medicine began in the 1970s [46], the progress was slow until the end of the 1990s where a lot of pioneering work was done to use optoacoustics for optically scattering media like biological tissue [17, 24, 47, 48]. In the last decade optoacoustic applications in biomedicine became a vastly growing field in research and industry. The quality of the acquired images has increased substantially by the availability of better lasers and acquisition hardware. Due to the advanced performance of computers the inversion schemes evolved from primitive filtered back-projection algorithms [29] to model-based inversion schemes [31]. The usage of molecular probes with a distinct absorption spectrum has extended optoacoustics to multi-spectral applications, known as multi-spectral optoacoustic tomography [2, 40]

The first modern optoacoustic systems were used in the field of spectroscopy. These systems have not deviated far from Bells original setup, apart from the introduction of laser light sources and precise acoustic transducers. A typical optoacoustic system consists of a laser light source, which is precisely pulsed, an incident chamber where the object is illuminated and a transducer to measure the acoustic waves. For spectroscopy, the optoacoustic sound spectrum of a sample is acquired by measuring the acoustic pressure waves at different excitation wavelengths. The spectrum is subsequently used to identify the components of the sample [21]. In spectral analysis of gas concentrations optoacoustic or

photoacoustic spectroscopy has become powerful tool [49]. Figure 9 illustrates an example of an assembly of an optoacoustic spectroscope.

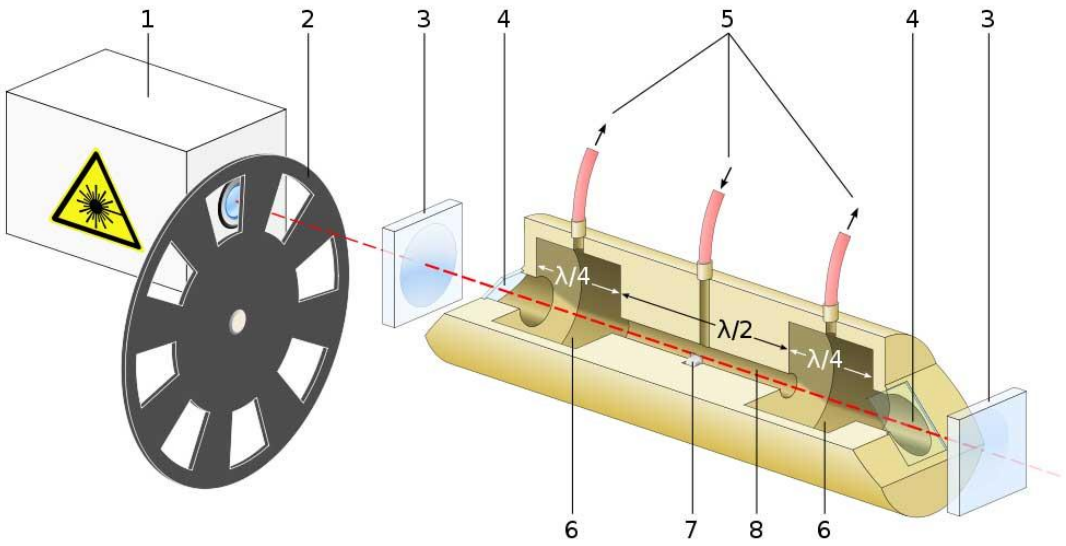

Figure 9: Example of an assembly of an optoacoustic spectroscope for gas analysis with an acoustic cell. Resonance occurs at a wavelength of double the resonator length. Instead of a chopper wheel, variation of the absorption could also be achieved with a tunable laser, modulating its frequency across absorption wavelength. Additional λ/4 tube elements could be added for example in the gas inlet to prevent unwanted flow noises. Electronic control elements, especially a lock-in amplifier, are not shown: 1: Light source, 2: Chopper wheel, 3: semipermeable mirrors form an optical resonance system, 4: cell windows (tilted for polarization), 5: gas flow inlet and outlets, 6: buffer gas volumes, 7: acoustic sensor (e. g. microphone or transducer), 8: resonator (source: Wikipedia, photoacoustic spectroscopy: http://en.wikipedia.org/wiki/Photoacoustic_spectroscopy)

In the field of biomedical research the optoacoustic effect can be used for tomographic, microscopic, catheter systems and handheld devices. With optoacoustic imaging technologies it is possible to image in the macroscopic, mesoscopic and microscopic ranges providing high contrast in up to subcellular resolution[2]. Additionally it is possible to target molecular probes by using multi spectral optoacoustic tomography (MSOT). The following subchapter gives a brief overview of the basic components of an optoacoustic system and of applications in the field of biomedical research with optoacoustics. The author makes no claim of completeness, as the field of optoacoustics is evolving rapidly.

2.2.1 Basic components of modern optoacoustic systems

The two main components of an optoacoustic system are the light source and the acoustic transducers. For optoacoustic tomography it is necessary to provide a stable light source, i. e. a laser. The laser is pulsed in the nanosecond range to assure thermal and stress confinement. Laser light at different wavelengths for multi spectral optoacoustic tomography is provided by pump lasers coupled to an optical parametric oscillator (OPO) [50] or a dye laser [51]. The energy used for biomedical applications lies in the range between 5 mJ and 20 mJ depending on the wavelengths used and on the application.

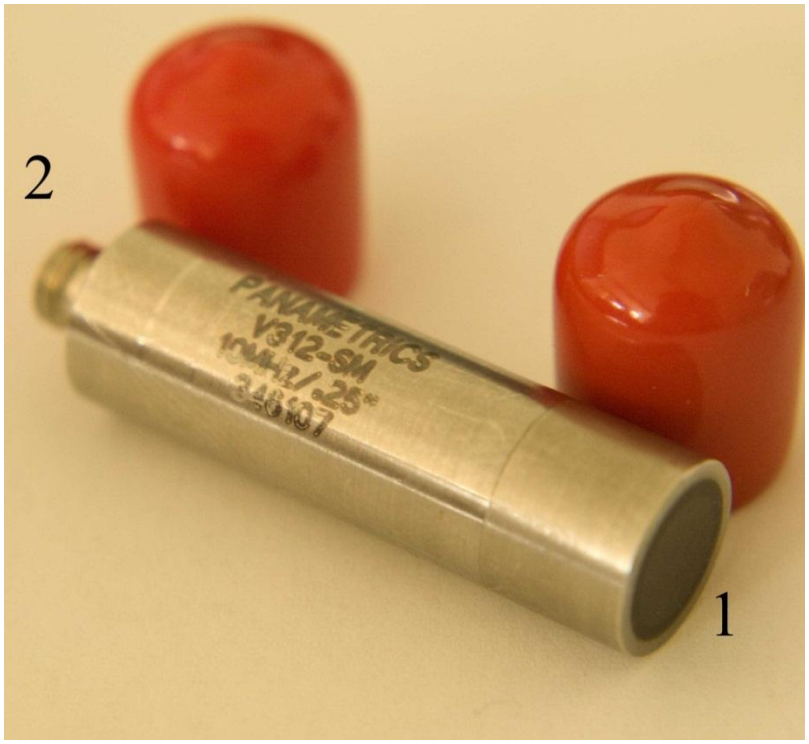

Figure 10: Acoustic transducer Panametrics: V312-SM (1) Detection surface (2) connector

The second main component for optoacoustic systems is the acoustic transducer. Transducer characteristics must be considered for specific applications. A transducer consists of a detection surface - the aperture - and a connector to transmit the measured signals to the recording hardware (Figure 10). The field of view or ~~–~~what the transducer hears" is described by the sensitivity field of the sensor. The sensitivity field is also a measure of the detectable frequency spectrum at each position, whereas the focal distance corresponds to the position of

maximum sensitivity of the transducer. A transducer can be focused in one or two dimensions by using a spherical or cylindrical aperture. For optoacoustic measurements, transducers must be selected according to the expected frequency spectrum, which is recorded. The frequency spectrum is closely related to the target size and will be discussed in the subsequently following chapter.

Even by selecting a transducer with a proper frequency spectrum, the spectrum itself is non-flat and spatially invariant [18]. The measured signals are corrupted by the electrical and spatial impulse response of the transducer and by the system components. The electrical impulse response can be acquired by measuring a point source in the focus of the transducer, while the spatial impulse response is measured by „point-source-wise" scanning through the detection plane [52, 53]. Though, this work does not focus on that topic proper algorithms are used to correct at least for the electrical impulse response. The influence of the spatial impulse response is assumed to be minimal as long as the measured object stays in the focal area of the transducer [53].

2.2.2 Tomographic systems

The tomographic application of optoacoustics was first experimentally implemented by Gusev *et al.* in 1987 [45]. Here the absorption coefficients in a layered medium were recovered. The used object consisted of a set of glass plates separated by layers of aqueous solutions of $CuCl_2$ in different concentrations, which caused a spatially inhomogeneous absorption of Nd:YAG laser radiation. The optoacoustic signals were recorded and reconstructed according to an analytical solution presented by Burmistrova *et al.* 1978 [45]. Clinical application and the development of more sophisticated reconstruction algorithms were prevented by the lack of precise measurement systems, lasers and computational power. In 2005 Xu *et al.* presented a fast and robust reconstruction algorithm for optoacoustic tomography [29]. Also the availability of better hardware made it possible to bring OAT into the field of biological and medical imaging. Lasers provided stable pulses in the nanosecond range and stable power output, which are necessary to fulfill the stress and thermal confinement constraint [54]. The computational capabilities had increased since the 1990s and high precision ultra sound transducers were available.

The typical OAT system consists of a laser source, a measurement chamber and a transducer for recording the acoustic waves. To acquire acoustic signals from different angles around the measured object several approaches were proposed. For example the object itself may be rotated on a stage, where the transducer and the illumination have a fixed position[55] (Figure 12). It can also be done in the other way around, where the transducer is rotated around the object, the illumination moving or being fixed[56]. For the simultaneous recording of acoustic signals for several projections, transducer arrays can be used instead of a single element system [36]. These systems can be used for real-time optoacoustic tomography, because of their fast acquisition time.

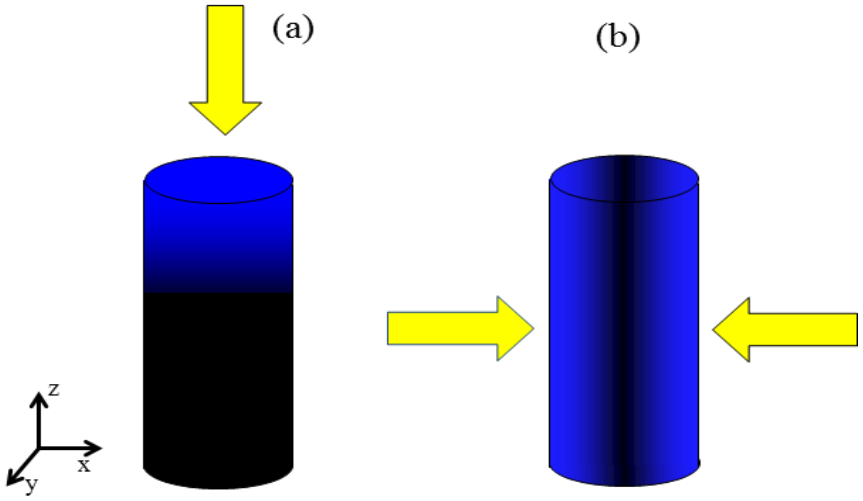

Figure 11: (a) top illumination (b) multi side illumination

For this thesis (Figure 11) optoacoustic systems are classified in top illumination (Figure 13) and multi side illumination systems (Figure 12). In top illumination systems (Figure 13) basically homogeneous illumination is present in each imaging plane, if moved forward on the z-axis. On the contrary in multi-side illumination, each imaging plane on the z-axis suffers from non-homogeneous light distribution.

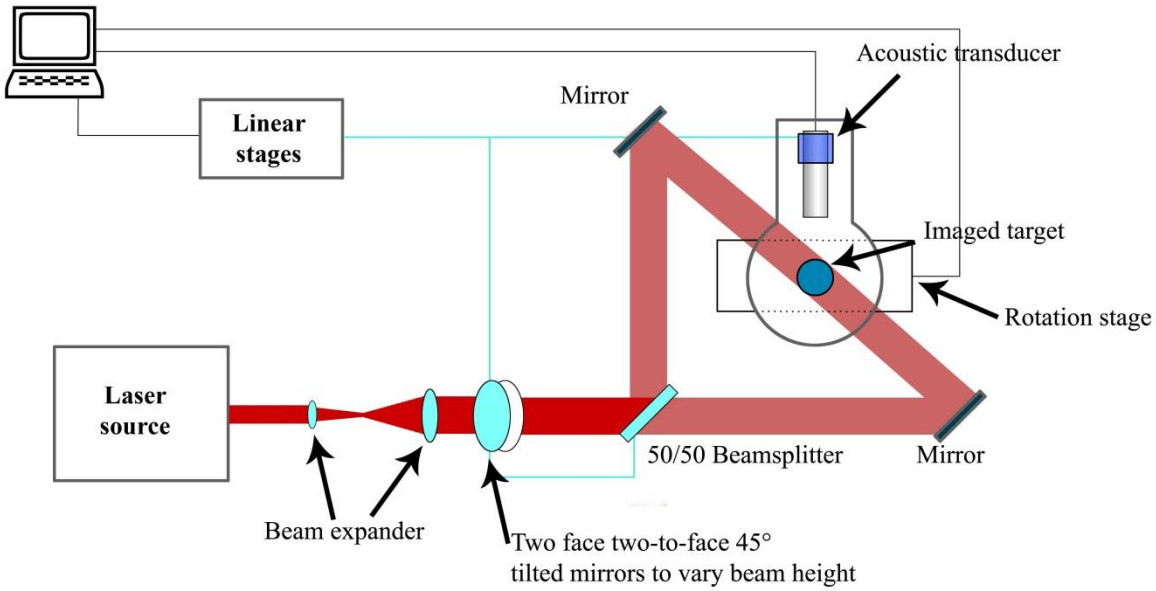

Figure 12: Typical multi side illumination optoacoustic tomographic system (top view)

Both approaches have their advantages and disadvantages. Top illumination systems are easier to implement, because transducers cannot block the path of the light. Furthermore, the

quantification of optoacoustic images can be done more easily because the illumination in each slice is approximately homogeneous. Nevertheless, this method is also very limited, because it can only image an object partially and full body imaging of small animals is impossible. This purpose can be achieved by the multi-side illumination, wherein non-homogeneous illumination in each imaging plane occurs.

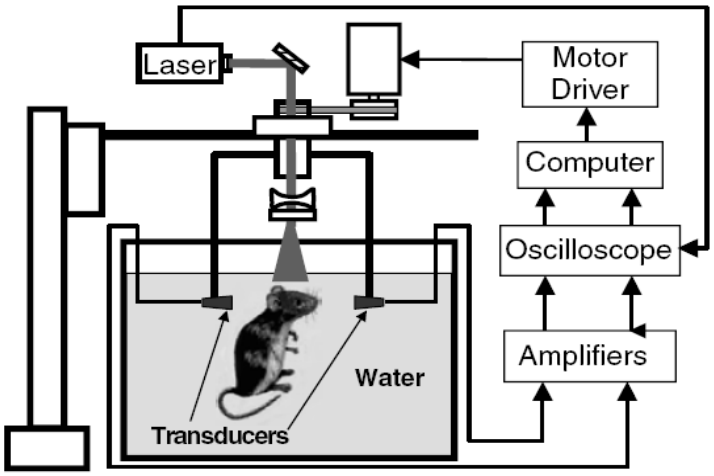

Figure 13: Typical top illumination system used by Wang *et al.* (side view) (Reprinted with permission from [56]. Copyright 2004, ACS Publications)

This work aims to correct for the influence of light attenuation in multi-side illumination systems, as this approach has become the most wide spread illumination method. Nevertheless, light attenuation may also occur in top illumination systems, for imaged targets with heterogeneous optical properties.

2.2.3 Multi spectral optoacoustic tomography (MSOT)

Optoacoustic tomography has been used to image the intrinsic contrast generated by light absorption for structural [57], functional [58] and molecular aspects [59] of tissue. In biomedical imaging, blood and its strong optically absorbing characteristics have been a prime target for imaging vasculature [57], blood oxygenation [60] or tumor angiogenesis [61]. Of particular interest is the development of multi-spectral optical tomography (MSOT) [19, 39, 62], which provides the capability to accurately resolve and quantify the volumetric bio-distribution of molecular probes and tissue biomarkers. The method utilizes illumination at several wavelengths to quantitatively resolve the spectra of various tissue molecules (Figure 14). An additional advantage of MSOT is that the separation of a molecular probe from background can be achieved in the absence of background measurements, i.e. there is no need to obtain data before probe administration [19]. This is useful for most molecular probes, which require some considerable time to deliver and localize at an intended target, typically an hour or more. The information yielded at multiple wavelengths is also employed to improve the accuracy of the reconstructed images as a function of depth and non-homogeneous light distribution [19].

To discuss MSOT in more detail, a simplified scenario is showcased where only two wavelengths are used to detect a molecular probe. A chromophore is assumed to have an absorption peak at wavelength λ_1 and no absorption at λ_2 [39]. By knowing the spectral characteristics of the probe, the optimal wavelengths are selected and optoacoustic signals are acquired. After measuring the signals and reconstructing the images, the images are subtracted from each other [39]

$$\Delta H(r) = H(\lambda_1, r) - H(\lambda_2, r) \tag{2.1}$$

Wherein ΔH is the difference image and $H(\lambda_1, r)$ and $H(\lambda_2, r)$ are the reconstructed images for the wavelengths λ_1 and λ_2, respectively. In practical cases more wavelengths are

selected to apply spectral decomposition methods. The most interesting spectrum for MSOT is the near infrared. Here the optical contrast of the tissue is low and does not have fast spectral changes in the absorption spectrum. The performance of MSOT to detect chromophores has been successively demonstrated in animal tissues and in nonabsorbing phantoms using a dual-wavelength approach. MSOT is also able to provide fast video rate imaging performance for dual wavelength imaging. With advances in wavelength switching technologies more wavelengths can be used to implement multi-spectral video rate imaging [39].

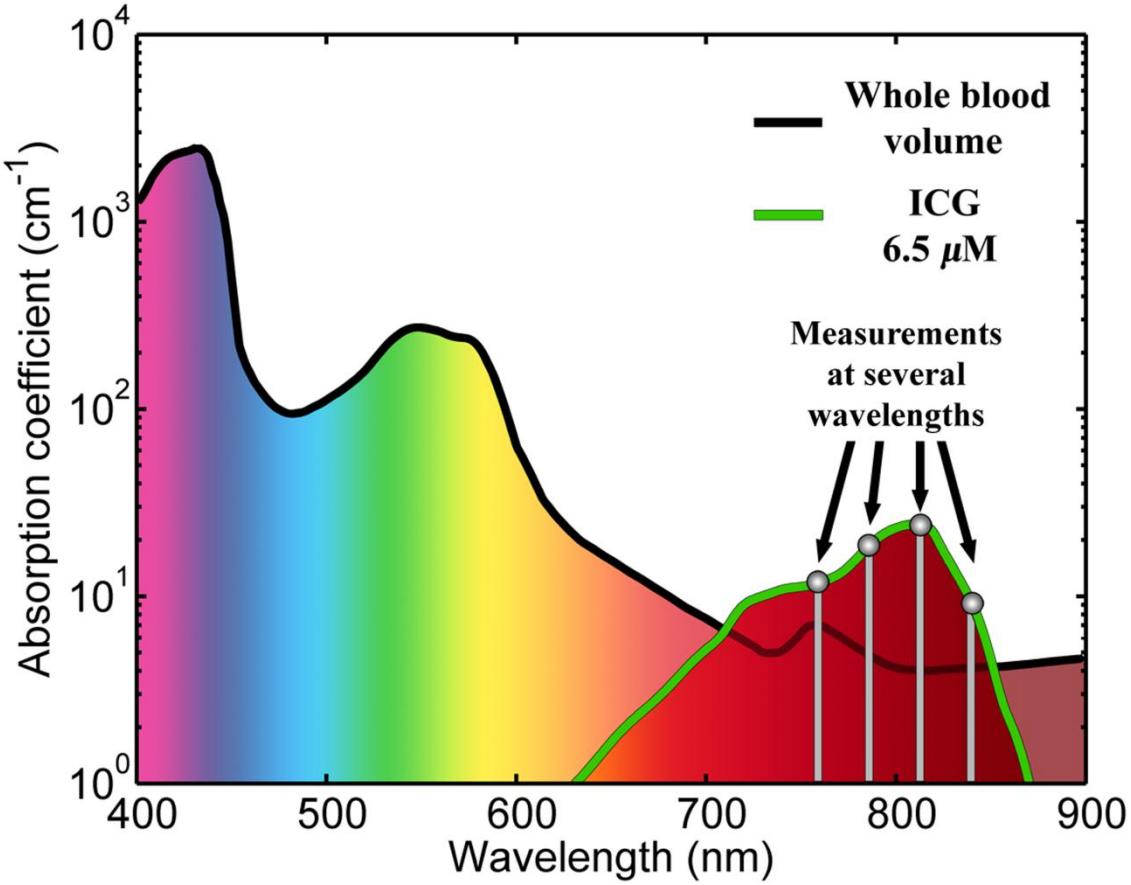

Figure 14: Resolving a molecular probe in the blood volume by multi spectral optoacoustic tomography. (Reprinted with permission from [43]. Copyright 2011, Royal Society of Chemistry).

2.2.4 Other optoacoustic systems

2.2.4.1 Microscopy

Currently existing microscopic systems are not able to provide information about the light absorbing characteristics of a sample. The available high resolution modalities like confocal microscopy or two photon microscopy, cannot sense direct information about the absorption. In 1979 Luukkala presented a optoacoustic microscope [63], which was able to provide a resolution of a few microns. The idea was adopted and advanced for biomedical applications, where it can provide direct information about the physiological status of tissue [64]. Furthermore this modality can overcome the classical penetration depth limitations of ~1 mm in biological tissue.

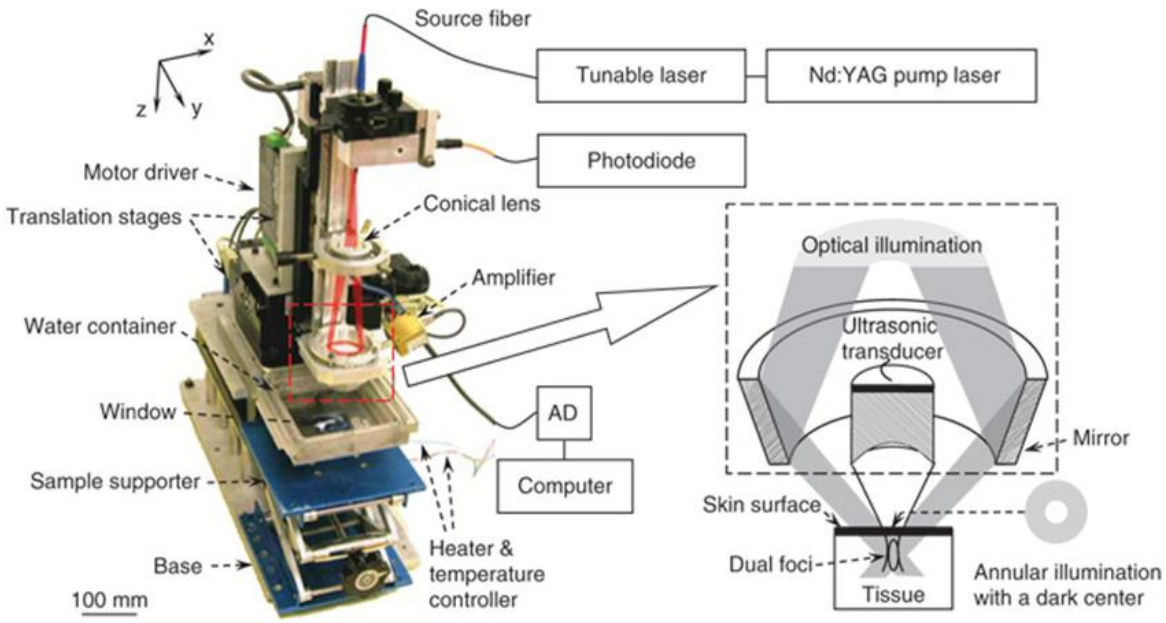

Figure 15: Sketch of an optoacoustic microscope (Reprinted with permission from [64]. Copyright 2006, Nature)

Figure 15 shows a prototype of a functional optoacoustic microscope [64]. Here a tunable dye pump laser is used, where short laser pulses irradiate the target object. For the illumination an optical fiber is coaxially positioned using a three-dimensional mechanical stage. To measure the broad band optoacoustic signals between 25-75 MHz, a changeable

acoustic transducer is additionally mounted onto the stage [64]. The main limitation factor for optoacoustic microscopes is the attenuation of high frequency acoustic waves in tissue, not the light transportation as in other microscopic technologies. A first application has been shown for the detection of oxygenated and deoxygenated blood vessels (Figure 16) and the detection of melanoma cells [64].

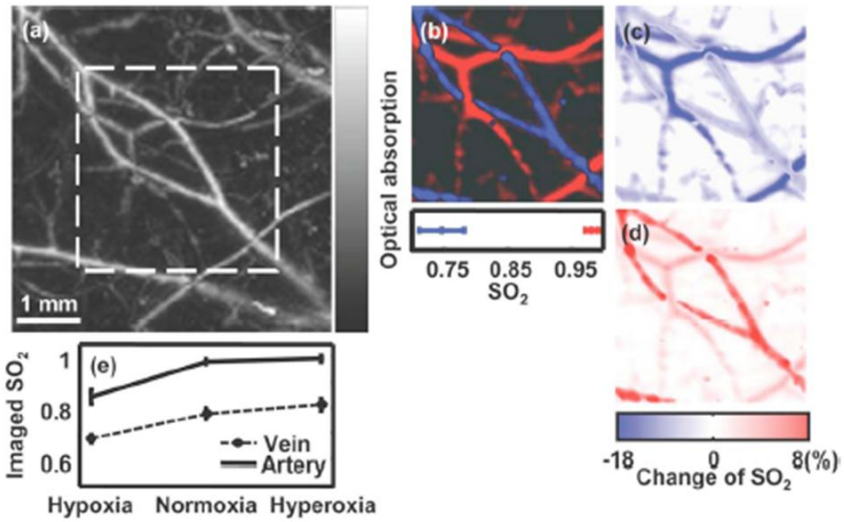

Figure 16: functional imaging of blood vessels (*in-vivo*) in a rat (a) Structural image acquired (b) Vessel-by-vessel sO2 mapping. The calculated sO2 values are shown in the color bar. (c) Microsphere-perfusion image showing arterioles (red) and venules (blue). (d) H&E-stained section showing the vessel structure (Reprinted with permission from [64]. Copyright 2006, Nature).

2.2.4.2 Handheld systems

Endoscopic and handheld systems are implementations of optoacoustic technology, which are in clinical use or will be in use in the near future [65]. Dima *et al.* gave in [66] a detailed review of the currently available systems and therefore only a brief introduction in that topic is given here. Most of these systems are extensions to standard ultra-sound systems [65, 67-69]. The first of these systems was proposed by Niederhauser *et al.* in 2008 [65], where an ultrasound and an optoacoustic system were combined. This group achieved optoacoustic and ultrasound B-scan imaging of human blood vessels up to a depth of 8 mm at a wavelength of

760 nm and a resolution of 0.3 mm axially and 0.4 mm laterally [66]. The transducer of the system was a linear array probe detector with a central frequency of 7.5 MHz and a bandwidth of 76 % (i.e. 4.65 – 10.35 MHz). The array consisted of 128 active elements each with a width of 0.38 mm and a length of 5 mm. Focusing in the imaging plane was achieved by an acoustic lens, which is commonly used in ultrasound probes [66]. The laser source of the system was a Q-switched alexandrite laser tuneable from 700 nm to 860 nm wavelength with a pulse length of 60 nm and pulse energy of 50 mJ. An optical fiber guided the laser light to the handheld probe, where it illuminated an area of approximately 25 mm diameter on the skin directly under the transducer [66].

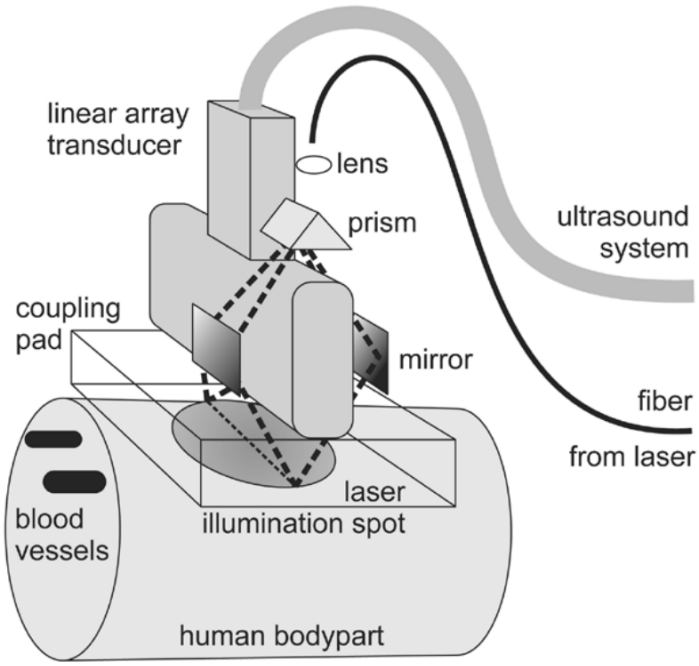

Figure 17: Combined optoacoustic and ultrasound real-time imaging setup (Reprinted with permission from [65]. Copyright 2005, IEEE).

Similar approaches were implemented by Kolkman *et al.* in 2008, Haisch *et al*. in 2010 and Kim at al in 2010. All these systems combine ultrasound with optoacoustic hardware. The main difference in these systems can be found in the ultrasound transducers and laser excitation [66] employed.

2.3 Quantification challenges

Optoacoustic tomography is a high resolution imaging modality providing good optical contrast [2]. It can quantitatively resolve molecular markers and it is able to image the intrinsic optical contrast of anatomical structures [19]. As light travels through an absorbing media it gets partially absorbed and subsequently generates an acoustic wave. In brief, this is the basic principle of optoacoustic imaging. The drawback consists in the loss of energy occurring as the photons travel a distance, resulting in an attenuated acoustic signal for absorbers distant form the light source, whereas absorbers close to the source generate a strong signal with high amplitude. Absorbers with the same optical properties appear much weaker or visually vanish for an observer, if they are located centrally in an object [70]. Figure 18 shows a simulated phantom with two insertions with the same optical absorption. The absorbing insertion close to the boundary of the numerical phantom can be clearly detected, whereas the central insertion is barely visible. This relationship can be described by

$$H(r) \sim \mu_a(r) U(r) \tag{2.2}$$

where *H(r)* is the optoacoustic image, *U(r)* is the photon fluence and μ_a is the light absorption.

This effect is most dominant in multi-side illumination systems, which are heavily used in optoacoustic tomographs. With less dramatic impact the effect is also present in top illumination approaches, which are often used in microscopic imaging scenarios. Due to the heterogeneous optical properties of tissue, deeper layers of imaging also suffer from the effect of light attenuation.

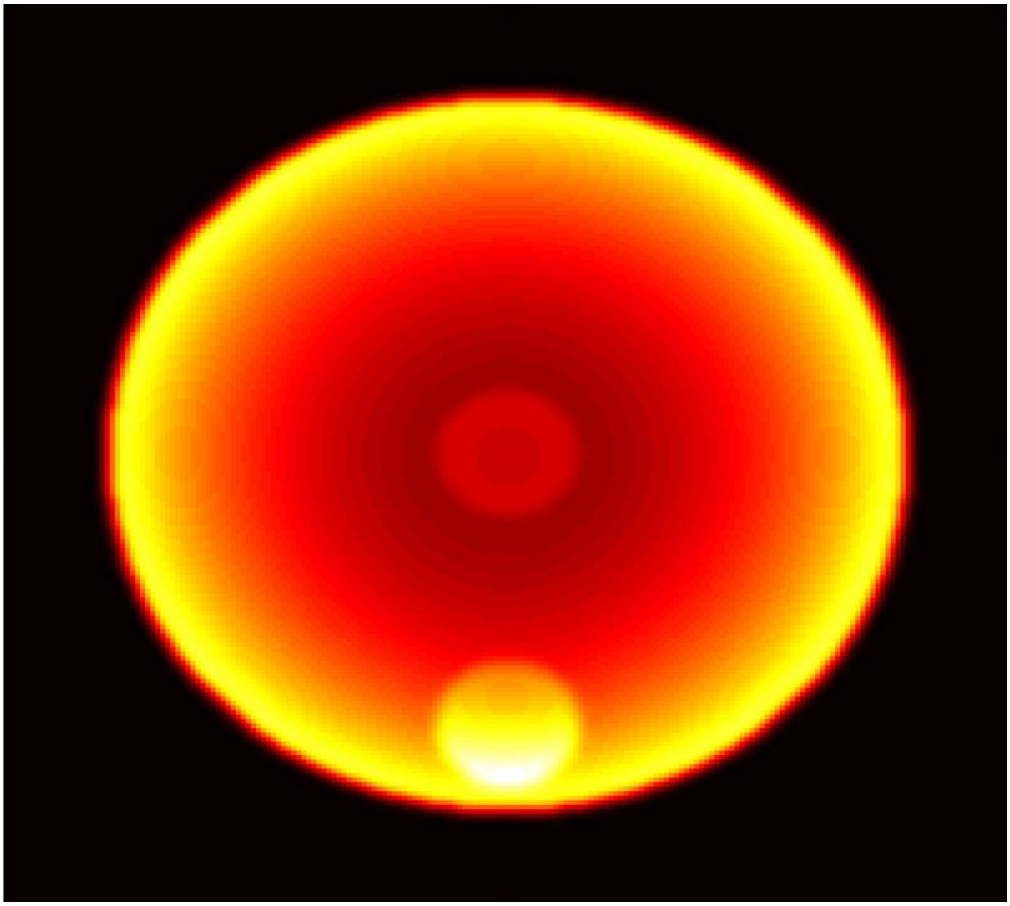

Figure 18: Typical quantification problem in optoacoustic tomography

There were several methods proposed to correct for the influence of the light attenuation [70-73]. Most of them are based on analytical or numerical descriptions of the photon fluence in tissue [74]. Several commonly used methods were studied in this work. In simulations each of these methods provides a good performance. Also an iterative algorithm was adopted for multi-side illumination scenarios which has generally a better performance compared to non-iterative methods [70]. Nevertheless, these methods have a low sensitivity in real experiments, because in reality data is flawed by issues inherent to the hardware. Additionally, assumptions must be made for parameters, which cannot be acquired experimentally. To avoid these problems a ratiometric approach is presented, which provides a very high sensitivity for the detection of molecular probes. It showed a very good performance in simulations as well in phantom and animal experiments.

Besides the effect of the light attenuation, several other effects are hindering the quantification of molecular probes in optoacoustic tomography. The inversion schemes used to reconstruct an optoacoustic image can generate artifacts itself. The commonly used back-projection algorithm is well known for its artifact rich reconstruction results [75], whereas the recently introduced interpolated model matrix inversion (IMMI) reconstructs images accurately [75]. This issue is also addressed in this work and a modified IMMI algorithm presented, which can also correct for inhomogeneous surface illumination[76]. Quantification problems caused by electrical and spatial impulse responses are already discussed by Rosenthal *et al.* [31, 52, 53]. To avoid the influence of the spatial impulse response, targets are selected, which stay spatially within the focal zone. In this area the variations of the spatial impulse response are minimal. The bias introduced by the electrical impulse response is corrected by using appropriate deconvolution algorithms on acquired signals.

3. Image formation

This chapter will give a general introduction in the theory of image formation in optoacoustic tomography. The general forward solution as well as inversion schemes for image reconstruction will be presented. Additionally, a modified version of the recently introduced interpolated model matrix inversion scheme is discussed which was developed by myself to correct for inhomogeneous surface illumination [31, 76].

3.1 General forward solution

Before discussing the inversion algorithms in detail, it is necessary to describe the optoacoustic phenomenon mathematically. It can be generally described following the non-homogeneous wave equation [18] Equation Section (Next)

$$\left(\nabla^2 p(\vec{r},t) - \frac{1}{c^2}\frac{\partial^2}{\partial t^2}\right) p(\vec{r},t) = -\frac{\beta}{\kappa c}\frac{\partial^2 T(\vec{r},t)}{\partial t^2} \tag{3.1}$$

where p represents the pressure at location r at time t, c is the sound velocity, β is the isobaric volume expansion coefficient, κ is the isothermal compressibility and T describes the temperature rise. The left side of the equation describes the wave propagation, whereas the right side shows the source term [77]. In thermal confinement the equation can be simplified. This can be achieved by using pulsed laser sources with a pulse length much lower than the thermal relaxation time. In this case the acoustic pulse is generated before significant heat conduction takes place. As a consequence, the assumption of zero thermal heat conduction is justified for determination of optoacoustic wave forms[18]. The equation can then be written as

$$\nabla^2 p(\vec{r},t) - \frac{1}{c^2}\frac{\partial^2 p(\vec{r},t)}{\partial t^2} = -\frac{\beta}{C_p}\frac{\partial \hat{H}(\vec{r},t)}{\partial t} \tag{3.2}$$

where $\hat{H}$ is the heat function and C_p is the heat capacity. Again, a forward solution can be derived if the condition of thermal confinement is fulfilled. The forward solution can then be written as

$$p(\vec{r},t)=\frac{\beta}{4\pi C_p}\int\frac{d\vec{r}'}{|\vec{r}-\vec{r}'|}\frac{\partial\hat{H}(\vec{r}',t')}{\partial t'}\bigg|_{t'=t-|\vec{r}-\vec{r}'|/c} \tag{3.3}$$

where t' is the time when the heating occurs. If additionally the condition of stress confinement is fulfilled, which means the laser pulse is much shorter than the stress relaxation time, the forward solution of equation (3.2) can be further derived as

$$p(\vec{r},t)=\frac{\beta}{4\pi C_p}\frac{\partial}{\partial t}\left[\frac{1}{ct}\int d\vec{r}'p_0(\vec{r}')\delta(t')\right] \tag{3.4}$$

where p_0 is the initial optoacoustic pressure. The initial pressure generated by a laser pulse $\delta(t')$ equals $p_0(r')=\Gamma(r')\cdot A(r')$, where A is a spatial absorption function and Γ is the Grüneisen parameter $\Gamma(r')=c^2\beta C_p^{-1}$ [77].

For better understanding of equation (3.4), the measured signal for a transducer at point r_0 is discussed in detail. For simplicity we assume two-dimensional geometry and an optoacoustic source at position r'. The source is excited by a laser pulse $\delta(t')$, which subsequently generates the initial acoustic pressure p_0. Figure 19 depicts the process for an optoacoustic source (red dot) on a discrete grid (blue dots) with the origin O at the center (black dot). A quantity of the emitted sound wave of p_0 reaches the sensor after a fixed time by travelling the distance $|r'-r_0|$. The measured signal at time t at sensor position r_0 is a superposition of waves generated by excited sources lying on a circle (dashed circle in Figure 19) with radius $c\cdot t$, which corresponds to the distance $|r'-r_0|$. The measured signal at time t is an integration over the dashed arc centered at r_0, which reduces the spatial two- or three-dimensional information into one dimension. The tomographic measurement is done by

rotating the transducer along the circular scanning geometry S_0 and recording the ultra-sound waves generated by the thermo-elastic response of the light absorption [18, 77].

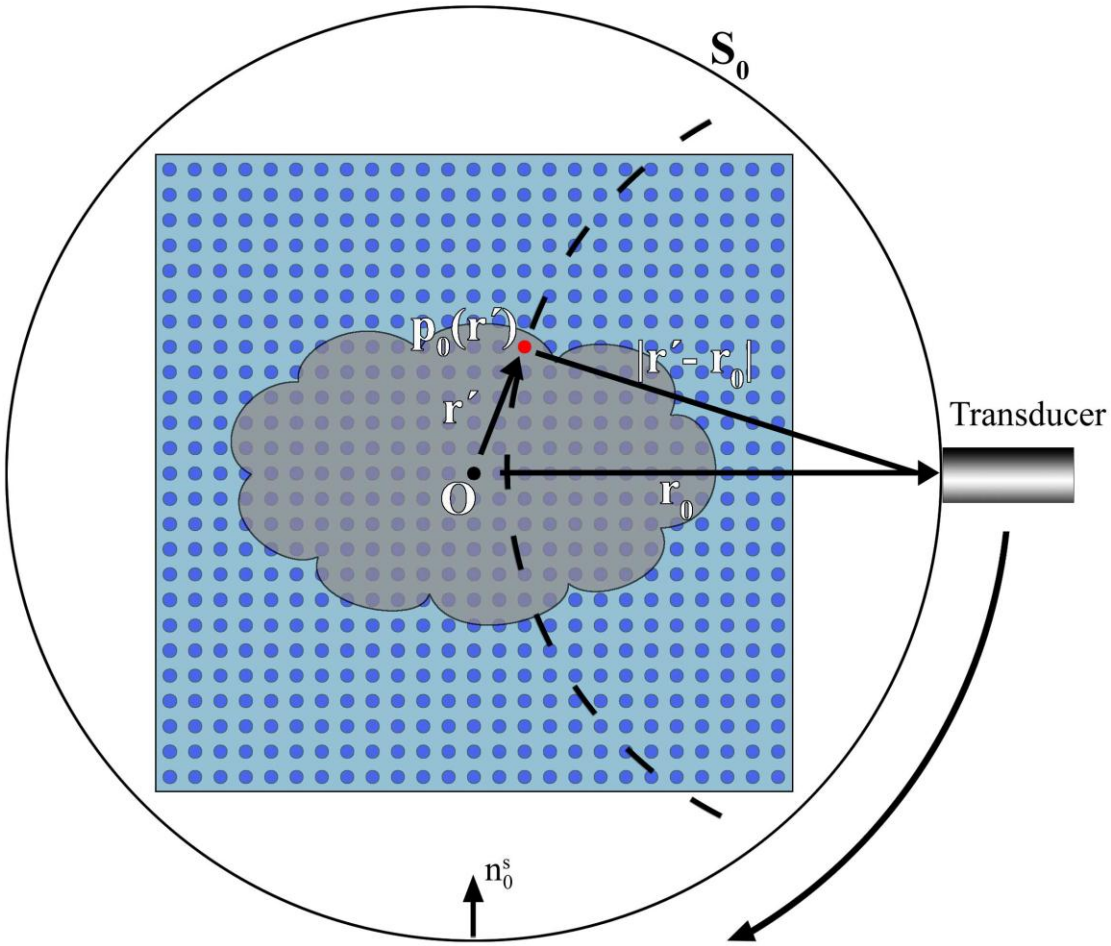

Figure 19: Discretized signal formation in 2D

3.2 Spatial resolution in optoacoustics

This section gives an introduction to the determination of resolution in optoacoustic imaging. A detailed discussion is provided by Wang et al. in Ref. [18]. In brief, the point spread function (PSF) in optoacoustic imaging is spatially invariant and takes the form of a Hankel function [18]

$$PSF^b(R) = \frac{1}{2\pi^2}\int_0^{+\infty} \tilde{H}(k) j_0(kR) k^2 dk \tag{3.5}$$

where $\tilde{H}(k)$ is a Hankel transform for even functions, b is the bandwidth, R is the distance between source and detector. A temporal representation of $\tilde{H}(k)$ can be defined with the help of the Fourier Transform [18]

$$\tilde{H}(t) = \frac{1}{2\pi}\int_{-\infty}^{+\infty} \tilde{H}(k)\exp(-ikt)dk \tag{3.6}$$

If $\tilde{H}(k)$ is even and real, equation (3.5) can be rewritten as [18]

$$PSF^b(R) = -\frac{1}{2\pi R}\frac{d\tilde{H}(R)}{dR} \tag{3.7}$$

If $\tilde{H}(k)$ is odd and imaginary, the real part of equation (3.5) becomes zero, leading to a zero result in the real part of the PSF[18].

The integral of equation (3.5) can be simplified, if $\tilde{H}(k)$ is even and has a cut off frequency of k_c [18]

$$PSF^b(R) = \frac{k_c^3}{2\pi^2}\frac{j_t(k_c R)}{k_c R} = \frac{k_c^3}{6\pi^2}\frac{3 j_t(k_c R)}{k_c R} \tag{3.8}$$

By normalizing this equation, the PSF can be written as [18]

$$PSF^{b}(R) = \frac{3 j_t(k_c R)}{k_c R} \tag{3.9}$$

As a measure for the resolution *(R_H)* the full width half maximum (FWHM) of a point spread function (PSF) is often used [18]. It can be easily shown that *$3j_t(x)/x=0.5$ when $x=2.4983$* [18]. Therefore the resolution is defined by [18]

$$R_H = 2\frac{2.4983}{k_c} = 2\frac{2.4983}{2\pi f_c / c} = \frac{0.7952c}{f_c} \approx 0.8\lambda_c \tag{3.10}$$

where f_c is the cutoff frequency, c is the propagation speed of the pressure wave and λ_c is the wavelength, which corresponds to size of the optoacoustic source. To determine the cut off frequency, a transducer should at least cover a certain target size. Equation (3.10) can be rewritten as [18]

$$f_c = \frac{c}{\lambda_c} \tag{3.11}$$

3.3 Inversion schemes

For optoacoustic tomography several image reconstruction algorithms were proposed in the last decade. The first widely used algorithms to reconstruct optoacoustic images are back-projection based inversion schemes, which were discussed in detail by Xu *et al.* in 2005 [29]. Although back-projection is very popular in the field of OAT, it also has flaws especially in quantifying optoacoustic images. Here, the classical back-projection algorithm is discussed as well as alternative inversion algorithms, which in general provide a better performance in terms of image quality and quantification. Both algorithms are tested with an analytical signal, which showcases the artifacts generated by the back-projection algorithm. Additionally I developed a modified version of the interpolated model matrix inversion scheme, which is capable of correcting for non-homogeneous surface illumination [31, 76]. In chapter 5.2 the performance of these algorithms is evaluated on phantom and animal experiments.

3.3.1 Back-projection

Image reconstruction in optoacoustic tomography has been primarily based on back-projection algorithms [29]. Back-projection relies on closed-form inversion formulae that can be practically applied as two- (2D) and three-dimensional (3D) problems analogously to the Radon transform. Back-projection formulae currently exist for planar, spherical and cylindrical detection geometries and are implemented either in the spatio-temporal domain [29] or Fourier domain [26]. To invert the equation (3.4) and reconstruct the initial pressure source, we need a solution with respect to p_0. A solution was proposed by Xu *et al.* [29] as

$$p_0(\vec{r}') = \int_{\Omega_0} \frac{d\Omega_0}{\Omega_0} \left[2\,p(\vec{r}_0, t) - 2t \frac{\partial p(\vec{r}_0, t)}{\partial (t)} \right]_{t=\frac{|r'-r_0|}{c}} \tag{3.12}$$

where Ω_0 is a solid angle of the whole detection geometry S_0, which is a circle for planar geometries ($\Omega_0=2\pi$). The term $\frac{d\Omega_0}{\Omega_0}$ is a weighting factor for the contribution of the detection element dS_0, which is characterized by the angular position of the sensor and the number of projections. In equation (3.12) $p(\, r_0,\, t\,)$ the pressure is measured at detector position r_0 and time t (assuming the excitation pulse took place at time $t_0 = 0$). The derivative of the detected pressure is taken numerically from the measurement. Ω_0 can be substituted by the surface S_0 with respect to the point in S_0, which is to be reconstructed [29], by

$$d\Omega_0 = \frac{dS_0}{|\vec{r}' - \vec{r}_0|^2} \frac{n_0^s(\vec{r}' - \vec{r}_0)}{|\vec{r}' - \vec{r}_0|} \tag{3.13}$$

where n is the surface normal vector of S_0 pointing to O.

Equation (3.12) can be interpreted as the quantity in brackets simply being projected backwards on a spherical surface (arc, for the two-dimensional case). For practical application the initial pressure at a point $r´$ can be expressed as a summation over a function, which is purely dependent on the geometry of the grid in relation to the sensor, and the recorded signal [77]. It can be implemented by sequentially going through each grid point characterized by $r´$ and each sensor position r_0 and compute t in equation (3.12). Then the derivative is taken from the detected pressure at time point t. The bracket term of (3.12) is subsequently computed and each weighting factor multiplied by the respective bracket term for all sensor positions r_0 is summed up [77].

To evaluate the performance of the back-projection algorithm an analytical signal based on a paraboloid was used. Such an analytical signal allows studying reconstruction errors introduced by the inversion scheme. The used paraboloid is given by the following equation [31, 77]

$$f(x,y)=\begin{cases}0 & \text{for } x^2+y^2>r^2\\ 1-\dfrac{x^2+y^2}{r_p^2} & \text{otherwise}\end{cases} \tag{3.14}$$

where r_p is the radius of the paraboloid.

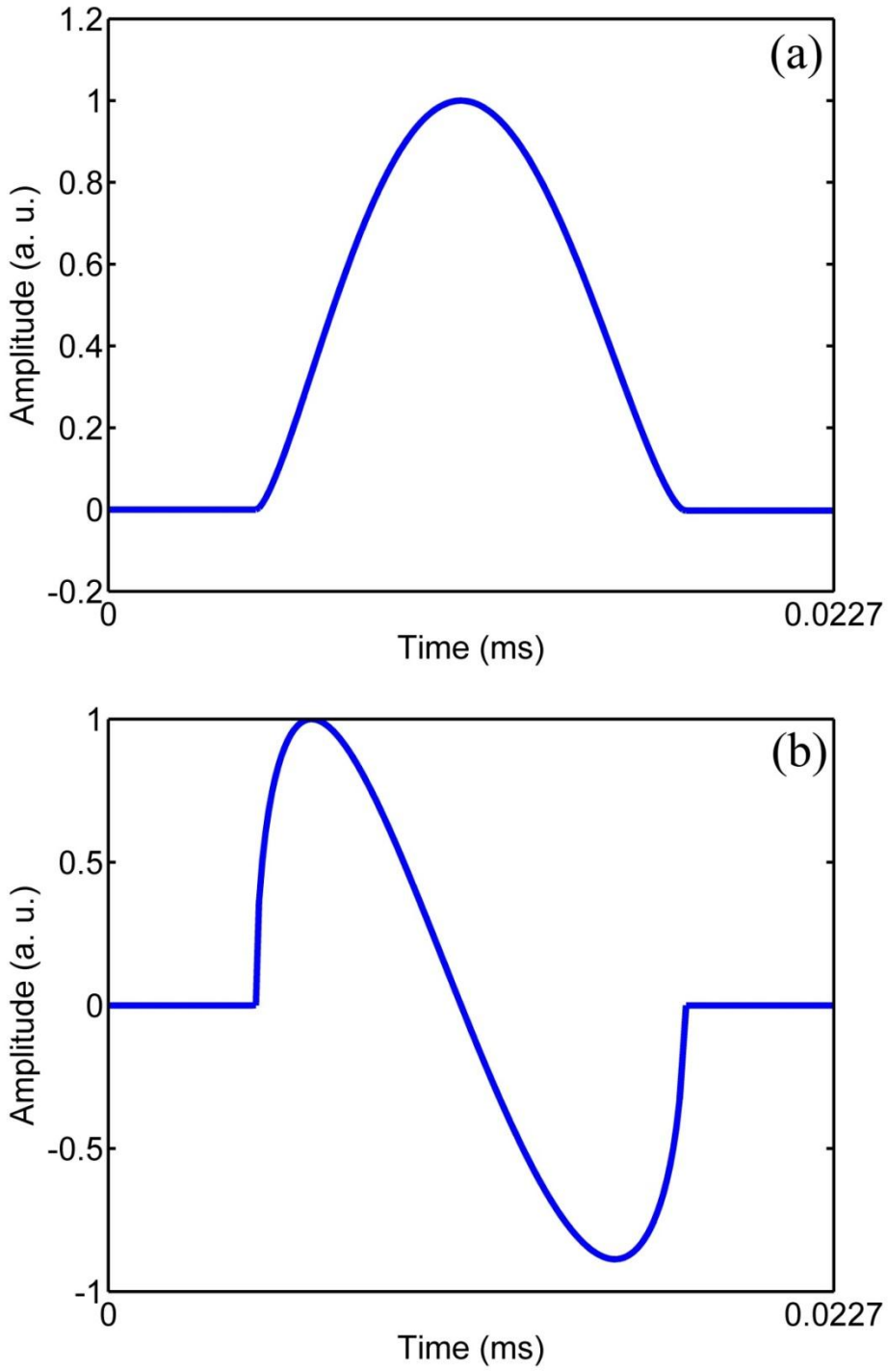

Figure 20: (a) integrated analytical signal of the paraboloid (b) derivative of the signal of (a)

For the simulation a radius of 0.5 cm was chosen and the image resolution was given by 70x70 pixels. The analytically calculated acoustic signal is shown in Figure 20a, which corresponds to an integrated measured signal. An actual measured optoacoustic signal relates to the derivative of the signal depicted in Figure 20a. Similar to the optoacoustic point source signal shown in chapter 2.1.3, the derivative of the signal has an N-shape-like form (Figure 20b). For reconstructing the paraboloid with the back-projection inversion scheme 120 projection angles in a 3 degree step were simulated to cover the paraboloid in full 360 degree tomographic scenario. The ideal paraboloid is shown in Figure 21a, whereas the back-projection based reconstruction of the analytically calculated signals is depicted in Figure 21b. At the border of the paraboloid the typical negative absorption artifact of back-projection can be observed. Additionally around the paraboloid an undesired texture is visible, which relates to the noise amplification effect (here numerical errors generated during the calculation of the analytical signal) of the back-projection algorithm.

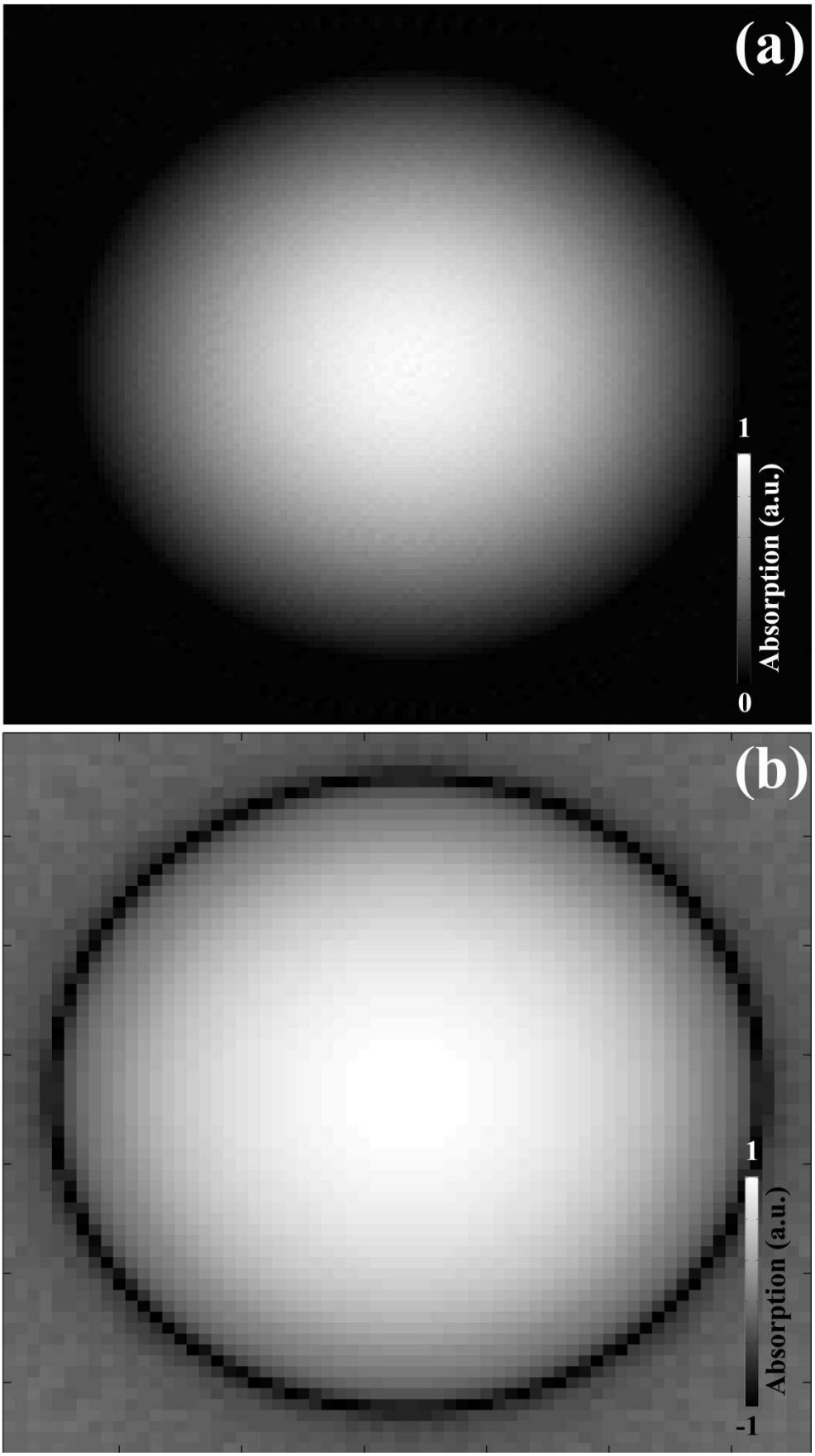

Figure 21: (a) Ideal image of the paraboloid (b) Reconstruction of the paraboloid using back-projection

3.3.2 Interpolated model matrix inversion (IMMI)

Although back-projection generates artifacts in reconstructed images, this has not prevented its use for biomedical applications. Naturally, these artifacts limit the capability of OAT in terms of quantification, image fidelity and the accurate utilization of methods for functional and molecular imaging applications [31]. For multispectral imaging methods the aspect of quantification is very important for example to differentiate a molecular probe from the background absorption of tissue [39]. The source of the artifacts in back-projection is based on the ideal description of the wave propagation and detection geometry [39]. Furthermore, back-projection works only for specific detection geometries and cannot be easily generalized into more realistic optoacoustic illumination-detection models that incorporate configuration and instrumentation-dependent effects [39]. To solve these issues the interpolated model matrix inversion scheme (IMMI) was introduced by Rosenthal and Dima *et al.* [31, 77]. This chapter provides a discussion on the derivation of this algorithm.

3.3.2.1 Modeling the forward problem

As mentioned in the previous section the measured optoacoustic signal is a superposition of waves generated by acoustic sources lying on a sphere for 3D or in a circle for 2D with a radius of *ct* and a center at r_0 (Figure 19). For our forward model, a cylindrically focused transducer and an illumination along the focal plane of the transducer are assumed. By using these constraints the model can be solved for two dimensions [31, 77]. To model the forward problem for a specific sensor position at time *t* it is necessary to integrate over an arc, which is intersecting the image space and then taking the derivative. For modeling the forward problem, equation (3.4) can be simplified [31, 77]

$$p(\vec{r}_0,t)=\frac{\Gamma}{4\pi c}\frac{\partial}{\partial t}\int\frac{H_r(\vec{r}',t)}{R}dl' \tag{3.15}$$

where *l* is the arc along which the integration is performed and R is defined by $R = ct$. For a better understanding a sketch is shown in Figure 22

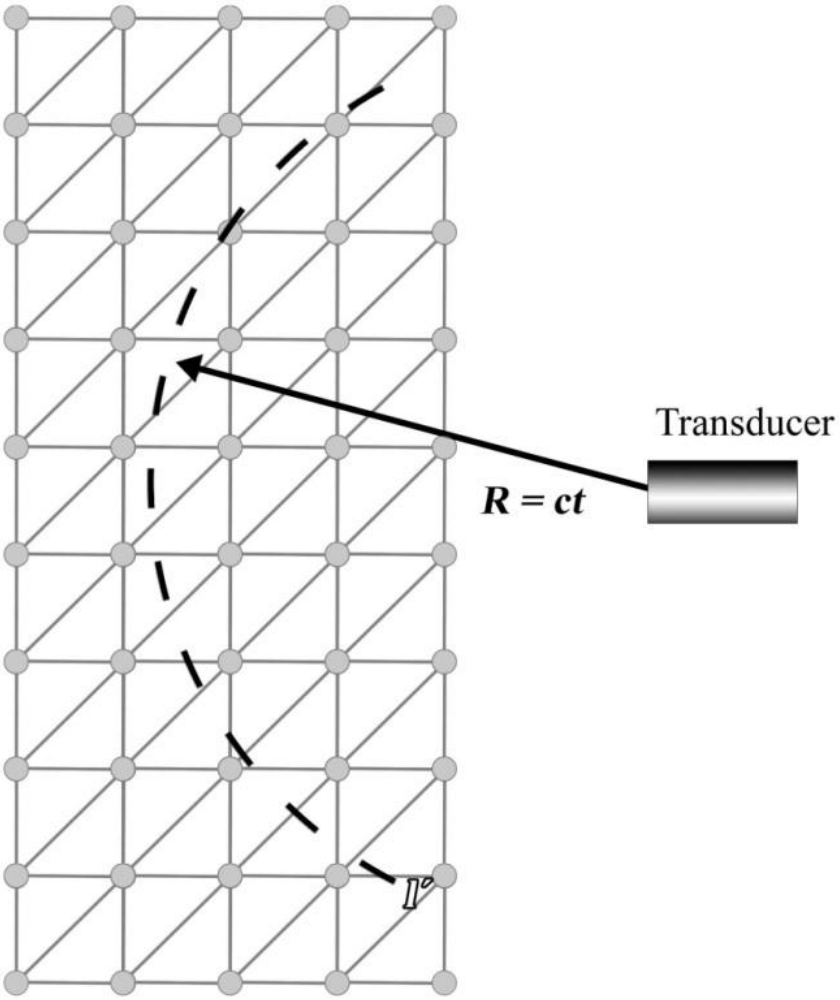

Figure 22: Initial sketch to model the forward solution

For implementing the integration of equation (3.15), first a margin ε is defined. In the second step two concentric circles are defined with the radii of $R \pm \frac{\varepsilon}{2}$ and the center at r_0 (Figure 23). These margins can be formally defined as [31, 77]

$$R - \frac{\varepsilon}{2} \leq \left| \vec{r}' - \vec{r}_0 \right| \leq R - \frac{\varepsilon}{2}, \varepsilon \ll R \tag{3.16}$$

Now all points between these two circles are summed up for the integration. The integration in discrete space can be written as the following function [31, 77]

$$f(t) = \sum_i H(r_i)\Big|_{R\pm\frac{\varepsilon}{2}} \tag{3.17}$$

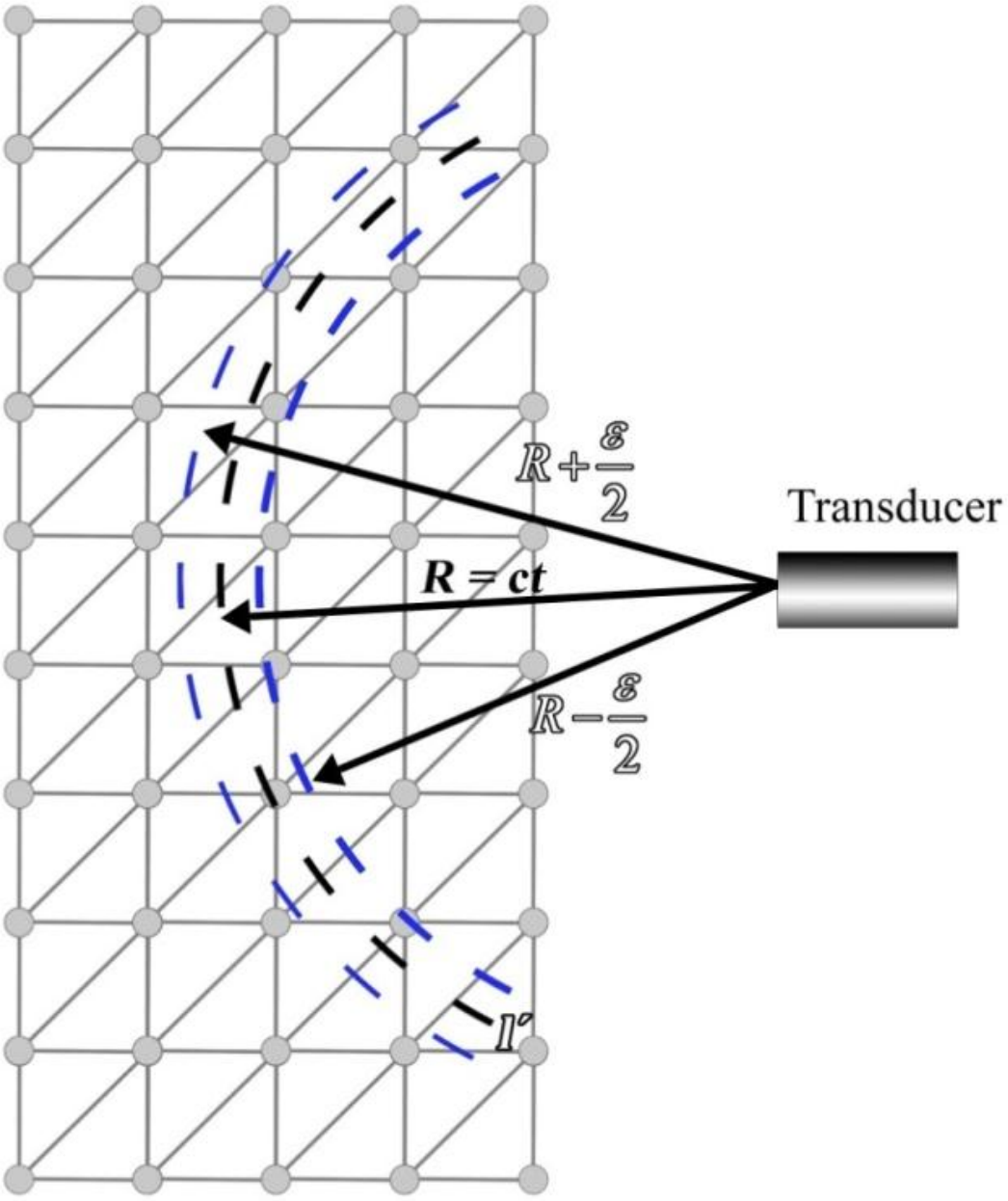

Figure 23: Modeling integration and time derivative

The time derivative can be calculated numerically by computing *f(t)* for two different times t_1 and t_2 [31, 77]

$$t_1 = t - \frac{\Delta t}{2} \text{ and } \qquad t_2 = t + \frac{\Delta t}{2} \tag{3.18}$$

with equations (3.16) and (3.18) the derivative can be defined as

$$ct_1 - \frac{\varepsilon}{2} \le \left|\vec{r}' - \vec{r}_0\right| \le ct_1 + \frac{\varepsilon}{2}, \varepsilon \ll ct \tag{3.19}$$

$$ct_2 - \frac{\varepsilon}{2} \le \left|\vec{r}' - \vec{r}_0\right| \le ct_2 + \frac{\varepsilon}{2}, \varepsilon \ll ct \tag{3.20}$$

with equations (3.17), (3.19) and (3.20) we can define the pressure received at r_0 at time t in discrete space as [31, 77]

$$p(\vec{r}_0, t) = \frac{Q}{\Delta t}\left(\sum_i^{n_2} H(r_i)\Big|_{ct_2 - \frac{\varepsilon}{2} \le \left|\vec{r}' - \vec{r}_0\right| \le ct_2 + \frac{\varepsilon}{2}} - \sum_i^{n_1} H(r_i)\Big|_{ct_1 - \frac{\varepsilon}{2} \le \left|\vec{r}' - \vec{r}_0\right| \le ct_1 + \frac{\varepsilon}{2}} \right) \tag{3.21}$$

where Q corresponds to the constants of equation (3.15), $\Delta t \ll t$ and n_1, n_2 are the optoacoustic sources between the defined arcs for the integration (Figure 24).

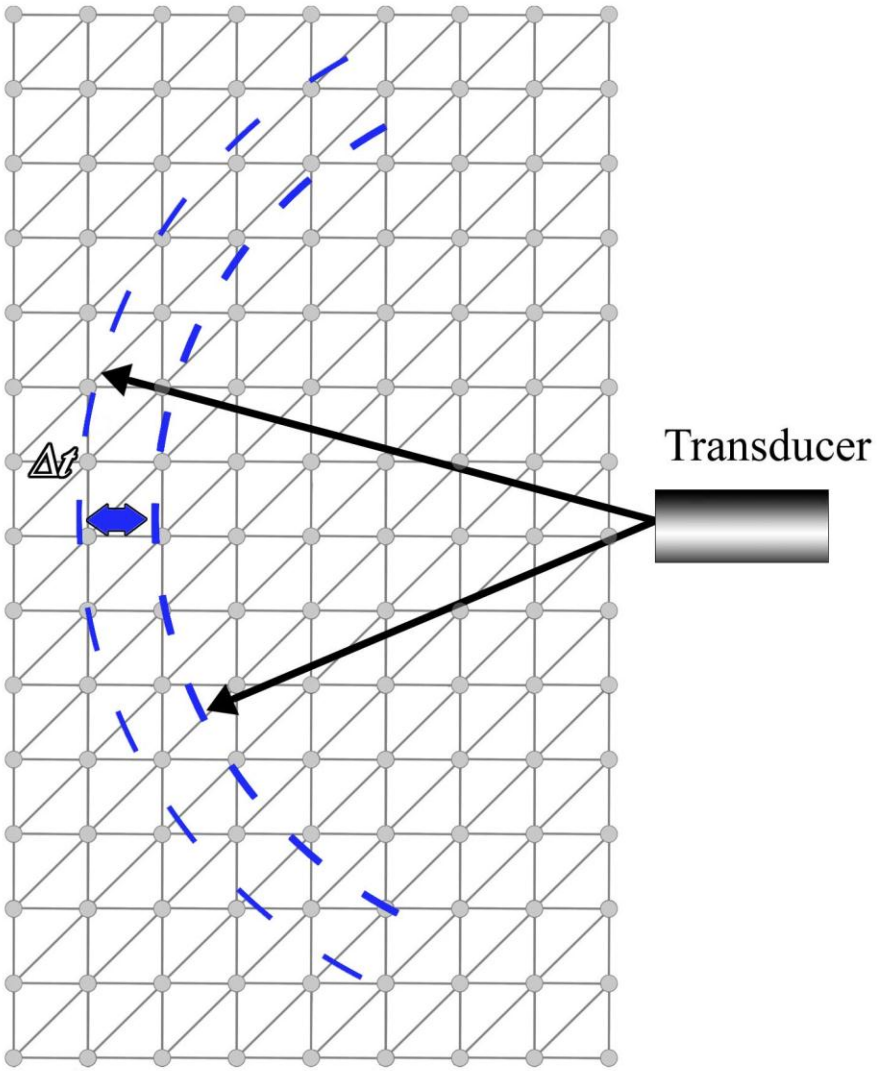

Figure 24: Time derivative in discrete space

As equation (3.21) is a linear combination of sources, a matrix vector multiplication can be used to describe all combinations of sensor positions and sampling times [31, 77]. For the matrix *M*, which shall represent the forward model, the dimensions of the image in terms of grid points (pixels) are defined as *n*. The number of grid points are defined as n^2, because only square images are reconstructed [31, 77].

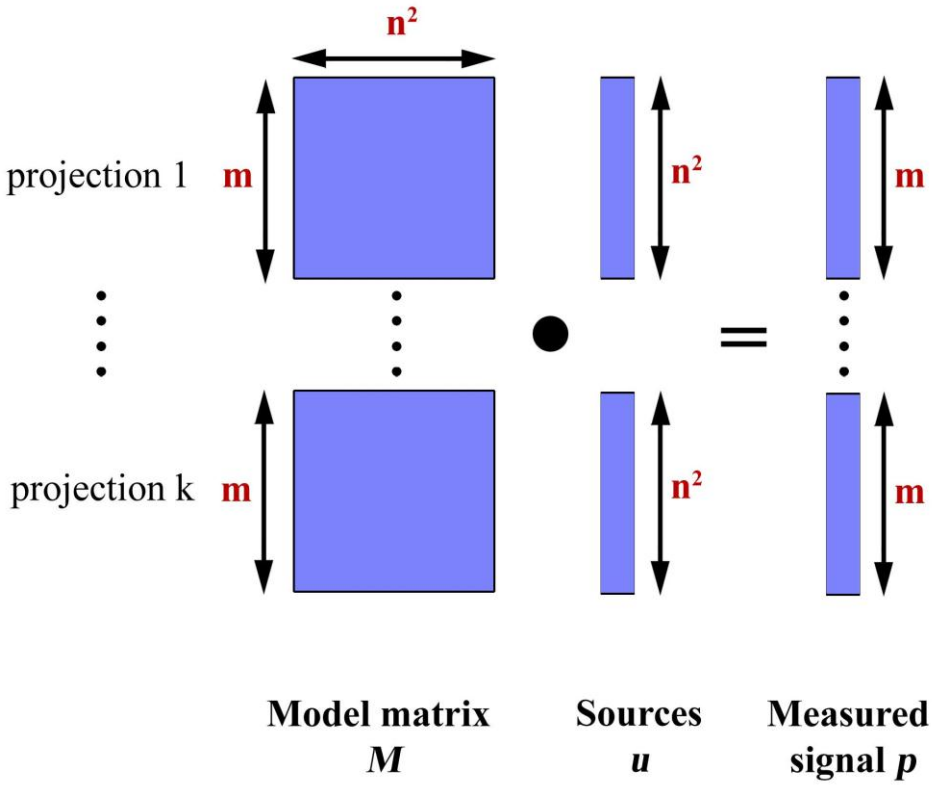

Figure 25: Linear system of equations

With matrix *M*, the vector of pressure sources *u* and the measured signals *p* can be defined as [31, 77]

$$\mathbf{M}u = p \tag{3.22}$$

The number of tomographic projections is defined as *k*, each with *m* time samples (Figure 25). With this, size *a* of the model matrix can be calculated in bytes by [31, 77]

$$a = kmn^2 8 \tag{3.23}$$

where we assume the matrix elements are in double precision floating-point format.

3.3.2.2 Modeling system characteristics into the model

Using a matrix model representation of equation (3.15) provides significant advantages compared to analytical solutions like back-projection. With a model matrix it is possible to take into account a wide range of experimentally related effects. One important effect is the spatial impulse response of the whole system, which includes the frequency calibration of the ultrasonic sensor used [31, 52]. Not taking these system characteristics into account can result in artifact-loaded reconstructions.

To model the impulse response of the system it is necessary to adequately acquire the characteristics. Rosenthal *et al.* described [52] several methods to measure the frequency response for ultrasonic systems. The acquired impulse response is subsequently convolved with the model matrix ***M*** projection wise.

$$p^k = (\mathbf{M}^k * h)u\,, \tag{3.24}$$

where p^k is a column vector representing the acoustic fields measured for projection k at r_k (k=1…K), for a set of times $\{t_i\}$ (i=1…I): $p_i^k = p(r_k, t_i)$; h is a matrix containing the impulse response for each spatial position, u is a column vector representing the values of the optoacoustic image on the grid $u_j = H(r_j)$ (j=1:…J), M^k is the acoustic forward-model matrix for a detector at r_k and * is convolution operator which convolves impulse response h with the model matrix (Figure 26).

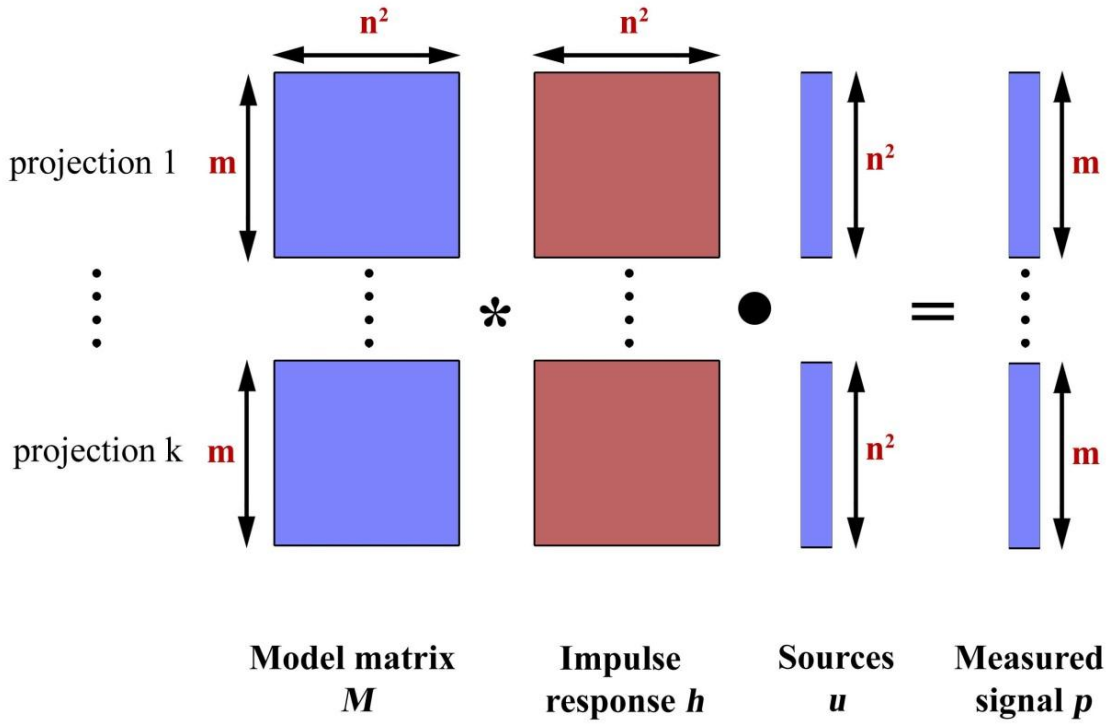

Figure 26: convolving the forward matrix with the impulse response

3.3.2.3 Matrix inversion

In order to obtain the optoacoustic image, equation (3.22) needs to be inverted. Two commonly used methods are the Moore-Penrose pseudo-inverse [78] and the LSQR (least squares QR decomposition) algorithm [79] . For the Moore-Penrose pseudo-inverse it is necessary to calculate the pseudo-inverse of **M.** The pseudo-inverse is given by [31, 76]

$$\mathbf{M}^{+} = (\mathbf{M}^{H}\mathbf{M})^{-1}\mathbf{M}^{H} \tag{3.25}$$

After the pseudo-inverse is calculated, the reconstructed optoacoustic image can then be readily obtained by

$$u = \mathbf{M}^{+} p \tag{3.26}$$

The main advantage of using the pseudo-inverse is that it needs to be calculated for a given system only once. Thus, if the pseudo-inverse is pre-calculated, the inversion can be performed in real time.

LSQR is an iterative algorithm for solving linear equations [79]. Analytically, LSQR is identical to the conjugate gradient method. However, numerically LSQR was found to be more stable. The main advantage of LSQR is its high efficiency in the case of sparse matrices. In addition, the operation performed in LSQR require saving only the non-zero elements of the matrix in memory, thus mitigating memory requirements. Since the model matrix **M** is sparse [31], LSQR is an extremely efficient method for inverting equation (3.22) when the number of grid points is high [31, 76].

To compare the performance of IMMI with back-projection, the analytical signals introduced in chapter 3.3 were reconstructed using IMMI and LSQR. Figure 27 depicts the reconstruction of the paraboloid using the same parameters as for back-projection. The IMMI reconstruction shows no deficits in terms of negative absorption and also no undesired texture appears around the paraboloid.

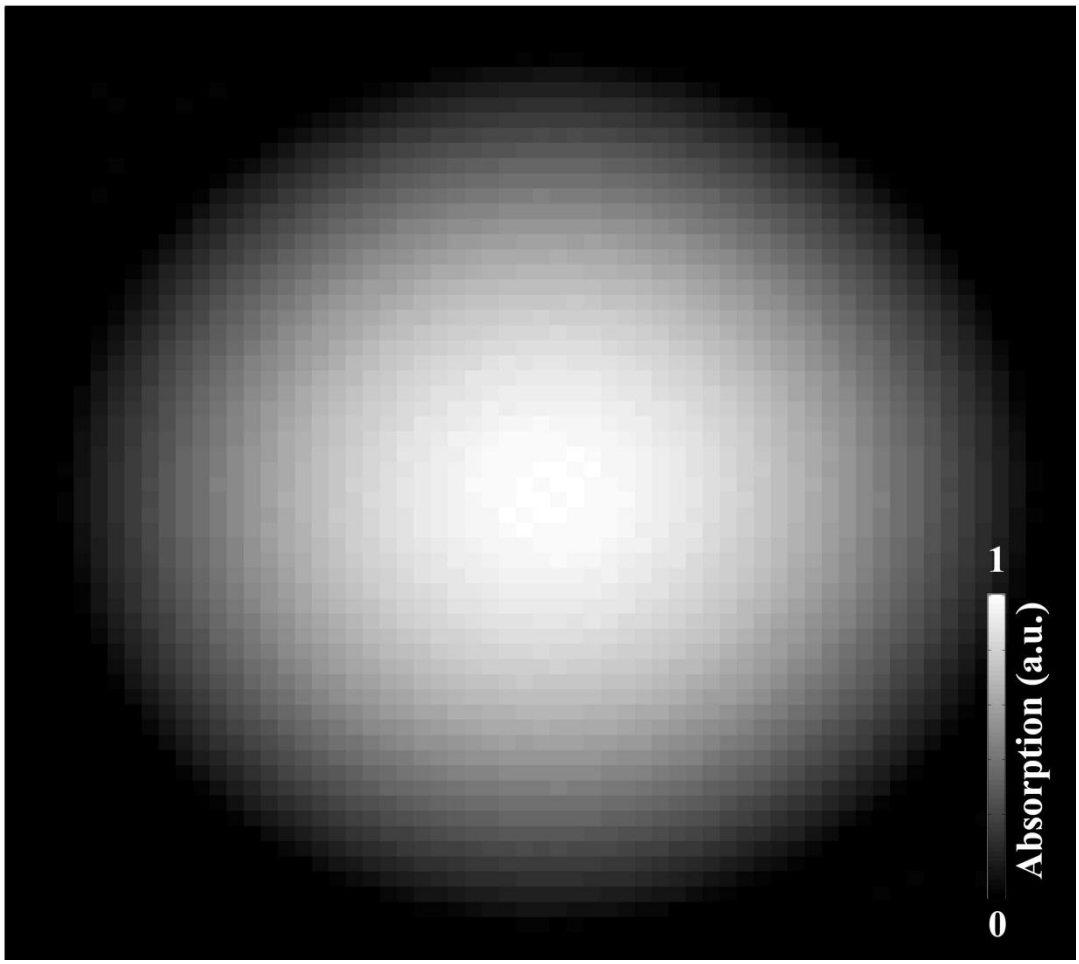

Figure 27: reconstruction of the analytical test function using IMMI

3.3.3 Weighted IMMI

OAT reconstructions are usually very sensitive to various instrumentation and configuration-related parameters, such as the shape of the object‘s illumination, transducer layout, its frequency response and sensitivity fields, as well as laser source stability. Many approximated inversion schemes, including the commonly used back-projection algorithms [29] are not suitable for accurately describing the optoacoustic tomographic problem. If these deviations become substantial, then unquantified or generally erroneous reconstructions may arise. It has been shown that a variety of configuration-related parameters could be taken into account when using exact model-based reconstruction schemes [80]. With the recent introduction of numerically efficient interpolated-model-matrix inversion (IMMI) [31], these methods are no longer afflicted with long computation times [76].

When considering the effects of object illumination, optoacoustic image quality and quantification abilities normally depend on homogeneity and uniformity of excitation light distribution. This is especially important in cases of varying illumination, e.g. when the imaged object is rotated with respect to both illumination and ultrasound detection elements [81]. In an ideal optoacoustic tomography scenario, the imaged region would be perfectly illuminated, which can be achieved by expanding, for example, the laser beam to an appropriate width to cover the entire object. However, this solution is only suitable if the laser power is strong enough so that an appropriate signal-to-noise (SNR) ratio can be attained after beam widening. Yet, even if the laser power is too weak for these optimal illumination conditions, the object can still be imaged by partially illuminating it. Overall, in many realistic imaging cases, where large parts of the object are not accessible for light or its geometry is not suitable for uniform illumination, a sub-optimal partial illumination arrangement is the only method to actually perform optoacoustic imaging at the expense of reduced tomographic quality of the data. Similar issues are arising regarding the sensitivity fields of the transducers

used for optoacoustic detection. These are generally not homogenous and have strong dependence not only on the distance from the detector but also on the detection angle [82] [76].

Herein a modified model-based reconstruction algorithm is presented, which is based on integrating an additional weight in the optoacoustic forward model by weighting the elements in the model matrix. Our main focus here is on light-related reconstruction effects. However, the proposed method can equally be used in other scenarios, e.g. for spatially dependent sensitivity which varies for different positions of the acoustic detector. Improvements in the image fidelity and quantification are demonstrated based on both numerical simulations and experiments using realistic tissue-mimicking phantoms and mice [76].

It has been previously shown that model-based reconstruction approach can be readily generalized to include linear effects that characterize the optoacoustic imaging system. Specifically, the frequency response of the detector was taken into account [31] by assuming it did not vary significantly within the imaged region. Thus, in that generalization, the sensitivity of the detector to each point in the imaged object was assumed to be the same. While this first order approximation yielded good initial results, in many scenarios the spatial variations in the object‘s illumination and detection sensitivity are too large to be neglected, thus requiring additional modeling[76].

A typical example of imaging configuration, in which modeling the spatially-dependent sensitivity is crucial, occurs when the illumination differs for each projection [83] (Figure 28a). While uniform illumination is considered to be the best theoretical choice, it might not be practical due to technical constraints. For instance, if the laser power is not sufficiently strong, expanding the beam to allow for uniform illumination of the imaged object will decrease the beam's intensity, readily resulting in lower SNR, reduced image quality or significantly prolonged reconstruction times due to signal averaging. Since in many practical

cases not all of the generated optoacoustic fields are detected simultaneously, the SNR can be significantly improved by illuminating only the parts of the object that are best detected in each particular projection of the imaging geometry [76].

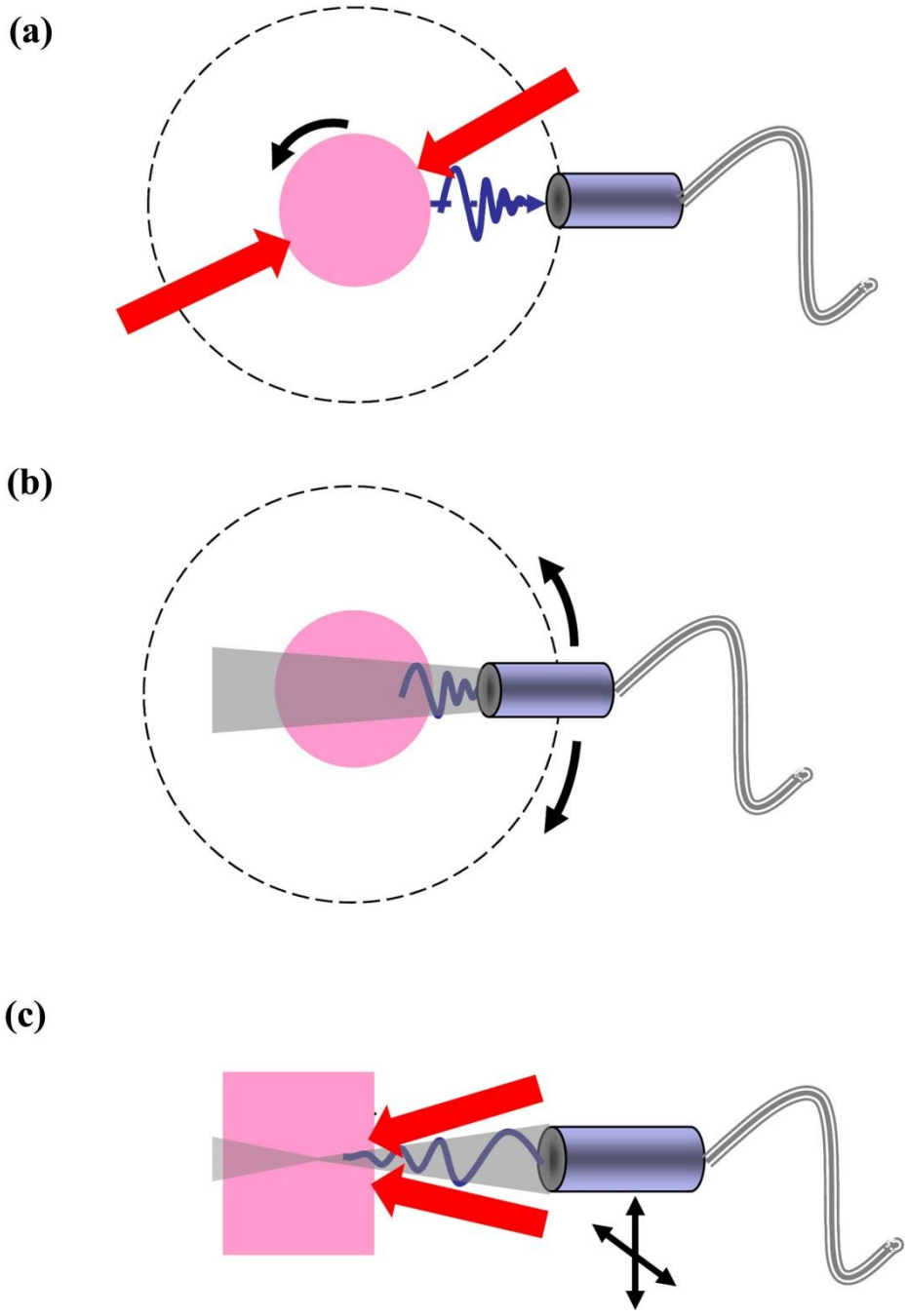

Figure 28: Optoacoustic imaging configurations with partial or variable tomographic data. (a) Circular scanning with narrow laser beam and a rotating object. Illumination and detector are static; (b) Circular scanning with ultrasonic detector having limited angular view, the imaged object and illumination being static; (c) Optoacoustic microscopy (B-mode) imaging with confocal illumination-detection geometry and linear translation (Reprinted with permission from [76]. Copyright 2010, Optical Society of America).

Similar considerations apply to ultrasonic detection. Spatial dependence is a common attribute of conventional acoustic transducers used for optoacoustic detection. Generally, the dependence is not only upon the distance from the detector but also on the detection angle [82]. This dependence can be mitigated by placing the transducer farther from the sample, however, such a solution comes on the expense of SNR. Thus, similar to the case of non-uniform illumination, there is a tradeoff between uniform sensitivity and maximum sensitivity, which might result in a limited view acoustic detection scenario (Figure 28b) [76].

In some cases, incomplete tomographic data is obtained due to both partial illumination and limited-view or focused acoustic detection. A typical example is the dark-field photoacoustic microscopy (PAM) [84] where both illumination and sound detection are confined to a relatively small focal region, which is also translated along the object‘s surface in order to capture three-dimensional image data (Figure 28c) [76].

An additional spatially-dependent effect is acoustic attenuation. Because acoustic attenuation depends on the distance of the source from the detector, its effect may be different for different regions in the imaged specimen. This effect may become significant in imaging animal such as mice and when imaging fatty tissue, which has a relatively high attenuation coefficient [85],[76].

When the spatially-dependent sensitivity of the detection is known, it can be incorporated into the model matrix of IMMI by weighting its elements. Denoting the weight function by $W^k(r)$, the weighted model-matrix elements are given by [76]

$$\breve{\mathrm{M}}_{ij}^{k} = W^{k}(r_j)\breve{\mathrm{M}}_{ij}^{k} \tag{3.27}$$

where r_j are the location of the grid points. The matrices $\breve{\mathrm{M}}^k$ ($k=1...K$) can be used to construct the total weighted matrix $\breve{\mathrm{M}}$ as shown in Figure 29: $\breve{\mathrm{M}} = [\breve{\mathrm{M}}^1, \breve{\mathrm{M}}^2, ..., \breve{\mathrm{M}}^K]$. The forward matrix M from equation (3.22) is then replaced with the weighted matrix $\breve{\mathrm{M}}$ and

inverted by using either the Moore-Penrose pseudo-inverse equation (3.25) or the LSQR algorithm [76].

The total amount of optical energy transferred to the imaged object from a single light pulse at a point *r*, is given by equation [76]

$$H(r) = \mu_a(r)U(r) \tag{3.28}$$

where *H(r)* is the optoacoustic image, *U* is the light intensity and μ_a is the optical absorption coefficient. In the case in which the illumination changes as a function of the position of the acoustic detector [83] (Figure 28a), the weighting function can be numerically calculated. The optoacoustic image for the *k*-th position of the detector (projection) is given by [76]

$$H^k(r) = \mu_a(r)U^k(r) \tag{3.29}$$

The optoacoustic image for each value of *k* can be presented as a function of the image in the case of uniform illumination[76]:

$$H^k(r) = H(r)W^k(r) \tag{3.30}$$

where the weight function $W^k(r)$ is given by $W^k(r) = U^k(r)/U(r)$. In order to calculate $W^k(r)$, a diffusion approximation must be obtained: once for uniform illumination and once for the specific illumination pattern of the *k*-th projection (Figure 29). For practical cases the exact fluence pattern can only be calculated if the absorption and scattering coefficients are known, while it can be approximated by using typical values for these coefficients. The approximation can be subsequently improved by using the reconstructed optoacoustic image to get a better estimate for the absorption coefficient and to calculate $W^k(r)$ in iterations [86] [76]. A general approach to model the light fluence is presented in chapter 4.2, however here it is assumed the light fluence *U* can be calculated numerically by using appropriate scattering

and absorption coefficients. A general overview of the performance of the presented inversion schemes is shown in chapter 5.2.

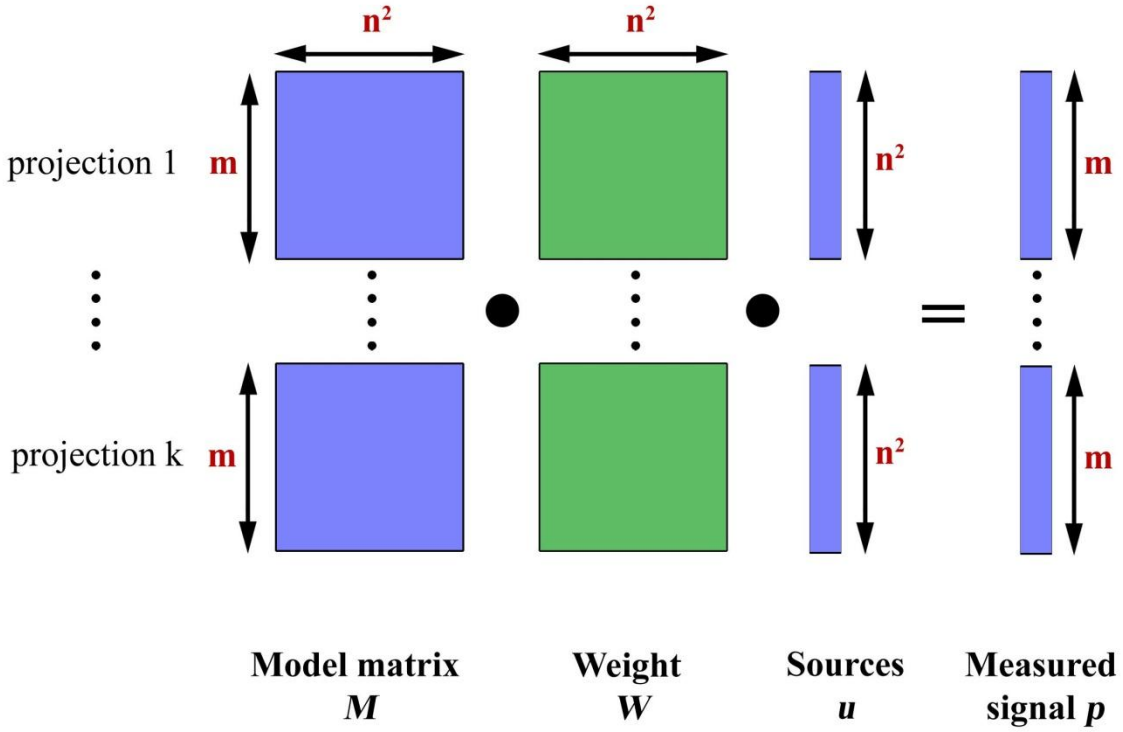

Figure 29: Structure of a matrix representing the weighted forward-model approach.

To numerically demonstrate the proposed reconstruction algorithm for the partial illumination I used the configuration shown in Figure 28a. All the inversion algorithms were implemented in Matlab (Mathworks Inc., Natick, MA), and executed on an Intel® Core™2 Quad Processor CPU operating at 2.67GHz with 4 Gbyte of RAM. All the model-based reconstructions were obtained using LSQR for inversion[76].

The algorithm is numerically tested for a round tissue-mimicking phantom containing two square inclusions with higher absorption compared to the background. The bulk of the phantom was assigned an absorption coefficient of μ_a=0.2cm^{-1}, whereas the top and bottom insertions had absorption coefficients of 0.6 cm^{-1}, and 0.4 cm^{-1}, respectively. The scattering coefficient was chosen to be constant and had the value of 10 cm^{-1}. Figure 30a and Figure 30b show the reconstructions obtained using standard IMMI [31] and the back-projection

algorithm [29] assuming constant and uniform surface illumination and circular detection geometry with 180 projections. As expected, the model-based approach achieves an almost exact reconstruction, whereas the back-projection algorithm suffers from negative artifacts and does not correctly capture the effect of light attenuation, making the image non-quantitative [76].

I simulated the non-uniform illumination using two beams coming at angles of 20° and 200° relative to the detector, and having widths of 0.75 cm and 1 cm, respectively (Figure 28a). We simulated the light beams and detector to encircle the imaged object with 2° increments to acquire a full optoacoustic tomographic data set. Figure 30c shows the light fluence for the projection in which the detector is positioned as in Figure 28a (3 o'clock orientation). Clearly, over half of the phantom's boundary is not illuminated. The reconstructions obtained using standard IMMI and back-projection are shown in Figure 30d and Figure 30e, respectively. While the filtered back-projection algorithm yields a non-quantitative image similar to the obtained in Figure 30b, the accuracy of the model-based reconstruction significantly deteriorates as compared to Figure 30a with a loss of contrast and blurring artifacts [76].

In order to correct for non-uniform illumination, the fluence ought to be approximated for both the non-uniform and uniform illumination geometries. Since the exact map of optical absorption distribution is not *a-priori* known in optoacoustic experiments, the light diffusion equation was solved for a phantom with estimated background absorption and scattering coefficients: μ_a=0.2cm^{-1}, μ_s‘=10cm^{-1}. The illumination profile, which can be measured experimentally, was modeled exactly according to the one used to generate the optoacoustic data. The approximated fluences were used to calculate a weight function $W^k(r)$, which was incorporated into the model using equations (3.27)-(3.30). The reconstruction obtained using weighted IMMI is shown in Figure 30f. Despite the rough estimation of the optical properties

used for modeling of light propagation, the corrected image shows a significant improvement in the reconstruction quality, which is comparable to the one obtained for uniform illumination (Figure 30a) [76].

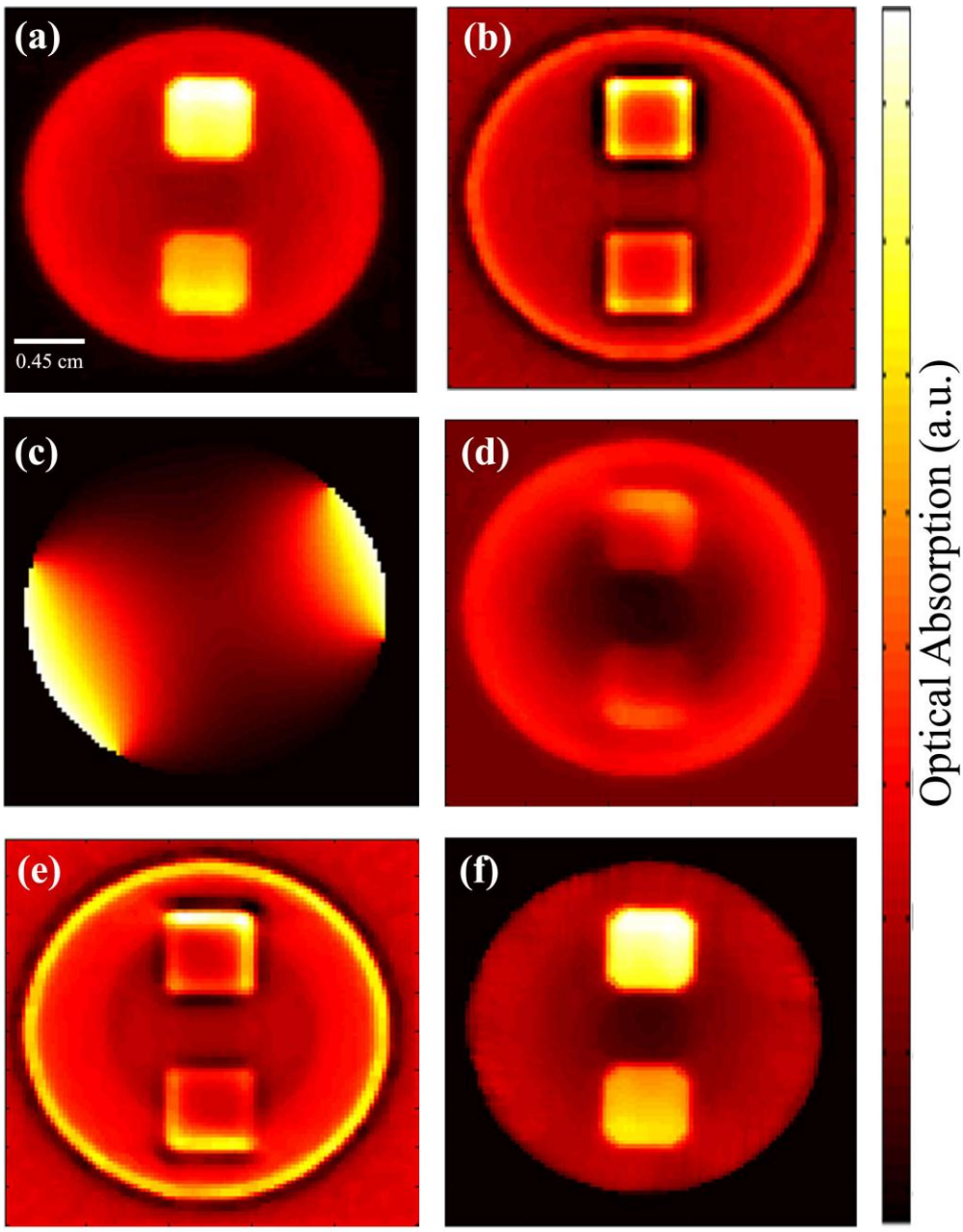

Figure 30: Reconstructions of the numerical tissue-mimicking phantom for the homogeneous illumination case with (a) model-based (b) back-projection, (c) light propagation model used in the simulated partial illumination case for weighting and correction; (d) reconstruction with back-projection for partial illumination; (e) standard model-based reconstruction with partial illumination; (f) image corrected for partial illumination using the weighted model-based approach (Reprinted with permission from [76]. Copyright 2010, Optical Society of America).

4. Image normalization in non-uniform illumination configurations

The main challenge in the quantification of molecular probes in optoacoustic tomography is the bias introduced by light attenuation. As stated in chapter 2.2.2, in top illumination systems this effect is not dominant at least for superficial tomographic images. Nevertheless, imaging deeper regions still suffer from the effect of inhomogeneous light distribution in tissue. By using the more flexible multi-side illumination in optoacoustic tomography the need to correct for the effect of light attenuation is of great interest for quantifying optoacoustic images. In the following chapter several methods are presented to correct for the light attenuation. As shown by equation (3.28) an optoacoustic image can be defined by the light absorption $\mu_a(r)$ and the energy transported to each voxel $U(r)$. An image, which is normalized for the light attenuation can be acquired by the following equation

$$\mu_a(r) = \frac{H(r)}{U(r)} \tag{4.1}$$

where H is again the optoacoustic image. The key to correct for the light attenuation is to get an estimate for the light fluence $U(r)$. There are analytical and numerical solutions, which can provide approximations of the light fluence. In this chapter, I discuss widely used methods to correct for the light fluence first. Then, in addition an implementation of an iterative image normalization algorithm is showcased which depicts a good performance for the simulations used in this chapter. In the last subchapter a ratiometric algorithm is shown, which is able to quantify molecular probes in tissue without using analytical or numerical estimations for the light fluence. The discussion of the whole chapter is limited to the algorithm itself and numerical simulations. Experimental results will be demonstrated and discussed in the next chapter.

4.1 Normalization using an analytical solution

An analytical estimation for the light fluence can be given by Bessel functions. To normalize for the light fluence in optoacoustic images, the following analytical solution to the light diffusion in cylindrical illumination configurations can be used [73]

$$U(\vec{r}) = I_0(|k|r) \tag{4.2}$$

where I_0 is the modified Bessel function of the first kind and zero order, k is a coefficient and r is the distance from the phantom´s center in the x-y plane[73]. Analytical solutions for the light fluence can at least increase the image quality visually, but their practical application in complex experiments is very limited especially in quantifying molecular probes. They can only be used for cylindrical objects assuming complete homogeneous surface illumination. Also the physical reality cannot be sufficiently described by Bessel functions, as the light attenuation depends mainly on the dimensionless coefficient k, whereas tissue has non-homogenous optical parameters. Nevertheless, the visual image quality can benefit by using Bessel functions as an approximation for the light fluence.

To showcase the performance of this normalization scheme, I used a numerical tissue mimicking phantom with two insertions. The bulk of the phantom was assigned an absorption coefficient of μ_a=0.4 cm^{-1}, whereas the top and bottom insertions had absorption coefficients of 0.6 cm^{-1}. The scattering coefficient was chosen to be constant and had the value of 10 cm^{-1}. Figure 31a shows a sketch of the geometry of the phantom. The optoacoustic responses were derived using the forward part of IMMI for 360 projections and assuming a homogeneous surface illumination. Figure 31b was reconstructed by using IMMI only for 180 projections. The image had a resolution of 200x200 pixels, with a voxel size of 100 micron. To normalize the image equation (4.2) was used to calculate an approximation for the light fluence U (Figure 31c). To correct for the light attenuation, equation (4.1) was employed and a normalized image was obtained (Figure 31d). To showcase the performance in detail, a plot

along the dashed line of Figure 31a is provided in Figure 31e, which correspond to the ideal values of the numerical phantom. Figure 31f depicts profiles for the uncorrected and corrected optoacoustic image. The normalized image shows a better visual quality compared to the initial image. The quantification of the insertions is still a problem because the coefficient *k* is arbitrarily chosen and it has a huge impact on the quality of the normalization. By knowing *a-priori* the properties of the optoacoustic image, the coefficient could be tweaked until a nearly perfect normalization is achieved. In real applications, there is no information about the optical properties of an imaged object.

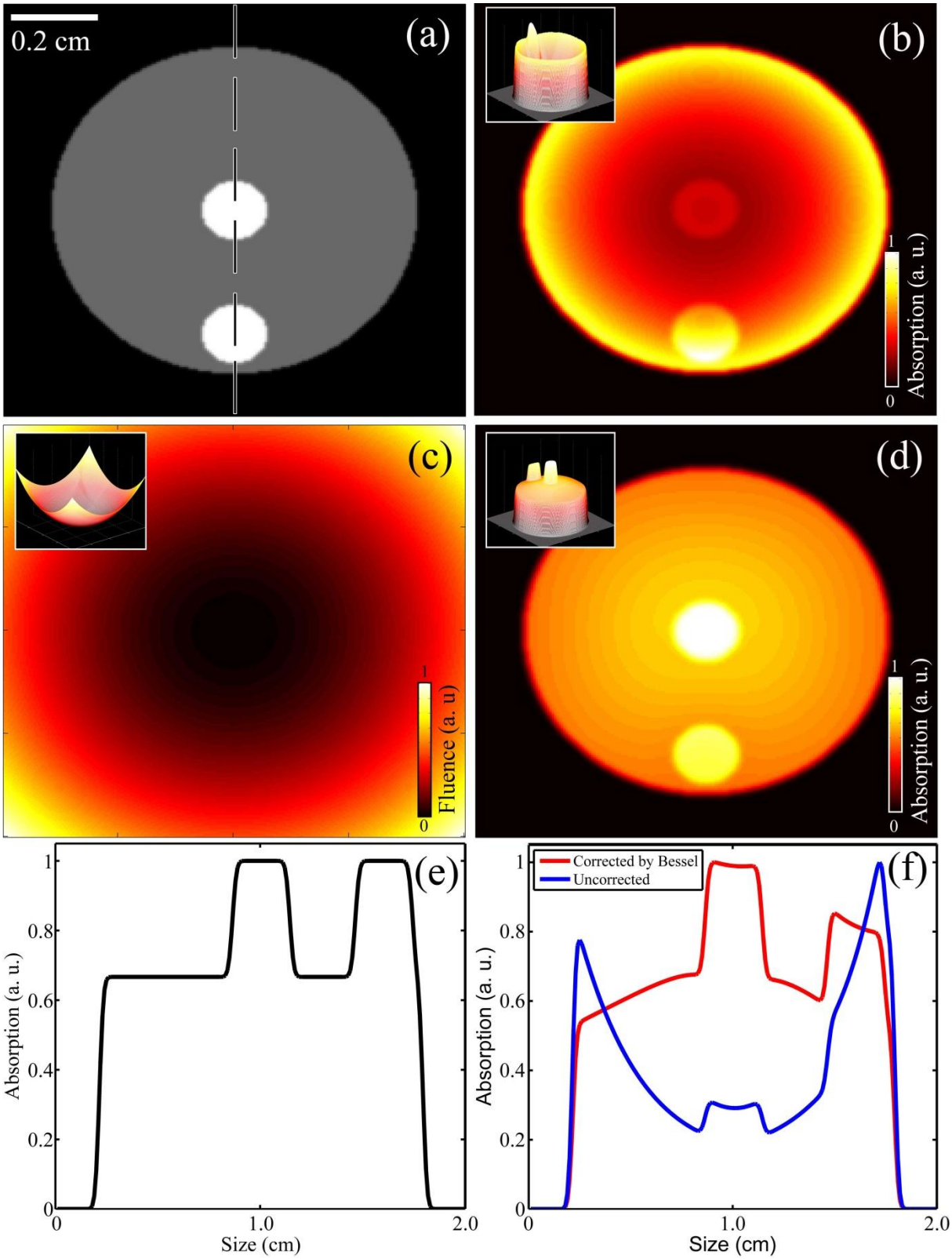

Figure 31: (a) Sketch of the numerical phantom (b) the reconstructed numerical phantom using IMMI (c) the fluence approximated by the Bessel function (d) the normalized optoacoustic image (e) the profile along the dashed line of (a) showing the correct optical absorption of the phantom (f) the profiles for the uncorrected and corrected optoacoustic images along the same line as (e)

4.2 Normalization using diffusion approximation

Modeling the light transportation in tissue is well-studied in the field of biomedical optics. It is of special interest in fluorescence molecular tomography (FMT) as well as other optical imaging fields. As widely discussed in several journals (Optics Letters, Journal of Optical Society of America and Medical Physics), here only a brief overview of the used algorithms is given [1, 9, 11, 12, 73].

To model the light fluence for optoacoustic simulations or to calculate a weight for the weighted IMMI algorithms, a diffusion approximation to light transport equation is assumed [73, 86], i.e.

$$-\nabla D(\vec{r})\nabla U(\vec{r}) + \mu_a(\vec{r})U(\vec{r}) = q_0 \qquad (4.3)$$

where $D = 1/[3(\mu_s'+\mu_a)]$ is the spatially dependent diffusion coefficient of the medium, U is the light intensity, μ_a is the optical absorption coefficient, μ_s' is the reduced scattering coefficient and q_0 is the source term. When the exterior medium is non-scattering, the behavior of $U(r)$ on the interface is given by the Robin boundary condition [87] [76]:

$$U(\vec{r}) + 2D(\vec{r})\hat{\mathbf{n}} \cdot \nabla \cdot U(\vec{r}) = 0 \qquad \vec{r} \in \partial\Omega \qquad (4.4)$$

where $\partial\Omega$ is the boundary of the object and $\hat{\mathbf{n}}$ is a unit vector normal to $\partial\Omega$ and pointing outwards. Clearly, for heterogeneous media, solutions for equation (4.4) can only be obtained numerically. In our work, we used a finite volume method (FVM) solution approach [88] [76].

To showcase the performance of a diffusion approximation by using FVM for optoacoustic image normalization, again I used a numerical tissue mimicking phantom with two insertions. The bulk of the phantom was assigned an absorption coefficient of μ_a=0.4 cm^{-1}, whereas the top and bottom insertions had absorption coefficients of 0.6 cm^{-1}. The scattering coefficient was chosen to be constant and had the value of 10 cm^{-1}. Figure 32a

shows a sketch of the geometry of the phantom. The optoacoustic responses were derived using the forward part of IMMI for 360 projections and assuming a homogeneous surface illumination. Figure 32b was reconstructed by using IMMI for only 180 projections. The image had a resolution of 200x200 pixels, with a voxel size of 100 microns. To normalize the image we used equation (4.2) to calculate an approximation for the light fluence *U* (Figure 32c). To correct for the light attenuation, equation (4.3) was employed by using an estimated absorption for the background of μ_a=0.3 cm^{-1} and a scattering coefficient of μ_s‘=12 cm^{-1} to calculate a light fluence model for a homogeneous background without absorbing insertions. In reality the scattering and absorption coefficients can only be estimated, so for the experiment only flawed values were used to see the performance of the algorithm. By using exact values a perfect normalized image could be calculated. Nevertheless practical experiments lack this information, which could finally be obtained by hybrid systems combining fluorescence molecular and computer tomography[12, 73].

To showcase the performance in detail, a plot along the dashed line of Figure 32a is provided in Figure 32e which corresponds to the optical absorption of the numerical phantom. Figure 32f depicts profiles for the uncorrected and corrected optoacoustic image. The normalized image shows a better performance in terms of visual quality and quantification. The center of the normalized images shows not a heightened structure compared to result of the Bessel normalization. The quantification of the insertion is still not perfect, although it could be improved by using *a-priori* knowledge of other sources. Such hybrid systems are known in other optical imaging modalities for example fluorescence molecular tomography in conjunction with computer tomography [12]. By applying *a-priori* knowledge to the light diffusion model - for example more detailed information about optical properties and beam pattern - the quality of the normalization may be increased.

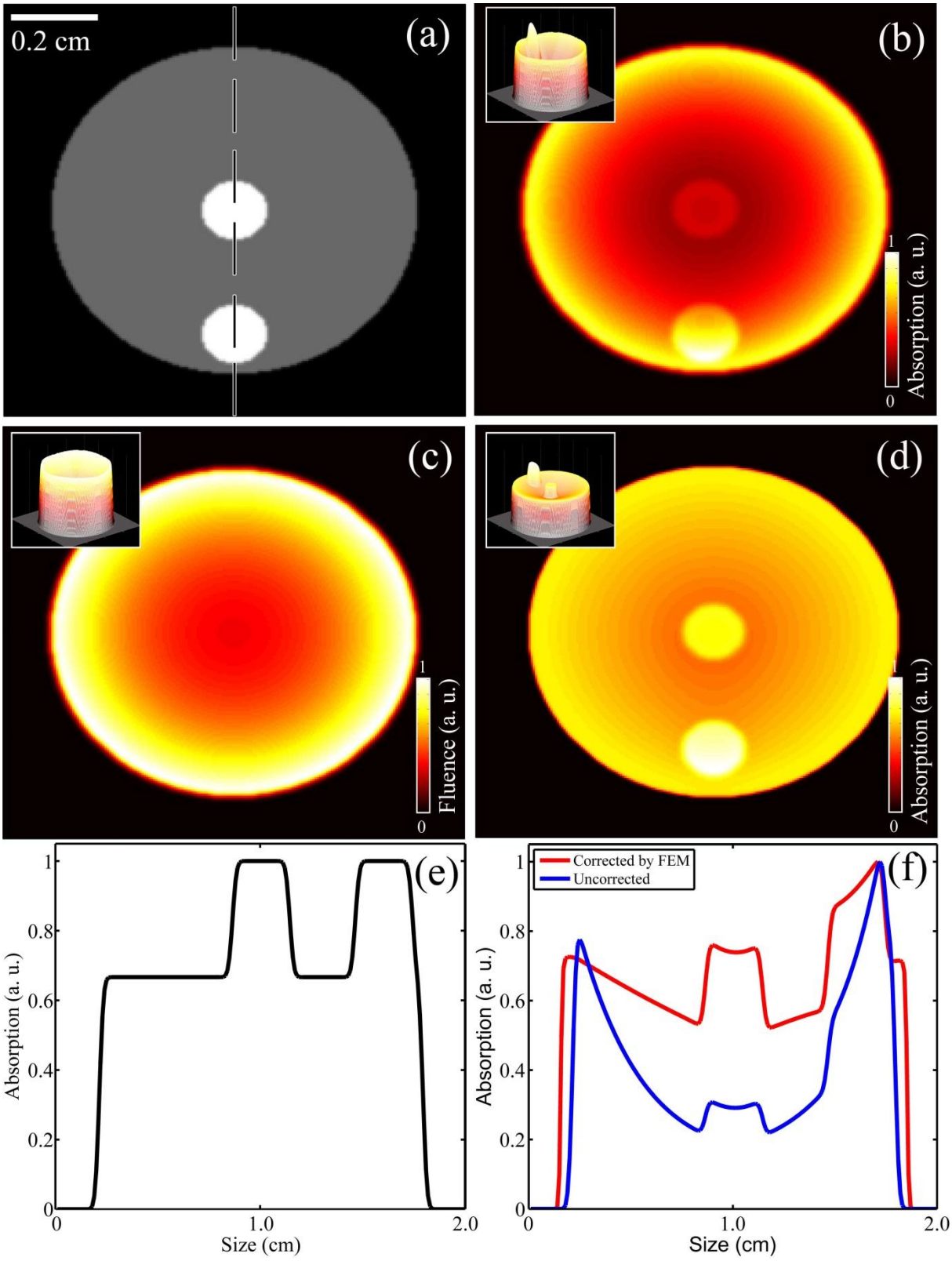

Figure 32: (a) Sketch of the numerical phantom, (b) reconstructed numerical phantom using IMMI, (c) fluence approximated diffusion approximation, (d) normalized optoacoustic image, (e) profile along the dashed line of (a) showing the correct optical absorption of the phantom, (f) profiles for the uncorrected and corrected optoacoustic images along the same line as (e)

4.3 Iterative normalization

Herein, I adopted a method, which is suitable for iterative quantification improvement of optoacoustic images produced from realistic whole-body small animal imaging configurations that naturally have highly heterogeneous light distribution within the imaged volume. The theoretical approach was suggested by Cox *et al.* in Ref. [71] and was adopted in Ref. [70] for small animal scanners like the MSOT I system [55].

For the iterative algorithm an optoacoustic image for a certain iteration is donated by h_i. To reduce complexity, we further assumed that reduced scattering coefficient of the object is known. In that case the light intensity $U(\vec{r})$ through the object depends solely on the absorption coefficient. The iterative approach is then applied at the *i*-th iteration by calculating $U(\vec{r})$ solving equation (4.3) with the absorption coefficient μ_{i-1} obtained at the preceding iteration. The absorption coefficient $\mu_i(r)$ is then calculated using the following equation [70, 71]:

$$\mu_i(r) = \frac{h_i(r)}{U_i(r) + \sigma}, \tag{4.5}$$

where σ is a regularization parameter that prevents possible divergence in the solution due to image artifacts, noise etc.

To test the performance of the iterative algorithm, I examined equation (4.5) with simulated data, for the phantom shown on Figure 33a. The bulk of the phantom was assigned an absorption coefficient of μ_a=0.4 cm^{-1}, whereas the top and bottom insertions had absorption coefficients of 0.6 cm^{-1}. The scattering coefficient was chosen to be constant and had the value of 10 cm^{-1}. The optoacoustic responses were derived using the forward part of IMMI for 360 projections and assumed a homogeneous surface illumination. Figure 33b was reconstructed by using IMMI for only 180 projections. The image had a resolution of

200x200 pixels, with a voxel size of 100 micron. Light distribution was simulated using again the finite element solution of the diffusion equation and optoacoustic responses were derived using the forward part of IMMI. The initial background absorption was estimated by μ_a=0.6 cm^{-1} and a scattering coefficient of 10 cm^{-1} was used for all iterations. The first fluence model, which is used to normalize the initial optoacoustic image in the first iteration, is depicted in Figure 33d. The corrected image is showcased in Figure 33e, which shows in general a poor performance. After the 4th iteration (Figure 33g - Figure 33i) the algorithm has converged and the correction shows a good performance compared to the initial image. The plotted profiles along the dashed line of Figure 33a also show an improvement between the first iteration (Figure 33f) and the 4th (Figure 33i). The algorithm is robust even for randomly choosing the absorption coefficient for the background as long as the estimated coefficient is larger than the correct coefficient. Although the algorithm is robust for the estimate of the background absorption, it is sensitive to the estimate of the scattering coefficient. To showcase the behavior of the iterative normalization, a scattering coefficient of 15 cm^{-1} was selected and the result depicted in Figure 33j – Figure 33l. Instead of converging after several iterations, the normalization scheme starts to diverge after the 2nd iterative step. It can be concluded that the algorithm shows a good performance as long as detailed information about the light scattering can be provided.

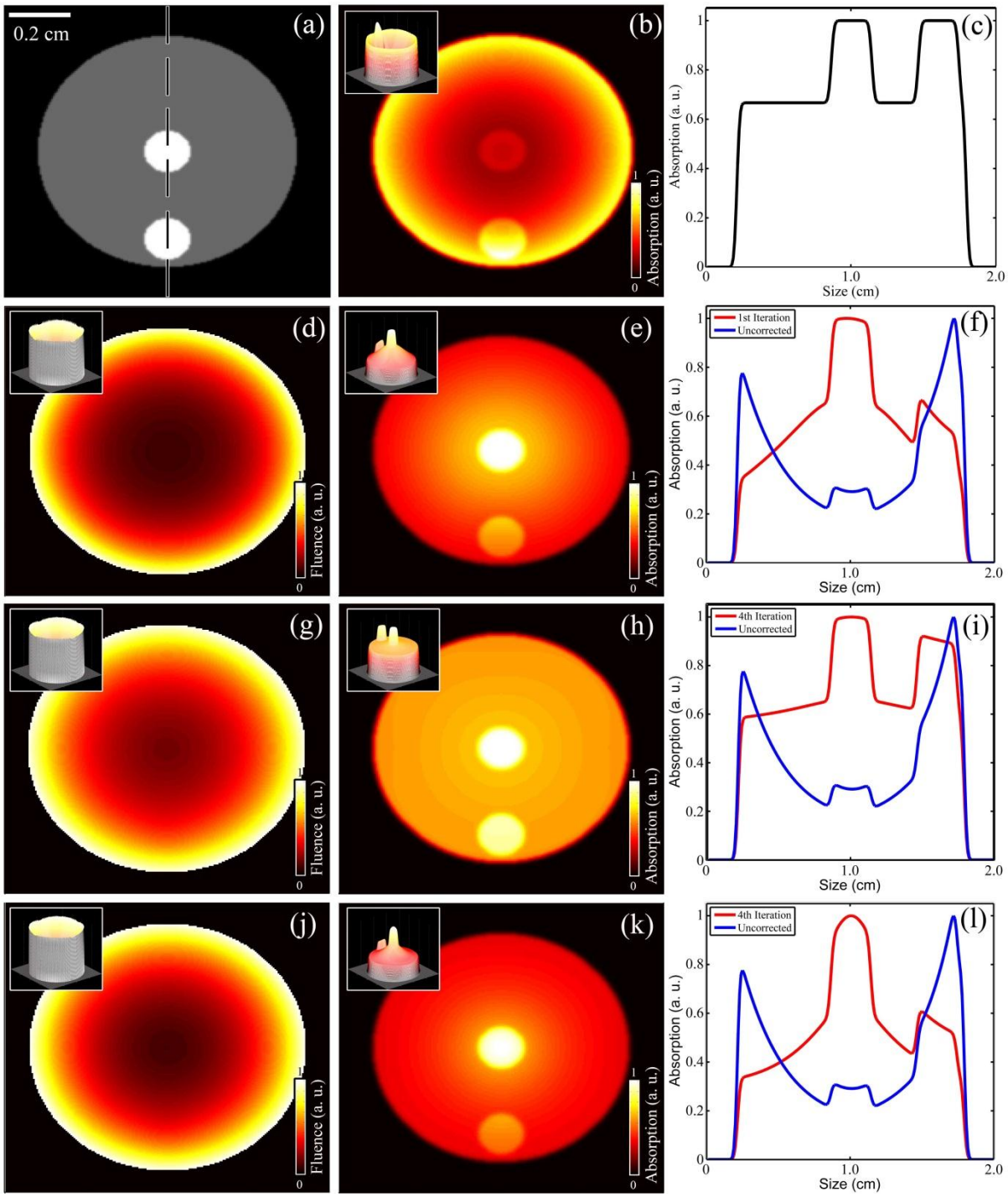

Figure 33: (a) Sketch of the numerical phantom, (b) reconstructed numerical phantom using IMMI, (c) profile along the dashed line of (a) showing the correct optical absorption of the phantom, (d) fluence calculated with diffusion approximation for the 1st iteration, (e) normalized optoacoustic image for the 1st iteration, (f) profiles for the uncorrected and corrected optoacoustic images along the same line as (c) for the 1st iteration, (g) fluence calculated with diffusion approximation for the 4th iteration, (h) normalized optoacoustic image for the 4th iteration, (i) profiles for the uncorrected and corrected optoacoustic images along the same line as (c) for the 4th iteration, (j) fluence calculated with diffusion approximation for the 4th iteration with a different scattering coefficient, (k) normalized optoacoustic image for the 4th iteration with a different scattering coefficient, (l) profiles for the uncorrected and corrected optoacoustic images along the same line as (c) for the 4th iteration

4.4 Normalization by spectral means

In contrast to the previous methods to correct for the light attenuation when quantifying molecular probes, I present a ratiometric method for multi-spectral optoacoustic, which can compensate for the effects of light attenuation on the optoacoustic images without the use of analytical or numerical approximations for the light fluence. The proposed method assumes a reconstructed optoacoustic image $H(\lambda,r)$ that is proportional to the photon fluence U and the absorption coefficient $\mu_{a,}$ at each point (voxel) r in the illuminated object, which is described by equation (3.28). If U was spatially constant, i.e. $U(\lambda,r) = U(\lambda) = C$ then the subtraction image $\Delta H(r) = H(\lambda_1,r) - H(\lambda_2,r) = C\cdot[\mu_a(\lambda_1,r) - \mu_a(\lambda_2,r)]$ of two optoacoustic images acquired from the same volume but at different wavelengths would be proportional to the $\mu_{a,}$ difference at the two wavelengths. The assumption of constant fluence may hold for superficial imaging. For deep tissue imaging however the difference image $\Delta H(r)$ is instead written as

$$\begin{aligned}\Delta H(r) &= H(\lambda_1, r) - H(\lambda_2, r) \\ &\cong U(\lambda_1, r)[\mu_a(\lambda_1, r) - \mu_a(\lambda_2, r)]\end{aligned} \tag{4.6}$$

$\Delta H(r)$ in equation (4.6) depends not only on the absorption difference at the two wavelengths but also on the fluence term and is therefore biased toward the specimen's boundary, where the fluence is strongest. Equation (4.6) assumes that $U((\lambda_1,r)\approx U((\lambda_2,r)$, *i.e.* that the fluence attenuation with depth does not vary significantly with wavelength, which generally holds true for closely spaced wavelengths in the near-infrared spectrum.

To extract quantitative information on $\mu_{a,}$, $\Delta H(r)$ should be normalized by the fluence. Mathematical modeling of light fluence has been proposed for normalization[70, 71] but comes with significant limitations. First, light propagation does not solely depend on the absorption coefficient but is affected by scattering as well; the latter being a parameter that is not explicitly resolved on the optoacoustic images. Secondly the different system gains and losses, absolute tissue absorption values or the illumination distribution on the tissue

boundary, required for fluence computation inside tissues, are not in general accurately known. Collectively, these uncertainties reduce the accuracy of numerical computations and may even amplify the errors in the images [70].

Instead, the ratiometric method considered herein accounts for the fluence distribution in the optoacoustic images by dividing equation (4.6) by equation (3.28), in which case one obtains a ratiometric image

$$I \approx \frac{\mu_a(\lambda_1, r) - \mu_a(\lambda_2, r)}{\mu_a(\lambda_1, r)}, \tag{4.7}$$

which is independent of the spatially varying fluence. Equation (4.7) can be alternatively normalized by the sum of images at two different wavelengths. Image I is therefore an image of relative absorption change normalized for image absorption, the latter being an image that is generally proportional to blood volume. In that respect, I reflects chromophore retention normalized for blood volume, i.e. probe delivery. A different normalization scheme would instead divide with a slow absorbing component of image $H(\lambda_1,r)$, calculated either as a low-pass filtered image H or a decomposed image H to low frequency and high frequency varying spatial components as achieved by the sparse-decomposition method [89]. The use of ratiometric images has been invaluable in optical tomography of diffuse media [11].

To confirm the experimental findings, I examined the performance of equation (4.7) with simulated data, for the phantom depicted on Figure 34a. The bulk of the phantom was assigned an absorption coefficient of μ_a=0.4 cm^{-1} at wavelength λ_1 whereas the top and bottom insertions were only absorbing at wavelength λ_2 with an absorption coefficient of 0.45 cm^{-1}. The scattering coefficient was chosen to be constant and had the value of 10 cm^{-1}. Light distribution was simulated using a finite element solution of the diffusion equation and optoacoustic responses were derived using the forward part of IMMI. Figure 34b shows the simulated optoacoustic image for λ_1 and Figure 34c for λ_2. Figure 34d shows a difference image between the two wavelengths whereas Figure 34e shows an image produced with

equation (4.7). Although the two lesions reconstructed in this case are identical, the difference image erroneously shows the lesion close to the boundary appearing with 4x contrast compared to the deeper seated lesion (Figure 34d). In contrast the ratio image correctly reveals similar contrast between the two lesions (Figure 34e).

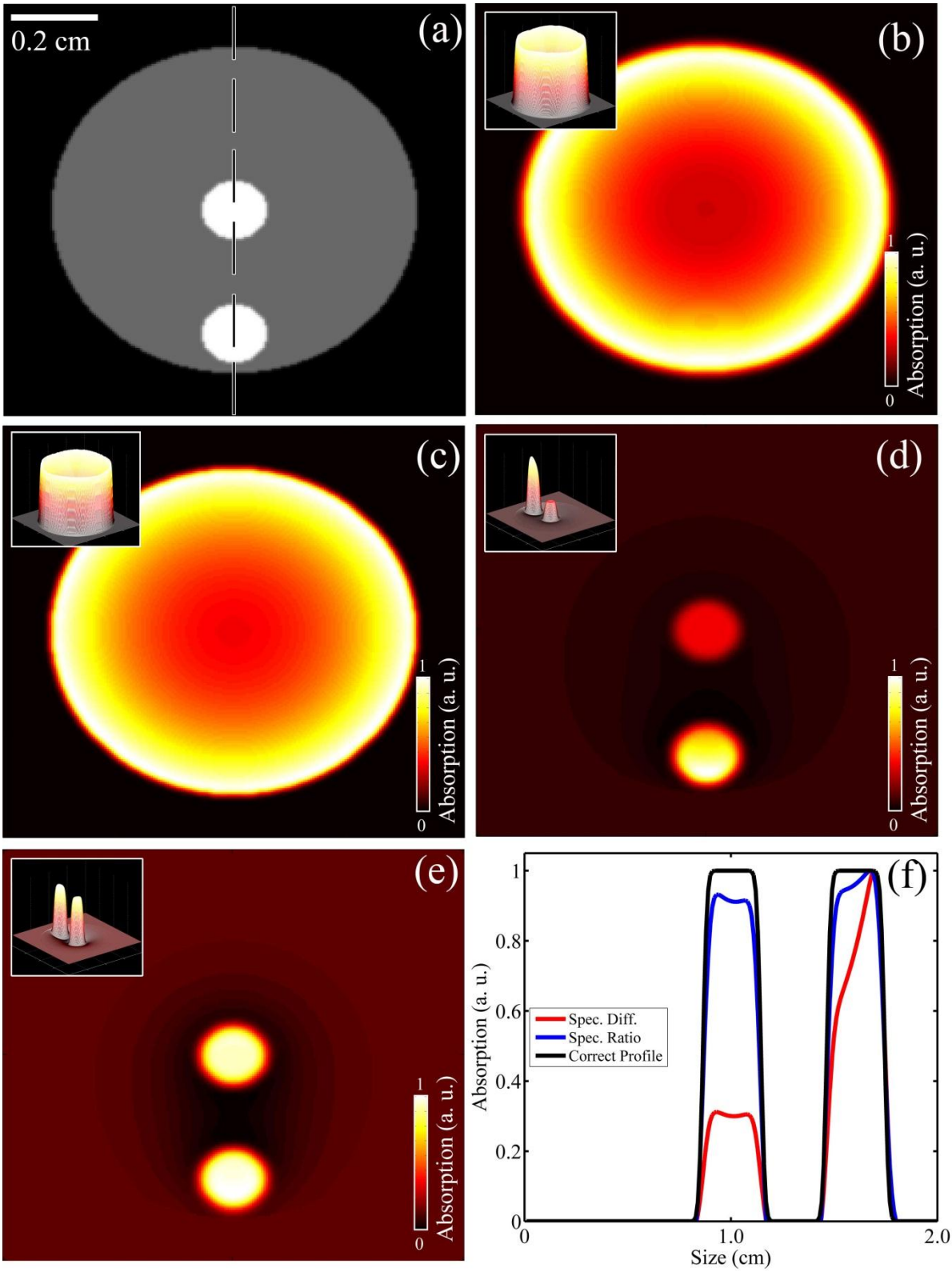

Figure 34: (a) sketch of the numerical phantom, (b) simulated optoacoustic image for λ_1, (c) simulated optoacoustic image for λ_2, (d) Spectral difference, (e) spectral ratio, (f) Reconstructed profiles along the dashed line on (a),

5. Experimental results

The previous two chapters show image reconstructions algorithms and image normalization schemes to correct for certain effects of inhomogeneous surface illumination and light attenuation within imaged targets. Before the performance of these algorithms is studied in experimental datasets, a brief description of the optoacoustic systems employed and of the general data processing steps are given. In the following subchapters the performance of the reconstruction algorithms is discussed with a focus on algorithm-related artifacts. Additionally the performance of the weighted IMMI algorithm is studied. It is capable for correcting for inhomogeneous surface illumination.

The other subchapters evaluate the performance of the image normalization methods. Here the same phantom and animal dataset were used to allow a better comparison between the proposed methods.

5.1 Experimental setups and data processing

To experimentally examine the performance of the proposed reconstruction algorithms and image normalization methods, two different systems were used. These optoacoustic tomographs were not developed by the author of this work. Nevertheless a brief overview over the systems is given in this chapter.

5.1.1 Apparatus I: MSOT I

The first experimental system used to experimentally evaluate the proposed algorithms is called MSOT I. The system was developed my Ma *et al.* and a detailed description of the system can be found in Ref. [55]. In brief, the system consisted of a tunable optical parametric oscillator (MOPO-700 series, Newport Corp., Mountain View, CA), pumped by a Q-switched Nd:YAG laser (Quanta-Ray Lab-Series 190-30 Newport) (Figure 35). The pump laser

operated on its third harmonic (35nm) to provide multispectral illumination between 400 nm and 680 nm. The laser provided a pulse duration of less than 10 ns and the repetition rate was 30 Hz. To provide a sufficient homogeneous illumination of imaged targets, a combination of iris, slits, cylindrical/spherical lenses and diffusers were used to manipulate the laser beam. To normalize for variations of the output power, a photo diode (PD) was installed for measuring the pulse energy. To record the acoustic signals, two different plumbum zirconate titanate (PZT) transducers were used. Both transducers were cylindrically focused to allow a two-dimensional image acquisition [55]. The first transducer used, had a central frequency of 3.5 MHz, 38.1 mm focal length while the detection element had a diameter of 13 mm (Model V382, Panametrics-NDT, Waltam, MA). The second transducer had a central frequency of 7.5 MHz, 25.4 mm focal length while the detection element had a diameter of 13 mm (Model V320, Panametrics-NDT, Waltam, MA). Together with the transducer a rotation stage was placed in the water tank. For experiments the imaged target was positioned on the stage and rotated to record the acoustic data for the chosen projection angles. For fast 360° data acquisition the system could operate in a continuous mode, whereas an averaged mode was also provided in cases were the SNR wasn‘t sufficient for single pulse measurements [55].

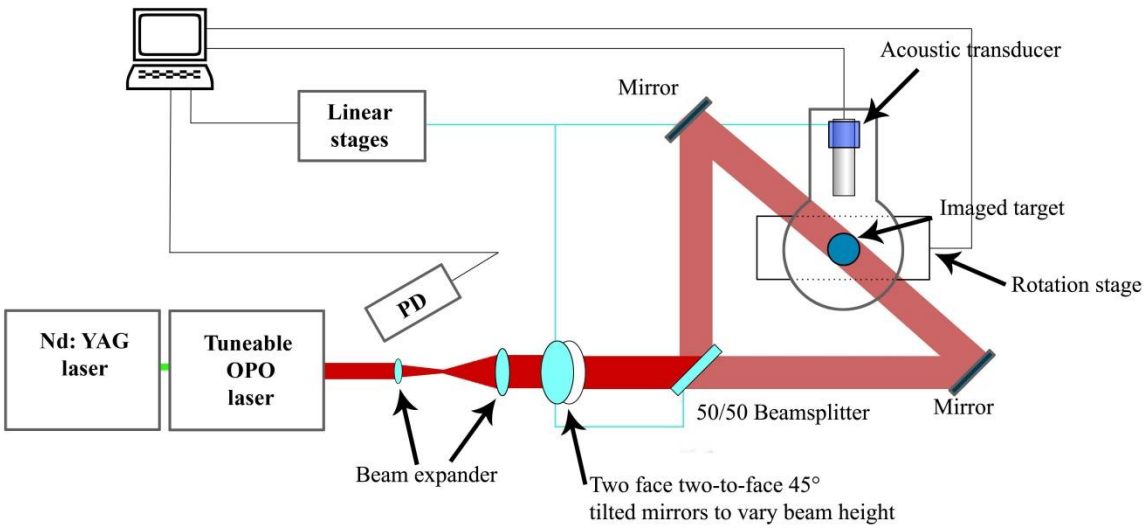

Figure 35: Sketch of the MSOT I system

5.1.2 Apparatus II: MSOT II

Aside from the good imaging performance, the MSOT I system was not capable of acquiring optoacoustic images in real-time. To fill this gap, Buehler *et al.* [36] developed an optoacoustic tomograph, which is capable of acquiring optoacoustic images fast enough to permit real-time video imaging[36]. The MSOT II system is also able to image a target three-dimensionally by moving the measured object along the z-axis and stacking the images to build a volumetric image stack. Instead of rotating an object to record tomographic datasets for several projects, a custom-made 64-element curved transducer array (Imasonic SaS,Voray, France) covering a solid angle of 172° around the object was built to allow the recording of 64 projections at the same moment (Figure 36a). Each single detection element is based on a piezocomposite material with a central frequency of 5MHz, bandwidth of more than 50% and a sensitivity of approximately 18 μV/Pa. The cylindrical focus is at 40 mm, providing an in-plane resolution of 150 μm and an elevational resolution of 800 μm. As a light source a tuneable optical parametric oscillator (OPO) laser (Phocus, Opotek Incorporated, Carlsbad, California) is used covering a spectrum from 680nm to 950nm. The pulse duration was below 10 ns at a repetition rate of 10 Hz. The laser beam is guided into a silica fused-end fiber bundle (Model PowerLightGuide, CeramOptec GmbH, Bonn, Germany) consisting of 630 fibers partitioned into 10 arms [36]. The ends of the fibers are positioned in a circular shape 3 cm away of the imaging target creating a ring-shaped illumination pattern of approximately 7 mm on the targets surface (Figure 36a). The beam power is kept below 20 mJ/cm^2 by broadening the beam shape. The employed linear stage (NRT150, Thorlabs GmbH, Karlsfeld, Germany) allows a linear translation in z-direction of the imaging target up to 150 mm with a minimal step size of 2 μm. Beyond the multispectral capabilities, the system provides good performance for video-rate optoacoustic tomography, shown in several animal studies. It is possible to image in real-time kidney perfusion [36] or real-time cardiovascular dynamics [37].

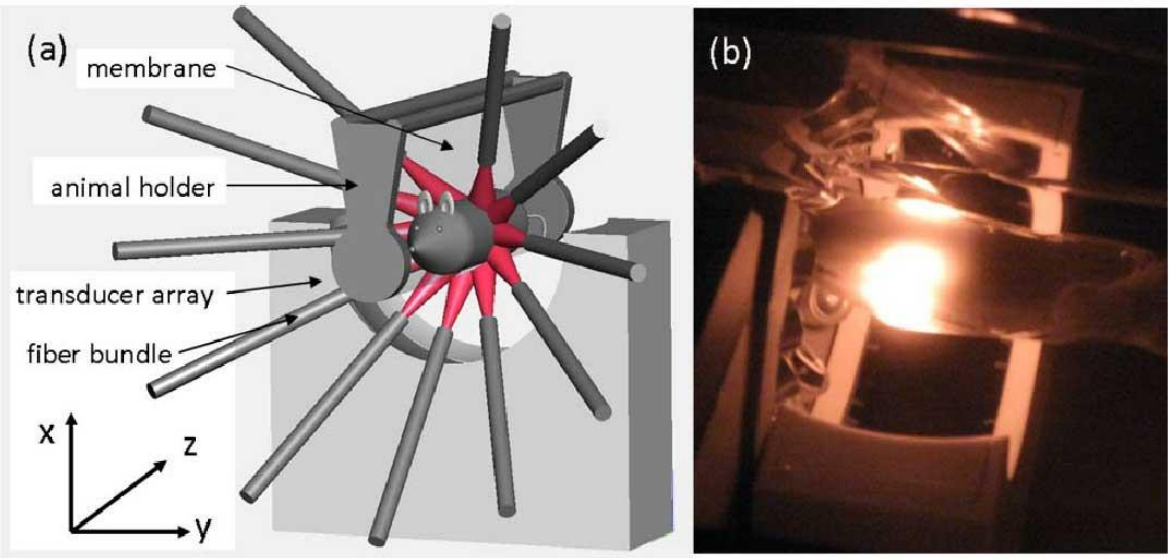

Figure 36: (a) Sketch of the MSOT II system (b) Picture of a mouse during a scan (Reprinted with permission from [76]. Copyright 2010, Optical Society of America).

5.1.3 Data processing

Before a detailed discussion of the performance of inversion and normalization schemes are given, the data processing steps are briefly described. As mentioned in previous chapters the useful frequency range of optoacoustic signals lies within a range from 50 kHz up to several MHz, depending on the size of the object and the transducer employed. According to the desired spectrum a band pass filter is used for the experimental data filtering acoustic signals from 50 kHz up to the central frequency of the employed transducer.

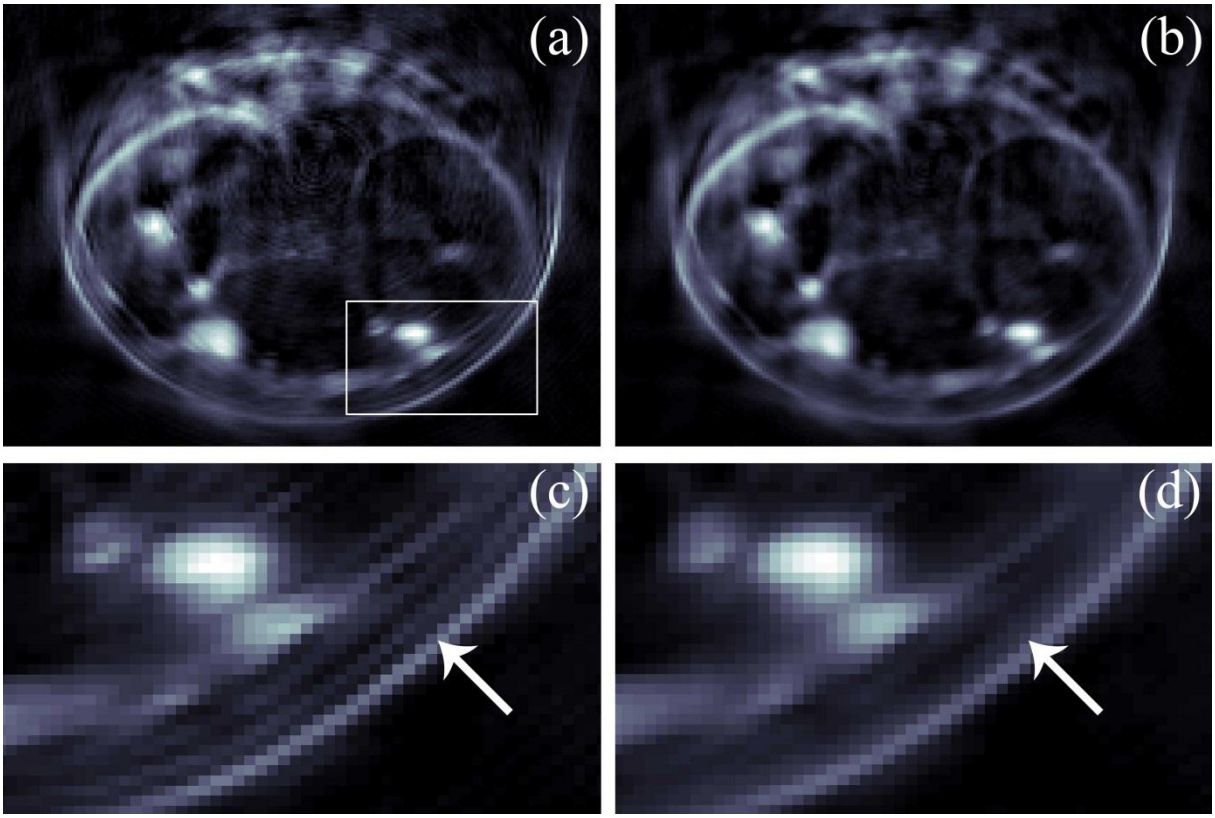

Figure 37: (a) Cross-sectional image of a human forefinger reconstructed by IMMI, no correction for the electrical impulse response (b) same dataset corrected for the electrical impulse response (c) zoom the marked area of (a) for the uncorrected image (d) zoom of the same area as (c) for the corrected image

In the next step the data is corrected for the electrical impulse response by deconvolving the measured data. By deconvolution, certain artifacts in the reconstructed images are removed and the quality of the reconstructed data is increased in terms of visual quality and in terms of quantifiability. To demonstrate the importance of this processing step, a human forefinger was measured in the MSOT II system. In the first experiment, the finger was measured in the transverse plane. Figure 37a shows the reconstructed image using IMMI without any correction for the electrical impulse response, whereas Figure 37b showcases the corrected image. A close inspection of the boundary of the uncorrected image reveals deficits in the form of a ~~"~~double boundary". This is shown in detail in Figure 37c and marked by an arrow, whereas Figure 37d does not depict that artifact. That effect of a double boundary is more dominant in images containing fine structures with a high contrast. Figure 38a shows an optoacoustic image in the coronal plane of the blood vessels of a human forefinger on its

upper side. The uncorrected image of Figure 38a shows the superficial structures of the blood vessels with limited clarity, whereas Figure 38b depicts a clearer image. On zooming in the marked area of Figure 38a, it shows a more detailed image of the structures revealing again ~~-d~~ouble borders" (Figure 38c). Figure 38d shows the same area as Figure 38c for the corrected image. The image shows more clearly the structures of the blood vessels because it does not suffer from impulse response-related artifacts.

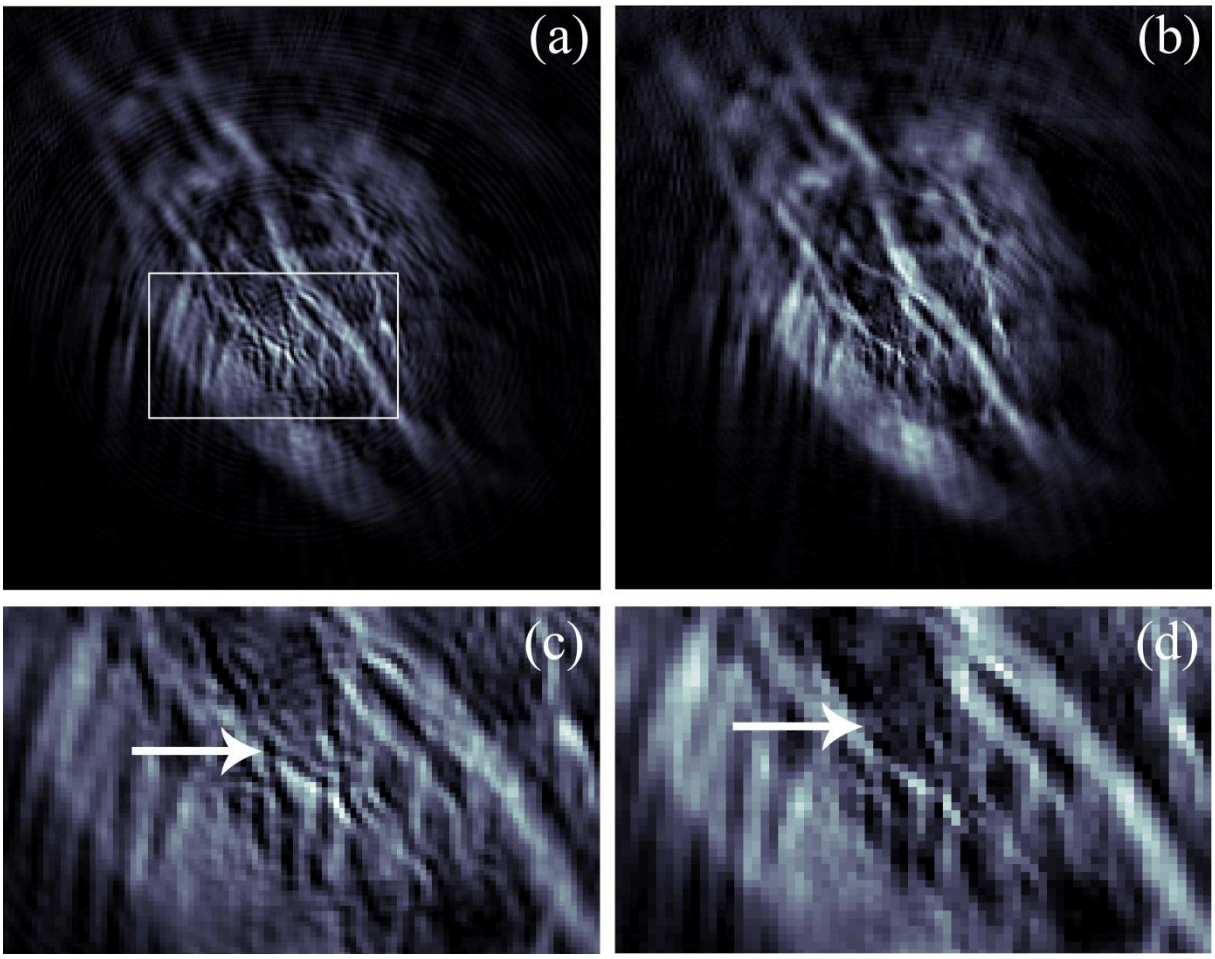

Figure 38: (a) image of a human forefinger reconstructed by IMMI of the coronal plane, no correction for the electrical impulse response (b) same dataset corrected for the electrical impulse response (c) zoom the marked area of (a) for the uncorrected image (d) zoom of the same area as (c) for the corrected image

5.2 Performance of the inversion schemes

This subchapter will study the performance of the presented inversion schemes for experimental data. It will be shown, that the back-projection algorithm is an artifact-rich inversion scheme also for experimental data. IMMI reconstructs images with better performance in terms of visual image quality and quantification. The performance of the modified IMMI algorithms is presented to demonstrate its flexibility to model certain experimentally related effects.

5.2.1 Performance of back-projection

The back-projection algorithm is a computationally very fast and resource light inversion scheme. The numerical implementation can easily be done in Matlab, Java or C/C++. Nevertheless the back-projection algorithm holds disadvantages generating various types of artifacts in reconstructed images. The typical artifacts found in back-projected images reduce not only the visual image quality, additionally they distort the quantification. The most prominent artifact manifests in the form of an accentuation of fast variations in the image (high gradient) which is accompanied by negative optical-absorption values that otherwise have no physical interpretation [31, 77].

To demonstrate these effects for practical cases, I built a tissue mimicking cylindrical phantom and measured it in the MSOT I system. To achieve ideal illumination conditions, the laser beam was expanded to about 2.5 cm and split into two beams, thus creating a nearly uniform light pattern around the object. A cylindrically focused transducer (Model V382, Panametrics-NDT, Waltam, MA), was used to record the optoacoustic signals emitted by the sample within the imaging plane. For collection of the signals over 360° projections, the samples were rotated on a stage while the transducer was placed at its focal distance of 38.1 mm from the center of rotation. The cylindrical tissue-mimicking phantom had a diameter of

1.8 cm with a background absorption and a scattering coefficient of μ_a= 0.2 cm^{-1} and μ_s‘ =10 cm^{-1}, respectively. Additionally the phantom had a rectangular insertion with an absorption coefficient μ_a= 2.1 cm^{-1} and had the same scattering as the background. The phantom was created by molding agar with appropriate concentrations of Intralipid and India ink (Higgins, Sanford Bellwood, IL) [90, 91].

In the reconstruction showed in Figure 39a, we can clearly see the phantom and a black ring with negative absorption in the area around the phantom (marked by the arrows). To show this in more detail the values along the dotted line were selected and printed as a graph in Figure 39b. An additional effect, which is not very obvious, is that the light attenuation is not reconstructed correctly. The profile shows a very strong light attenuation, which is not reasonable for the optical properties of the phantom. Rosenthal *et al*. discussed that in detail in [31], where they proposed the IMMI algorithm, which is able to overcome the limitation of back-projection based algorithms.

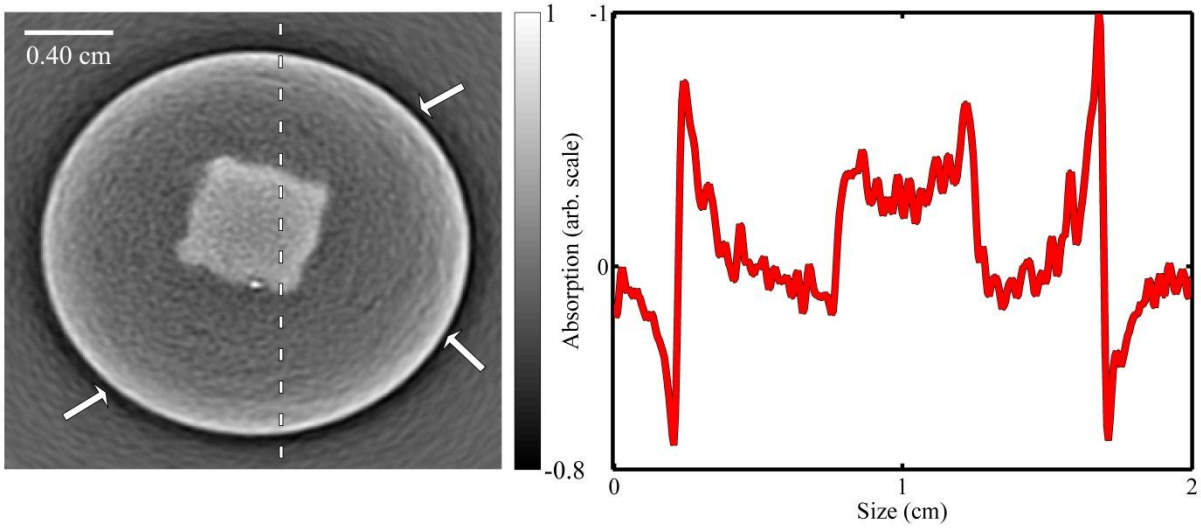

Figure 39: (a) optoacoustic image reconstructed by back-projection. (b) Graph along the dashed line of (a) to show the artifacts more in detail.

5.2.2 Performance of IMMI

To compare the performance with the classical back-projection algorithm the phantom of Figure 39a is first reconstructed using IMMI and LSQR (Figure 40a) and then a profile along the dashed line is shown (Figure 40b). A close look at the reconstructed image shows no real presence of negative value artifacts. There is only a small negative offset in the shown profile observable, which is caused by noise flawed impulse response measurements. Nevertheless the profile shows correct behavior for the light attenuation in accordance with its physical properties.

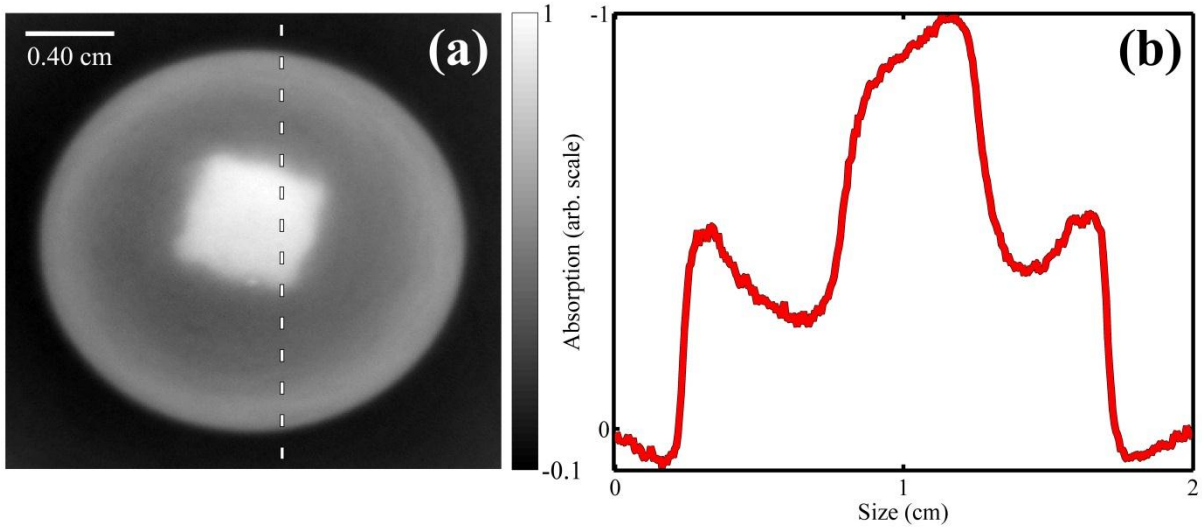

Figure 40: (a) IMMI reconstruction of Figure 39a (b) profile along the dashed line

As shown, model-based reconstruction schemes [31, 80] can eliminate negative absorption artifacts and improve the reconstruction accuracy over back-projection methods. Until now, I only showed phantom studies, which were based on phantoms with a very homogenous structure. Additionally the volumetric imaging capacity of the IMMI reconstruction method is examined [31, 55] by selecting the brain as a target organ in small animal imaging applications and studying the IMMI performance against back-projection methods. My underlying hypothesis was that the IMMI method would be necessary for improving imaging performance over artifacts commonly seen in back-projection algorithms.

The rationale for this study therefore was the necessity to select the most appropriate inversion method for accurate small animal optoacoustic brain imaging [75].

Again the experimental setup described in the previous chapter as MSOT I was used. In brief, the experimental setup consisted of a single acoustic detector (Figure 41a), whereas the imaged object was rotated in front of the transducer to obtain 360-degree tomographic scans of the generated optoacoustic response, as described in Ref. [55]. To evaluate the performance of the algorithm for small-animal imaging, a 6 day old mouse was measured *ex-vivo* with the experimental setup shown in Figure 41. The excitation wavelength employed was 650 nm, obtained from a nanosecond OPO (optical parametric oscillator) Spectra Physics laser. The optoacoustic signal detection was performed with a 7.5 Mhz cylindrically focused transducer (Model V320, Panametrics-NDT, Waltam, MA), scanning to receive signals over 360 degree projections around the animals head, at 3 degree steps. In order to improve the signal-to-noise ratio of the signals, each projection was obtained by averaging 32 independent measurements, resulting in 32 x 120 = 3840 measurements which were acquired in approximately 10 minutes. The model matrix, which was subsequently inverted, consisted of 90000x381900 elements corresponding to a reconstructed image of 300 by 300 pixels, of approximately 64 micron resolution. Image validation was based on a cryo-slicing system [92] that can allow high-resolution photography of mouse slices obtained ex-vivo from frozen mice with a similar position to the non-invasive optoacoustic imaging studies.

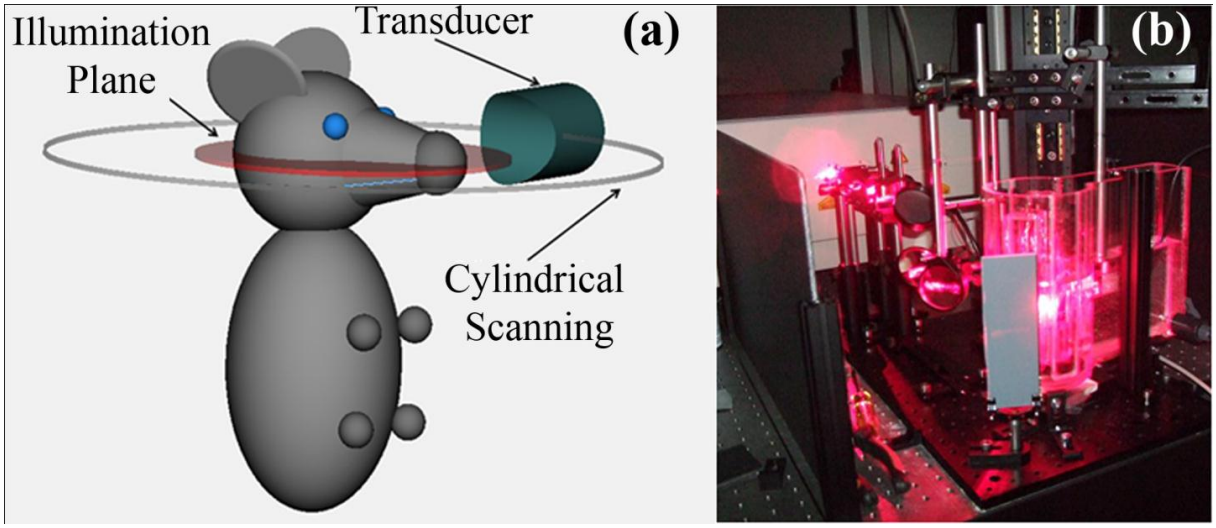

Figure 41: (a) Schematic representation of the OAT system (b) Picture of the system during the measurement (Reprinted with permission from [75]. Copyright 2011, American Institute of Physics)

Figure 42 depicts cross-sectional slices of the mouse head and corresponding cryo slices to verify the reconstruction results. The first row (Figure 42a and Figure 42b) presents images reconstructed using the back-projection image algorithm. The second row (Figure 42c/d) shows images reconstructed using IMMI. To demonstrate that IMMI could also reconstruct the high frequency component of the optoacoustic signals, a high-pass filter was applied to the images in Figure 42c and Figure 42d. The result, shown in Figure 42e and Figure 42f, is comparable to the back-projection images shown in Figure 42a,b. To validate the findings, frozen mice were sliced at a slice thickness of 400 microns and the slices were photographed. Photographs of sliced tissue corresponding to the acquired optoacoustic images are shown in Figure 42g and Figure 42h. The anatomical structures seen are marked with numbers and described in the figure caption in detail [75].

Despite the approximate co-registration between cryosliced photographs and non-invasive opto-acoustic images, Figure 42 shows a good correspondence between the anatomical features seen on the photographs and the reconstructions using back-projection and IMMI. There are however noticeable differences between the appearances of images obtained using the two reconstruction methods. The boundary of the imaged mouse is better defined in the

IMMI reconstructions compared to the back-projection reconstructions. The back-projection images also exhibit more artifacts, identified as dark arcs in the images. In contrast, these artifacts do not appear in the IMMI images. In the high-pass filtered IMMI images, similar artifacts may be observed. These results demonstrate that the conventional back-projection algorithm does not treat properly low-frequency components in the optoacoustic images. In contrast IMMI images retain high frequency features whereas they also treat the low frequency components yielding overall images that contain more complete information. Figure 42c depicts at label 1 and 3 the eye sockets of the mouse head. The eye socket in the lower part (label 3) of the back-projected image is difficult to identify as it appears not closed and smeared. In the IMMI reconstructions the same structure more closely resembles the expected round structure of the eye socket and the smearing artifact is removed. One of the most problematic artifacts of the traditional back-projection algorithm is the appearance of negative absorption values that have no physical meaning and further complicate the understanding of the different structures appearing. The appearance of these troughs is shown with arrows on Figure 42b. In contrast, IMMI always presents images with physically correct positive contrast which simplifies image understanding. It can allow the straightforward application of image processing tools such as filtering or segmentations, which correspond to real physical attributes [75].

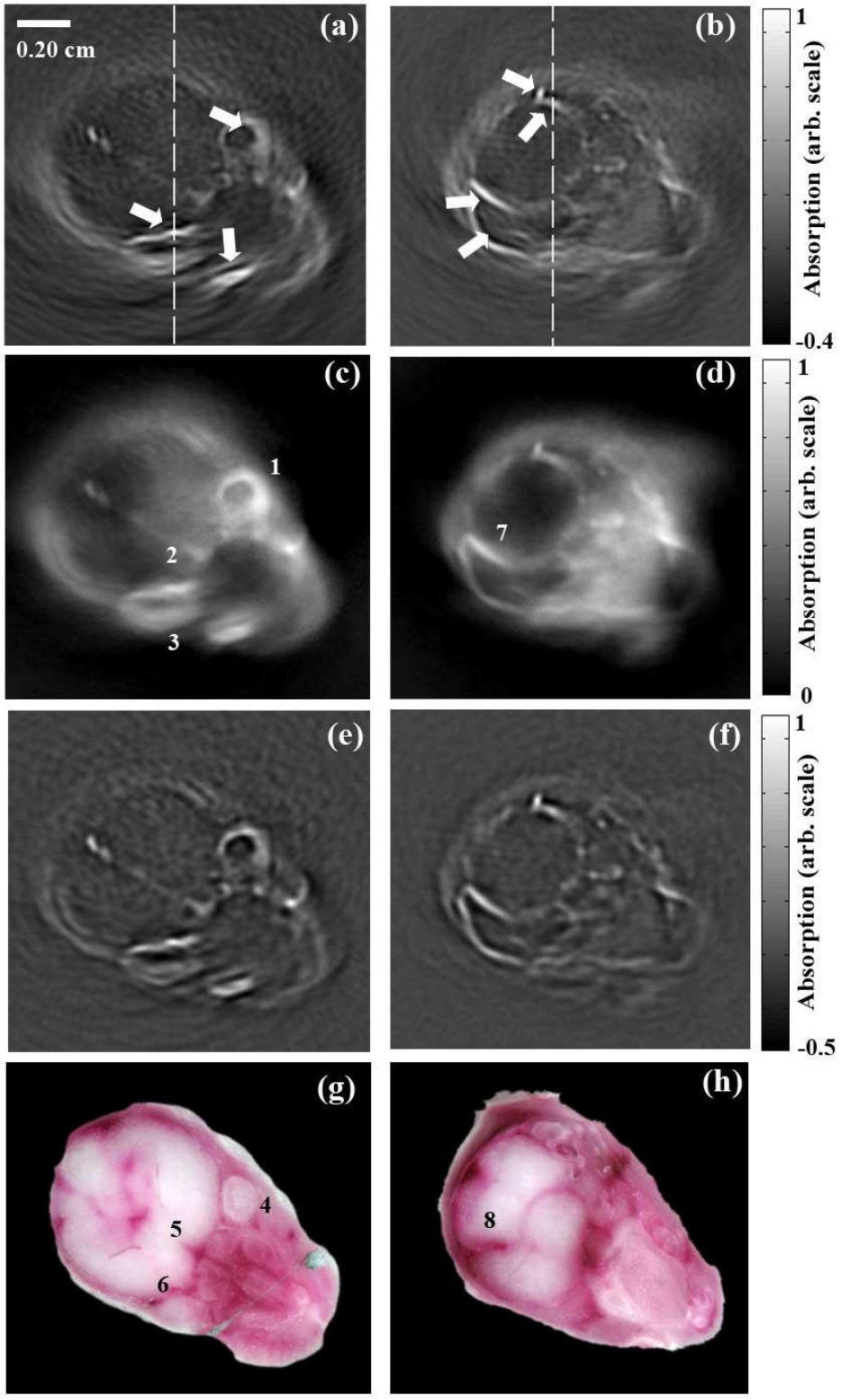

Figure 42: Several cross-sectional slices of the head region of a mouse back projection based reconstructions of (a) head region, (b) lower part of the head, (c) and (d) corresponding IMMI reconstructions, (e) and (f) corresponding IMMI high pass filtered images, (g) and (h) cryoslices (Reprinted with permission from [75]. Copyright 2011, American Institute of Physics)

Anatomical structure:
1, 3, 4, 6 – eye sockets
2, 5,7,8 – blood vessels

Figure 43 demonstrates the negative absorption artifact in more detail. The first row in Figure 43 represents profiles taken from the corresponding images in the first row of Figure 42 along the dotted line shown on Figure 42a and b. The second row shows corresponding profiles for the IMMI reconstructed images of Figure 42 c, d. The profiles from the back-projection reconstructions show clear negative absorption artifacts around areas with a high gradient, i.e. a fast change in light absorption, seen in the 2D images. We can find such artifacts in multiple pixels of the images in Figure 42 a, b. In addition, the overall image background appears to be around zero, erroneously indicating non-absorbing regions throughout the mouse head. In contrast, the IMMI images show positive profiles which are more justifiable from a physical standpoint. This appearance is closer to equivalent profiles obtained from the photographs of Figure 42g, h, which are shown on Figure 43e, f. The appearance of the profiles between Figure 43 c, d and e, f is only approximate since the cryoslices shown only approximately match the virtual slices imaged by the non-invasive opto-acoustic method. In addition the color images also comprise scattering contrast, which is not visualized in the optoacoustic images [75].

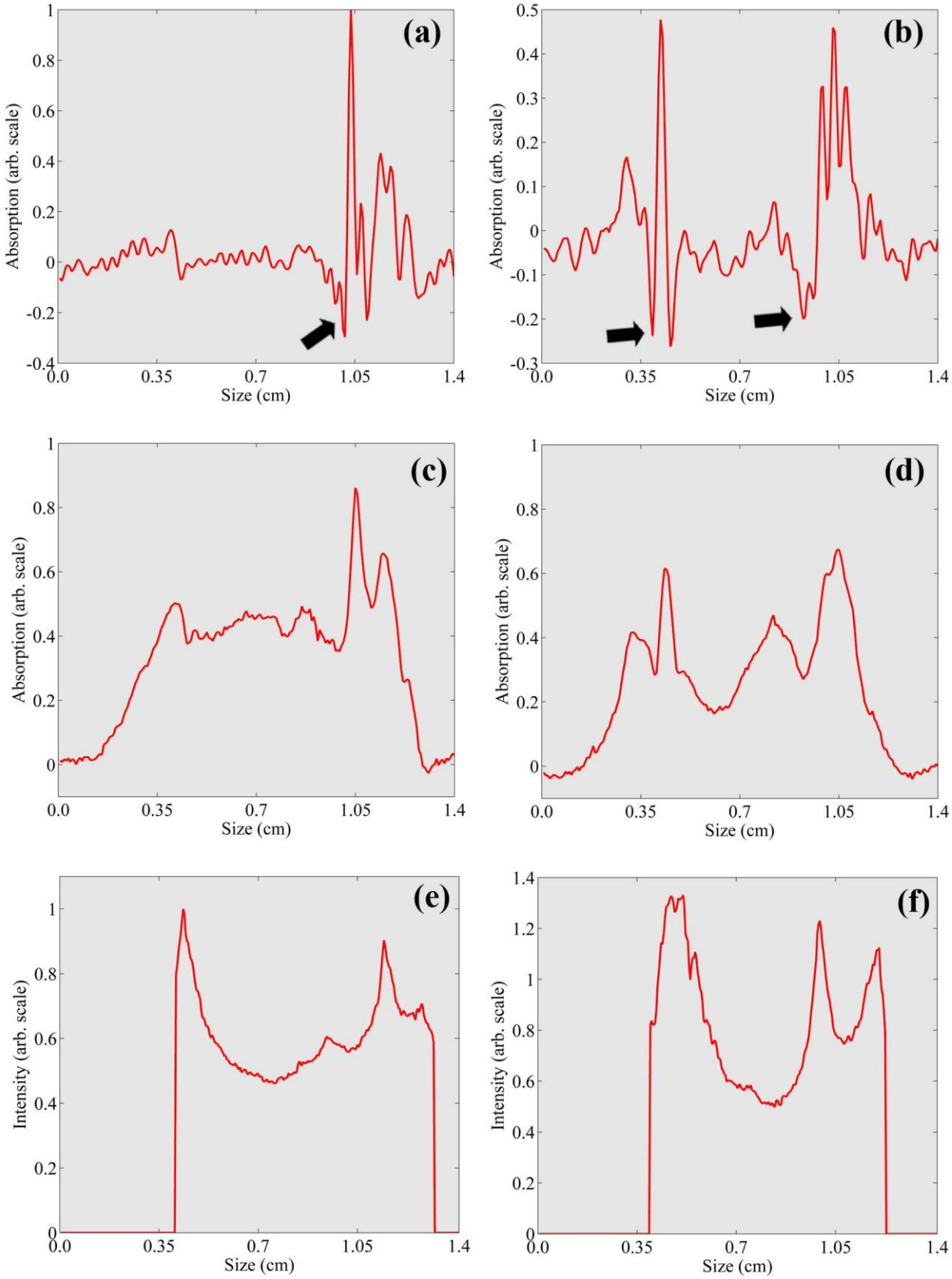

Figure 43: cross-sectional profiles (a) and (b) for standard back projected reconstruction of Figure 42a/b (c) and (d) IMMI profiles of Figure 42c/d (e) and (f) profiles of the photos of Figure 42g/h (Reprinted with permission from [75]. Copyright 2011, American Institute of Physics)

By accurately treating the low frequency components of the signal, IMMI yields images that have better physical value compared to images reconstructed by the back-projection method. Consequently the algorithm manages to avoid the generation of artifacts common in back-projection methods, such as distorted reconstructions of boundaries and round structures and negative absorption signals. Therefore, quantification of regions of interest, multi-spectral operations and other image processing tasks can be applied with better accuracy. Based on the results demonstrated herein, in can be concluded that IMMI may be considered as a promising alternative to back-projection algorithms in small animal brain optoacoustic imaging studies. While the IMMI images appear of lower resolution compared to conventional back-projection parameters, this is only a perception result attributed mainly to the retention of low frequency components in the image. High pass filtering of the images reveal the same resolution common in the images generated by back-projection showing that all the high frequency information is retained. The results were intentionally obtained from a challenging tissue structure such as the mouse head in order to have a variance of contrast mechanism from the generally homogeneous appearance of the brain itself, with optically varying bone structures, relative scattering clear media such as the eyes and air-cavities associated with the mouth structure. The findings and conclusions were corroborated by anatomically accurate cryoslice images which reveal the exact anatomical appearance of the tissue imaged and allow for a gold-standard in the performance comparison investigated herein [75].

5.2.3 Performance of weighted IMMI

To verify the performance of the weighted IMMI scheme, first I tested it on tissue mimicking phantoms. The measurements were performed in a tomographic continuous acquisition scanner presented here under the name MSOT I[83]. Briefly, a tunable optical parametric oscillator laser (MOPO-710, Spectra-Physics, Mountain View, CA, USA), providing < 10 ns duration pulses with 15 Hz repetition frequency in the visible spectrum (450–680 nm), was used in order to illuminate the sample under investigation. In all experiments, a wavelength of 650 nm was used which yielded an average power of approximately 450 mW. In ideal illumination conditions, the laser beam was expanded to about 2 cm and split into two beams, thus creating a nearly uniform light pattern around the object. Subsequently, the beam size was reduced with focusing lenses to 0.8 cm in order to simulate the partial illumination scenario (Figure 28a). A cylindrically focused transducer (Model V382, Panametrics-NDT, Waltam, MA), was used to record the optoacoustic signals emitted by the sample within the imaging plane. For collection of the signals over 360° projections, the samples were rotated on a stage while the transducer was placed at its focal distance of 38.1 mm from the center of rotation[76].

To showcase reconstruction improvements attained by the weighted model-based inversion, two phantoms were constructed. Both phantoms were cylindrically shaped and had a diameter of 16 mm, background absorption coefficient of $\mu a = 0.2\ cm^{-1}$ and reduced scattering coefficient of $\mu s' = 10 cm^{-1}$. The first phantom was used as an imaging target (Figure 44a) while the second phantom (Figure 44c) served for calibration of light deposition pattern on the surface of the imaged objects. For this purpose, a thin carbon stick was embedded at the phantom‘s surface. By rotating the phantom, magnitudes of optoacoustic responses from the stick were recorded over 360°, as shown in Figure 44b [76].

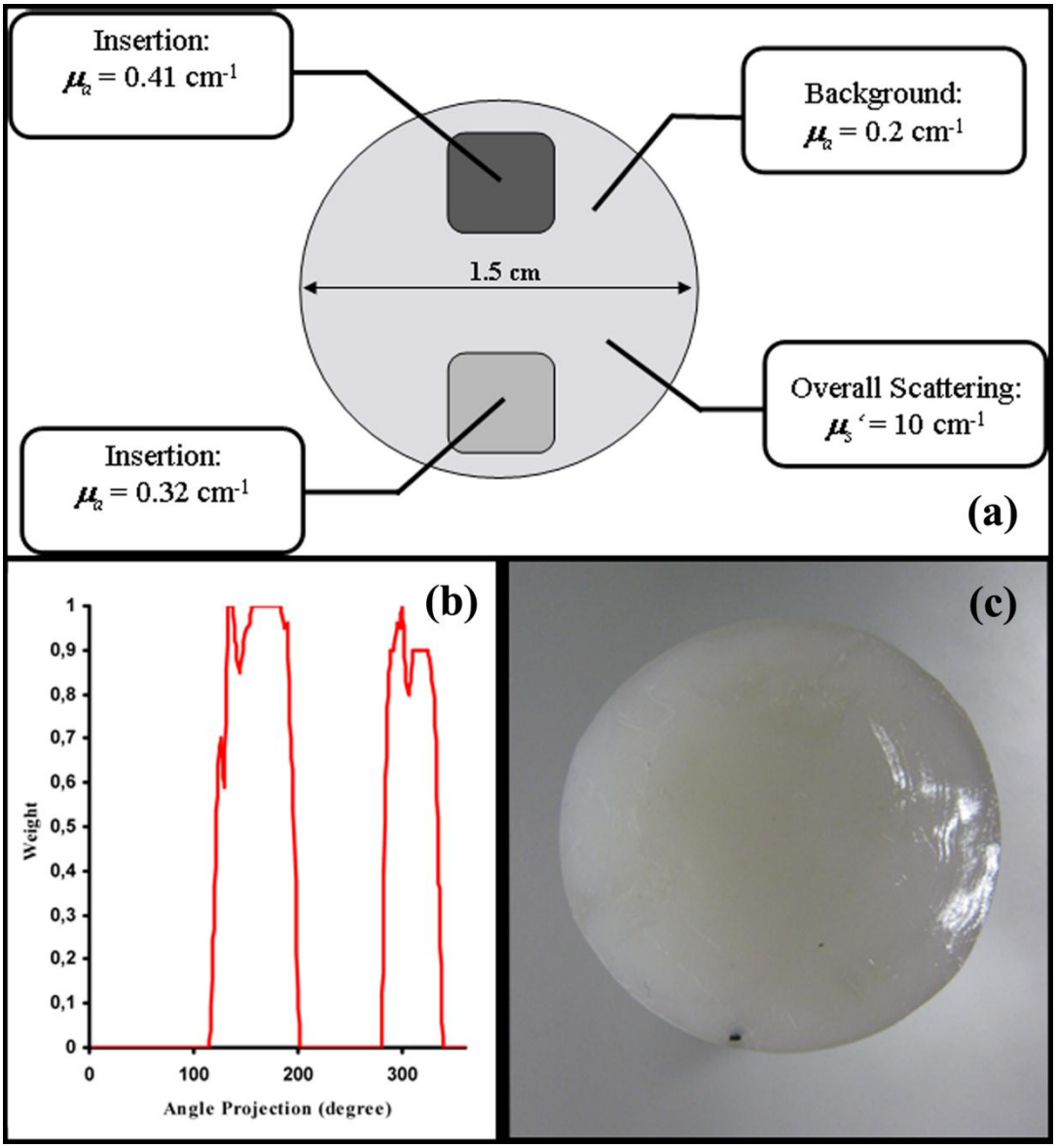

Figure 44: Experimental validation results. (a) Sketch of the imaged phantom; b) The measured illumination pattern upon the object's surface; c) Sketch of the illumination calibration phantom (Reprinted with permission from [76]. Copyright 2010, Optical Society of America)

The tomographic optoacoustic data were collected over 360 degrees with increments of 3 degrees. All the reconstructions were performed using a 100×100 grid, which corresponded to a pixel size of approximately 160 μm. The images of the phantom were first reconstructed for the full illumination case with laser beams covering the entire width of the phantom, as shown in Figure 45a. The average values of the experimentally reconstructed absorption coefficient in the two insertions were 0.32 cm^{-1} and 0.41 cm^{-1}. Subsequently, the beam size was reduced to approximately 0.8 cm and the image was reconstructed by the standard model-based

inversion assuming uniform illumination (Figure 45b). As expected, due to incorrect illumination assumptions and similarly to the numeric simulations, one can observe surface blurring effects while the other structures in the phantom‘s center are barely visible. To correct for these artifacts, we have used the illumination maps previously obtained with the calibration phantom. Equations (4.3)-(4.4) were utilized in order to build a weighted matrix for each projection which was subsequently applied to obtain the weighted forward model. The run time for constructing and inverting the model matrix was approximately 30 minutes for the given experimental setup. It was a sparse representation of the matrices used and the inversion was solved by using LSQR. The sparse matrix occupied approximately 1.5 GB of memory. The results of the weighted reconstruction are presented in Figure 45c and clearly show that the method was able to correct for image artifacts introduced by the sub-optimal partial illumination. The average values of the reconstructed absorption coefficient in the two insertions were in this case 0.326 cm^{-1} and 0.42 cm^{-1} [76].

To demonstrate the stability of the algorithm, the weights were built using different estimations of background absorption. As shown in Figure 45d, the algorithm is stable for variations of +/- 0.1 cm^{-1} between the real background absorption and the one assumed in the model[76].

Apparently, the uniform illumination experiment attained a slightly better quantification as compared to the weighted model-based correction algorithm. The relatively small discrepancies can be attributed to inaccuracies in characterization of the beam and building the model. Clearly, the diffusion equation can only serve as an approximation to the realistic fluence distribution while possible inaccuracies in the positioning of the calibration phantom relatively to the reconstructed phantom could introduce additional errors. Nevertheless, the algorithm was shown to significantly improve overall image quality and quantification compared to the uncorrected image[76].

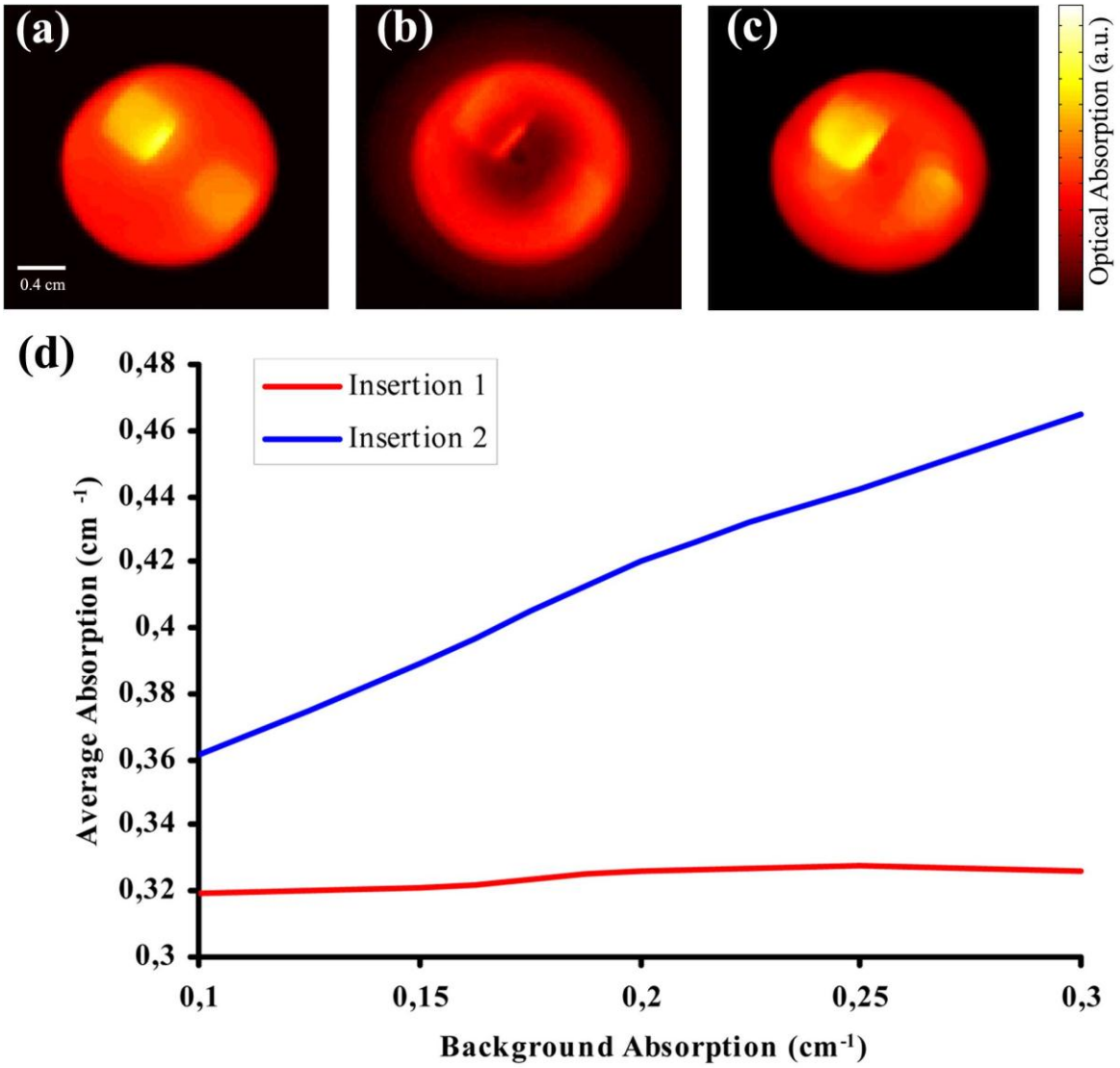

Figure 45: Model-based reconstruction for the a) Fully illuminated phantom; b) Variable partial illumination; c) Including weighting correction; d) Recovered absorption coefficient for weighted reconstruction with various assumptions for the background absorption (Reprinted with permission from [76]. Copyright 2010, Optical Society of America).

To further showcase the performance of the weighted IMMI method I applied it on real mouse data acquired with the recently reported whole body real-time scanner, which is described as MSOT II in this thesis [36]. In this imaging configuration the illumination remains constant for all the projections; however, the multiple detectors around the object only provide a partial view of the imaged object, resembling the case shown in Figure 28b. The measurement was performed on an anesthetized mouse, which was positioned in a supine position in the animal holder [36]. The imaging wavelength was 850 nm and the laser fluence

upon the animal surface was kept below 20 mJ/cm^2. Optoacoustic signals were measured with a cylindrically focused 64 element transducer array covering a 172° arc around the mouse (Figure 46a). The sensitivity field, as shown for one of the detection elements in Figure 46a, was determined beforehand by scanning the imaging plane in 1 mm steps with an illuminated graphite pencil tip (~0.5 mm) glued onto an optical fiber and measuring the magnitude of the corresponding optoacoustic signal. The reconstructions were performed on a 200×200 grid yielding a voxel size of approximately 150 μm. To stabilize the reconstruction and reduce noise, the 64 measured signals were interpolated to a set of 400. The weighted matrix taking into account the sensitivity fields of all the elements was constructed using equation (3.27). The inversion of the forward model was done with the LSQR algorithm. Figure 46b and Figure 46c show IMMI reconstructions with and without the correction for the sensitivity fields, respectively. Several image artifacts have been reduced by using sensitivity correction, including signal smearing in the spleen, some erroneous negative reconstruction values and grainy appearance, as correspondingly marked with numbers 1-3 in Figure 46b and Figure 46c [76].

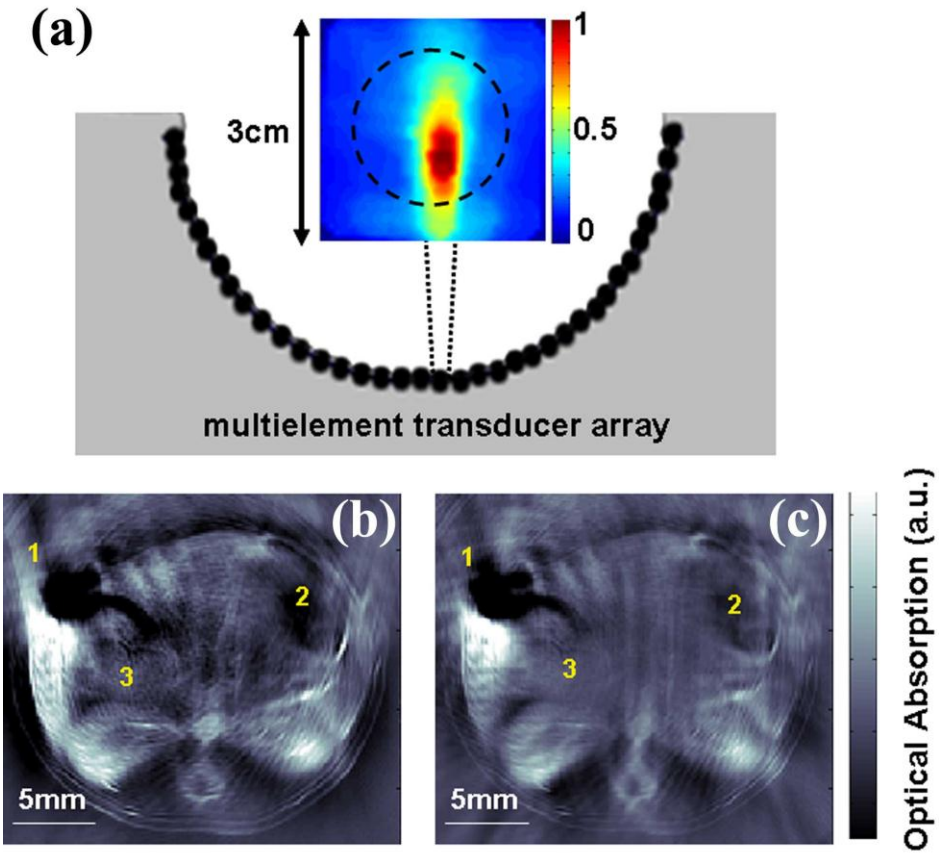

Figure 46: (a) Example of the measured limited-angle sensitivity field of a single element inside a multi-element transducer array. The approximate position of the imaged mouse is indicated by the dashed circle. The object was uniformly illuminated in the imaged plane; (b) model-based reconstruction of the mouse lower abdomen without ultrasound sensitivity field correction and (c) with sensitivity field correction. The latter are observed to reduce arc artifacts (1), eliminate some of the negative values (2) and smooth grainy appearance of the image (3) (Reprinted with permission from [76]. Copyright 2010, Optical Society of America).

The advanced semi-analytical model-based inversion scheme was successfully tested and compared to the commonly used back-projection and the unweighted model-based reconstruction on both numerical and experimental data. For the simulated data, the weighted model-based reconstruction and original image were almost identical. In contrast, similar correction using back-projection reconstruction is so far not possible. Thus, quantification remains challenging due to intrinsic inaccuracies of the method in the form of negative values and erroneous accentuation of fast absorption variations in the image. For the numerical phantoms, the weighted model-based inversion was able to correct the blurring and smearing effects so that the shape and absorption values in the inclusions were nearly the same compared to the homogeneously illuminated phantoms. The corrected images in the

experimental case showed deviations below 10% from the real absorption values in the phantom. It was further possible to show that the method is suitable for taking into account the limited-angle detection fields of common ultrasonic detectors, which was demonstrated on real in vivo mouse data [76].

The results attained by the proposed reconstruction method emphasize the advantages of the semi-analytical model-based inversion scheme over other commonly-used reconstruction methods for OAT. The methodology provides therefore a more generalized tomographic framework and serves as a robust method for quantitative optoacoustic image reconstruction [76].

5.3 Experimental results for normalization methods

This chapter showcases the performance of the presented normalization schemes for two experimental datasets, which I built and measured for this study. The first dataset consists of a tissue mimicking phantom with two insertions. To further depict the efficiency of the ratiometric normalization scheme, the insertions were spectrally dependent. The cylindrically shaped phantom had a diameter of 1.5 cm and was made of agar. India ink and intralipid were used to provide a background absorption of μ_a = 0.4 cm^{-1} and background scattering of μ_s‘ =10 cm^{-1}. Additionally the phantom contained two round inclusions with reduced scattering coefficient of μ_s‘ = 10 cm^{-1}. The lesion close to the boundary had an absorption coefficient of μ_a = 2.2 cm^{-1} at λ_1 = 580 nm and μ_a = 2.4 cm^{-1} at λ_2 = 560 nm whereas the lesion at the center attained μ_a = 2.2 cm^{-1} and 2.6 at λ_1 = 580 nm, 560 nm respectively. In an optimal normalized image the lesion at the center should have a higher absorption compared to the lesion close to the boundary. For better understanding a sketch of the phantom is shown in Figure 47a/b. Such complex scenarios often occur in experiments, where one blood vessel is labeled with a molecular probe and other blood vessels are unlabeled. The target could be for example plaque, which has accumulated only in certain vessels.

Imaging was performed at 560 nm and 580 nm using a tunable optical parametric oscillator laser (MOPO-710, Spectra-Physics, Mountain View, CA, USA), by rotating the phantom in front of a cylindrically focused ultrasound transducer (V382, Panametrics-NDT, Waltam, MA), as described in chapter 5.1.1. For the numerical and analytical methods only the dataset measured at 560 nm was used.

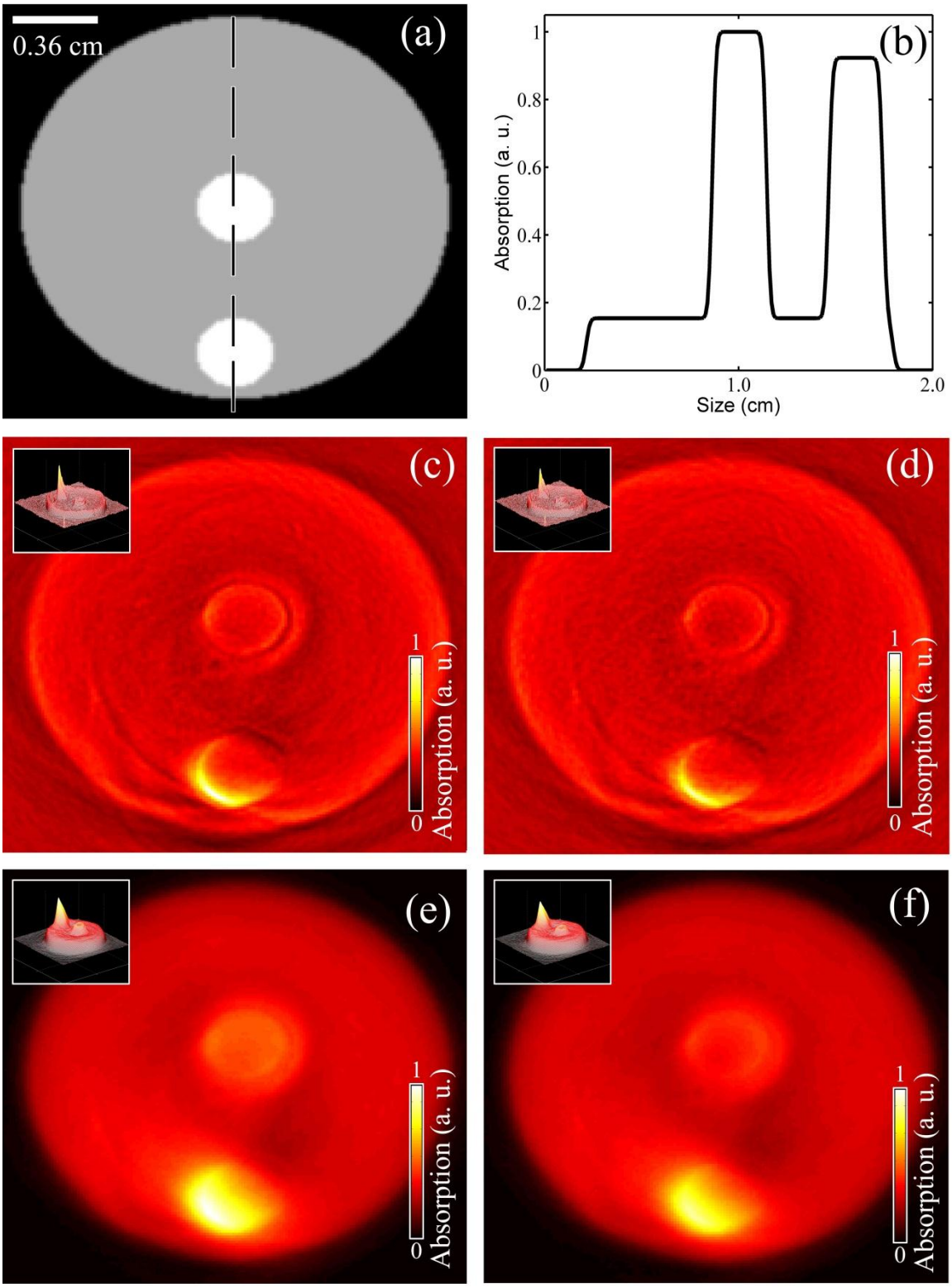

Figure 47: (a) Phantom sketch (b) Profile along the dashed line of (a) to show the optical absorption in a normalized scale (c) back-projection based reconstruction of the phantom measured at wavelength λ_2 (d) back-projection based reconstruction of the phantom measured at wavelength λ_1 (e) IMMI based reconstruction of the phantom measured at wavelength λ_2 (f) IMMI based reconstruction of the phantom measured at wavelength λ_1

For the second dataset I measured a mouse *post mortem*, where three tubes were implanted. The tubes were filled with Indocyanine Green (ICG) providing an absorption coefficient of $\mu_a = 1.6\ cm^{-1}$ at $\lambda_1 = 800$ nm and were not absorbing at $\lambda_2 = 880$ nm. A sketch of the mouse with the location of the tubes is given by Figure 48c. Imaging was performed in the abdominal area using a 64-element ultrasound array and ring illumination system as described in chapter 5.1.2, at 800 nm and 880 nm. Figure 48a/b depicts the optoacoustic images obtained at the two wavelengths, showing several anatomical structures, notably liver blood vessels. However the ICG tubes are not visible, due to the strong surrounding contrast. To test the performance of the analytical and numerical methods both images are corrected for the light attenuation. Due to the low absorption of the ICG compared to the intrinsic contrast of the tissue, the difference is taken in a second step to identify the molecular probes. For multispectral optoacoustic tomography this is a common approach to detect molecular probes. By taking the difference of two images the intrinsic contrast of the hemoglobin is reduced and ideally only the molecular probe remains.

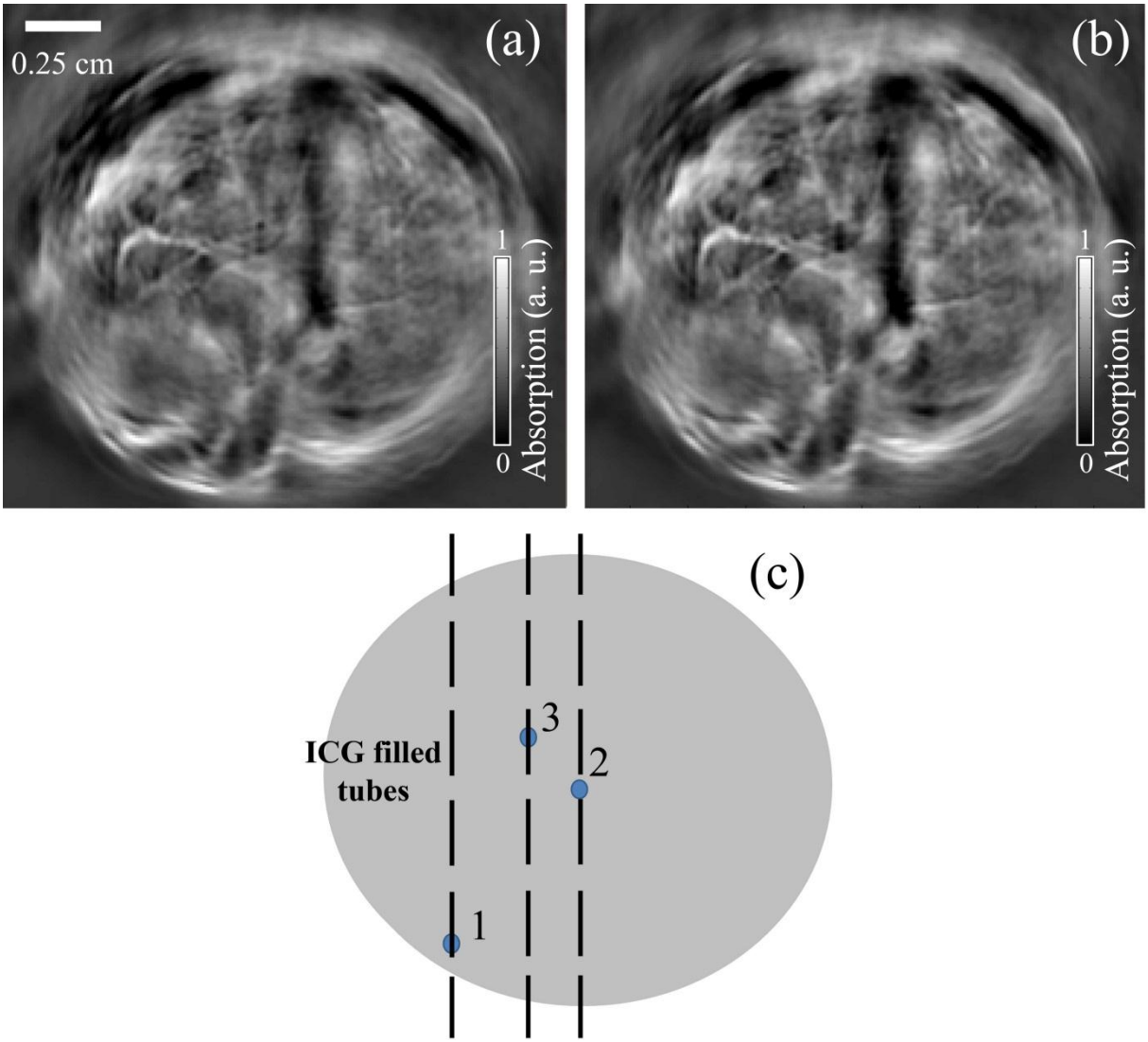

Figure 48: (a) tomographic optoacoustic image of t he abdomen of a mouse at a wavelength of 800 nm with implanted ICG filled tubes (b) imaging of the same region as (a) at 880 nm (c) sketch of the position, where the ICG filled tubes were implanted

Phantom images were reconstructed using the recently introduced interpolated model-matrix inversion (IMMI) algorithm [31] (Figure 48e/f) and the back-projection algorithm(Figure 48c/d). Despite the fact that IMMI yields in general a better performance in terms of contrast and quantification, back-projection is widely used. For comparison reasons, back-projection will be presented for the phantom experiments. To avoid negative absorption artifacts in the region of interest (ROI) for iterative image normalization and the ratiometric algorithm, an offset of 0.2 was added. For the animal experiment only IMMI is considered because of its superior image quality.

5.3.1 Bessel function based

To study the performance of the analytical two dimensional Bessel function based approach for experimental data, the dataset for the tissue mimicking phantom is selected and reconstructed by IMMI and by back-projection. First I normalized the reconstructed image based on back-projection by equation (4.1) using equation (4.2) to approximate the light fluence U for normalization (Figure 49a). A radius $r = 0.75$ cm was chosen and a coefficient k of 200 was selected. The selection of coefficient k is a physical approximation for practical cases. Typically the normalized image is checked after an initial normalization by the user and the parameter k is optimized until a reasonable normalization is achieved.

The normalization of the raw optoacoustic image (Figure 47c) is shown in Figure 49c. Both lesions seem to have the same signal strength. A plot along the dashed line reveals that the central lesion is still weaker as compared to the lesion close to the boundary (Figure 49e). Comparing this with the real absorbing properties demonstrate the limited usability of the method. The coefficient can be changed until a nearly perfectly normalized image is generated. This can again only be obtained by using the *a-priori* knowledge of the phantom composition.

The normalization of the optoacoustic image reconstructed by IMMI, shows approximately the same performance (Figure 49d/Figure 49f). Nevertheless the IMMI reconstructed images show in general a better performance at least in terms of visual image quality. Due to the normalization procedure, artifacts generated by the back-projection algorithm could be amplified and additionally decrease the visual performance of the reconstructed image.

The showcased scenario is difficult, but common in the field of biomedical research. A pure analytical model of the light fluence is too erroneous to solve such a sensitive problem. Nevertheless an image normalization based on a two dimensional Bessel function still can be

used in less sensitive situations. It can help to increase the visual image quality of anatomical images. An additional advantage is the easy implementation and fast computation time of less than 1 s.

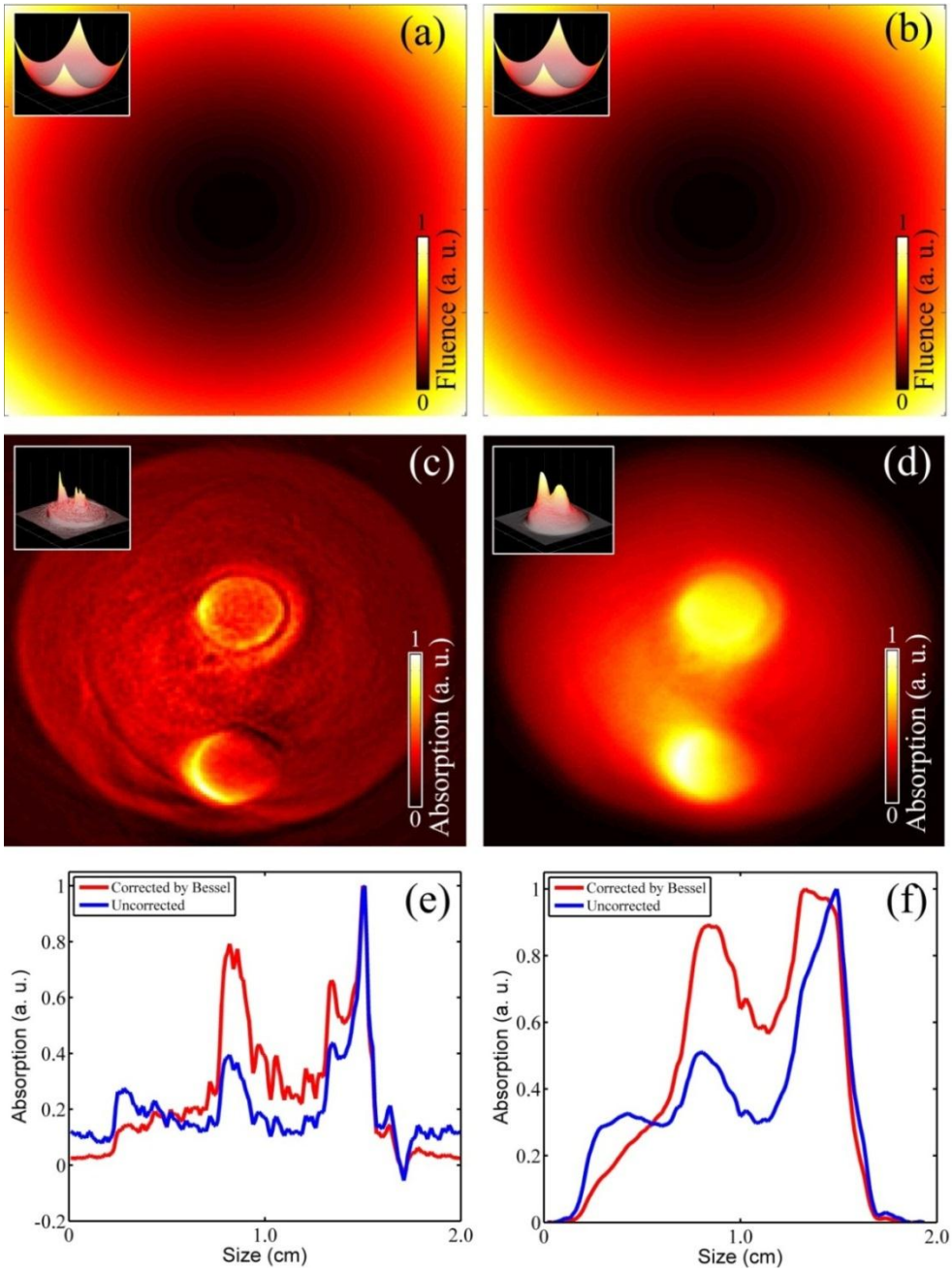

Figure 49: (a) two dimensional Bessel function used to correct for the light attenuation, used for back-projection based reconstruction (b) two dimensional Bessel function used to correct for the light attenuation; used for IMMI based reconstruction (c) Normalized optoacoustic image; reconstructed by back-projection and normalized by the function of (a) (d) Normalized optoacoustic image; reconstructed by IMMI and normalized by the function of (b) (e) profile for corrected and uncorrected back-projection reconstructed optoacoustic images, profile was selected along the dashed line of Figure 47a (f) profile for corrected and uncorrected IMMI reconstructed optoacoustic images, profile was selected along the dashed line of Figure 47a

To further understand the performance of a two dimensional Bessel function for image normalization, the algorithms were tested on the animal dataset. As described in the introduction of this subchapter both images were normalized and afterwards a spectral difference was calculated. The quantification problem is easier compared to the phantom experiment, because in an ideal normalization process all three ICG filled tube should have approximately the same value. To compute the Bessel function, the following parameters were used: radius r = 0.75 cm coefficient k = 230. The resulting two-dimensional analytical fluence is depicted in Figure 50a and it was used to normalize the raw optoacoustic images of Figure 48a/b. The resulting differential image of the normalized optoacoustic images is shown in Figure 50b. It depicts two of the three tubes, but also amplified other regions of the mouse body. These artifacts have approximately the same absorption as the two successfully recovered ICG tubes (Tube 1: 0.89 (a. u.), Tube 2: 1.0 (a. u.)). Unfortunately tube 3 is still not visible in the image. The generation of the artifacts and the missing tube is based on the analytical nature of this normalization scheme. It cannot consider non-cylindrical geometries as well as variations in the optical properties and inhomogeneous illumination scenarios.

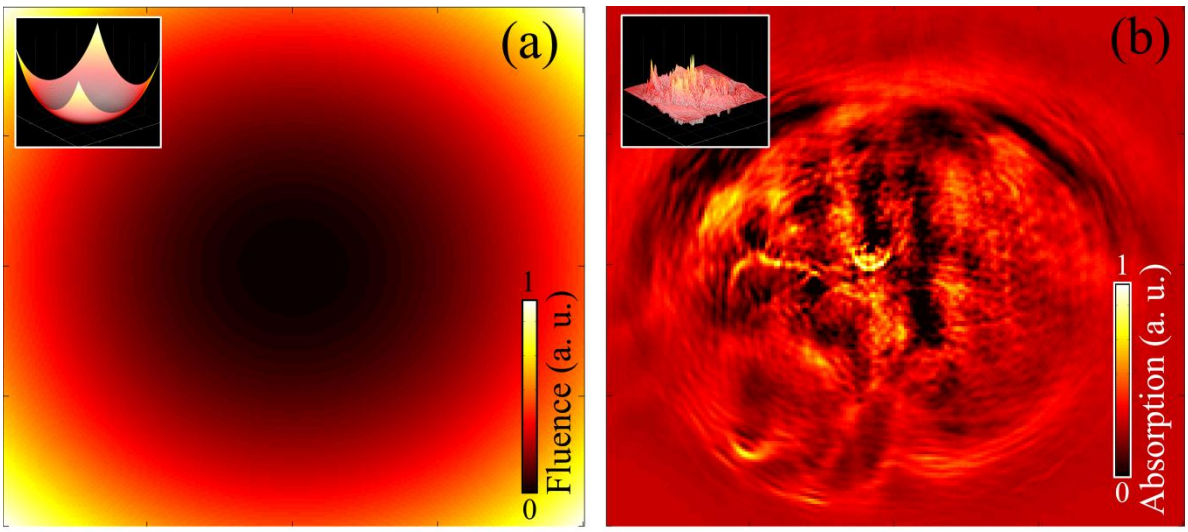

Figure 50: (a) two dimension Bessel function used to normalize the spectral difference image. (b) normalized image using the Bessel function of (a)

5.3.2 Diffusion model-based

Here I tested the performance of a numerical solution of the diffusion approximation based on finite volume solution (FVM) for experimental data. Again the dataset for the tissue mimicking phantom is selected and reconstructed by IMMI and back-projection. Initially the reconstructed image based on back-projection is normalized by equation (4.1) using equation (4.3) to approximate the light fluence U for normalization (Figure 51a). A reconstructed optoacoustic image was thresholded to acquire the geometry necessary to model the FVM mesh. To model the light fluence a reduced scattering coefficient of $\mu_s' = 10$ cm^{-1} and an absorption coefficient of $\mu_a = 0.4$ cm^{-1} were assumed for the background. The normalization of the raw optoacoustic image (Figure 47c) is shown in Figure 51c. Both insertions seem to yield the same signal strength. A plot along the dashed line reveals a similar result as for the Bessel function, where the central lesion is still weaker than the boundary lesion (Figure 51e). The advantage of a numerical solution for the diffusion approximation is, that no guessing of the coefficient k of equation (4.2) is necessary to model the light fluence. This is only valid as long as the optical properties are known for the background. The IMMI based reconstructions show again the same performance as the normalization for the based on back-projected reconstructions (Figure 51d/Figure 51f).

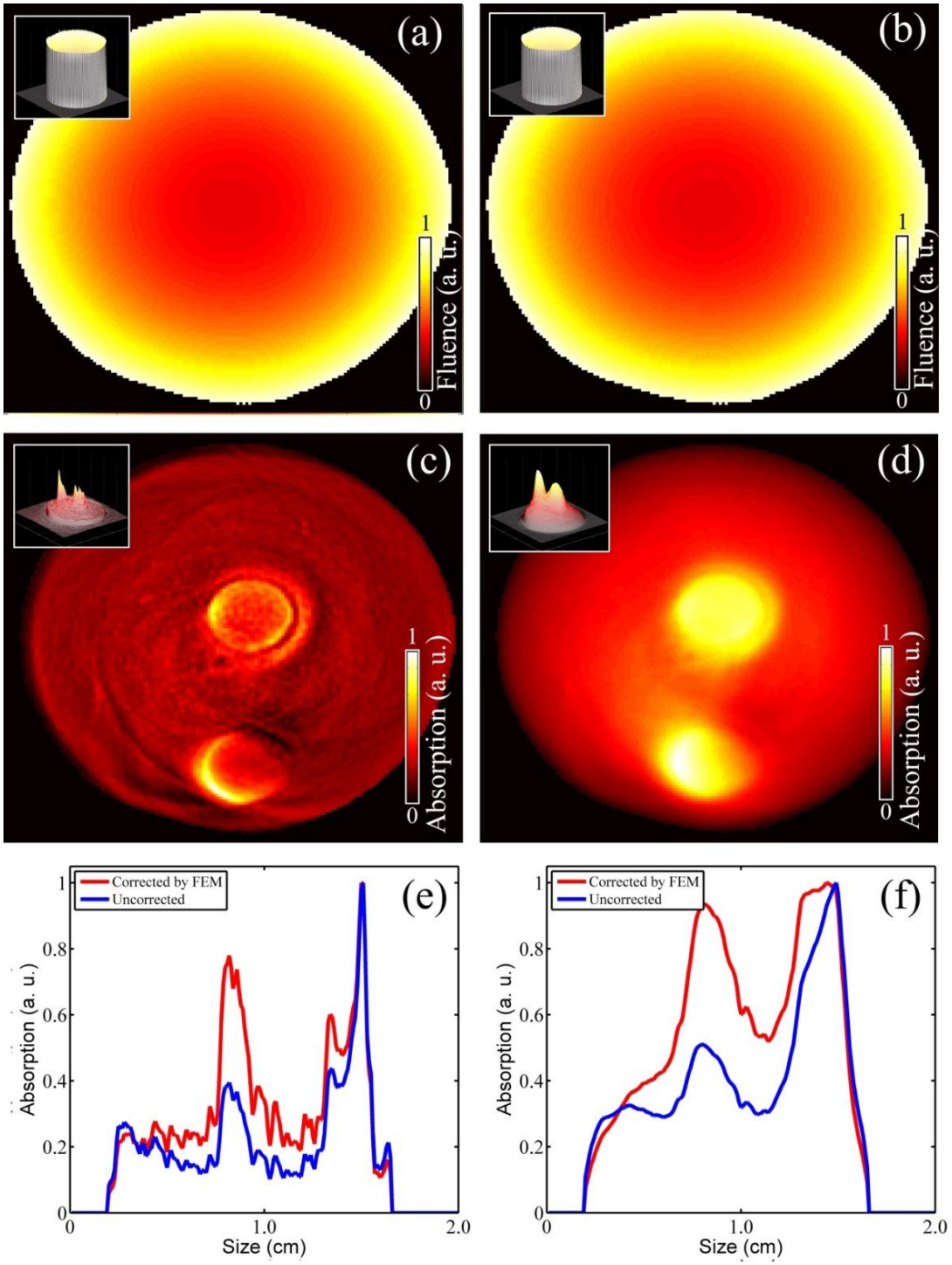

Figure 51: (a) fluence model used to normalize the back-projection image (b) fluence model used to normalize the IMMI image (c) Normalized optoacoustic image; reconstructed by back-projection and normalized by the function of (a) (d) Normalized optoacoustic image; reconstructed by IMMI and normalized by the function of (b) (e) profile for corrected and uncorrected back-projection reconstructed optoacoustic images, profile was selected along the dashed line of Figure 47a (f) profile for corrected and uncorrected IMMI reconstructed optoacoustic images, profile was selected along the dashed line of Figure 47a (Reprinted with permission from [74]. Copyright 2011, Optical Society of America)

The algorithm was also tested on the animal dataset. The geometry for the FVM mesh was approximated by a circular shape because a closed form is very difficult to extract from an animal experiment made in the MSOT II system. In MSOT II images contain artifacts due to its limited view. The detection geometry does not correspond to real light fluence and makes it difficult to extract the exact geometry. Average optical properties of tissue were selected according to the literature [1, 7]. A scattering coefficient of $\mu_s' = 10$ cm^{-1} and an absorption coefficient of $\mu_a = 0.2$ cm^{-1} were assumed for the background. These properties also being used in other optical imaging modalities like FMT [12].

Here the method showed a performance comparable to the analytical approach (Figure 52). Again artifacts were generated, which have approximately the same absorption as the two successfully recovered ICG tubes (Tube 1: 0.95 (a. u.), Tube 2: 1.0 (a. u.)). Unfortunately tube 3 is again not visible in the image. The generation of the artifacts and the missing tube is based on the assumption of a homogeneous optical background absorption and scattering.

Nevertheless a numerical solution to model the light fluence holds several advantages compared to pure analytical methods. It can model any kind of geometry; it can take into account inhomogeneous illumination scenarios and has in general a more physically correct behavior. However, image normalization for a quantitative probe recovery is still a problem in complex scenarios.

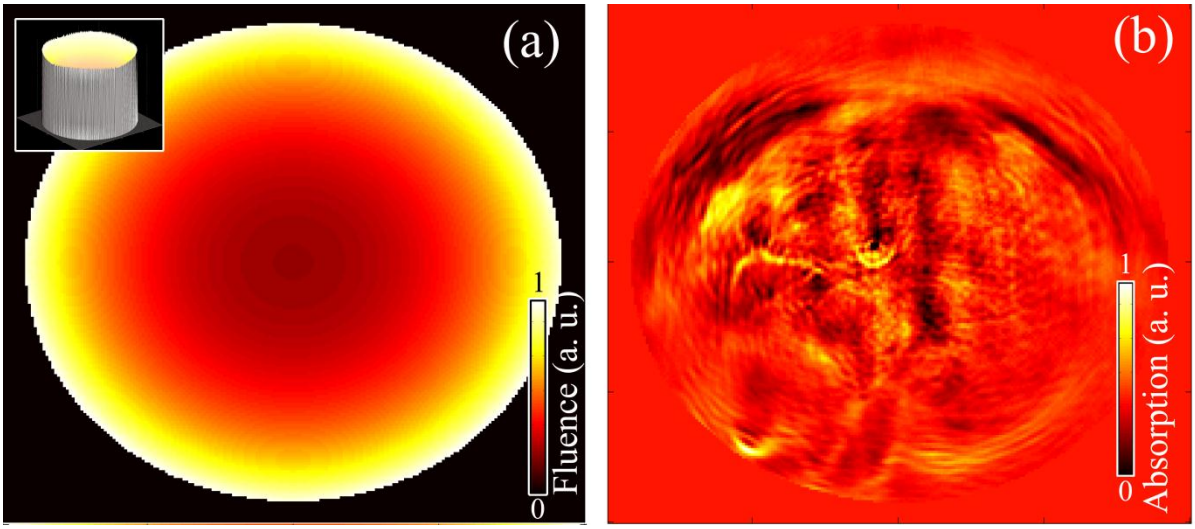

Figure 52: (a) two dimension Bessel function used to normalize the spectral difference image. (b) normalized image using the Bessel function of (a)

5.3.3 Iterative approach

To evaluate the performance of the iterative normalization algorithm I applied it again to the experimental dataset of the phantom and animal with the implanted ICG tubes. Throughout for the iterative procedure it was assumed that the absorption coefficient of the surface is known. This information is used to model the initial homogeneous fluence model for the background with finite volume methods. For practical cases this value can be obtained by the literature or measured with a spectroscope.

The initial optoacoustic image of the phantom was obtained by applying the back-projection algorithm to the measured acoustic signals and is shown in Figure 47c. It can clearly be seen that the light attenuation causes the region of the insertion closer to the phantom boundary to be accentuated. For the first-step improvement, the phantom‘s boundary was extracted and a theoretical fluence was computed assuming homogenous properties (μ_a = 0.4 cm^{-1} and μ_s = 10 cm^{-1}). The resulting fluence is showcased in Figure 53a with the corresponding normalized reconstruction in Figure 53d, which clearly shows that, although the fluence was calculated for only an approximated absorption map, it considerably improves the visual quality of the image. Consequently, the OAT image was also normalized using the iterative algorithm with the following parameters: μ_s = 10 cm^{-1} and σ=0.001. The fluence distribution along with the corrected images at the 1st, 4th and 7th iterations of the algorithm are shown in Figure 53 a/d, b/e, and c/f, respectively. For a better understanding of the performance of the algorithm, profiles along the dashed line of Figure 47a are given (Figure 53g-i). The results show that visual and quantitative improvements were obtained for the first few iterations only. However, as the number of iterations increased, the visual quality of the images decreased. Possible reasons are noise and other artifacts in the reconstructed optoacoustic images as well as discrepancies between the real light fluence and the modeled fluence. these artifacts are naturally amplified throughout the iterations.

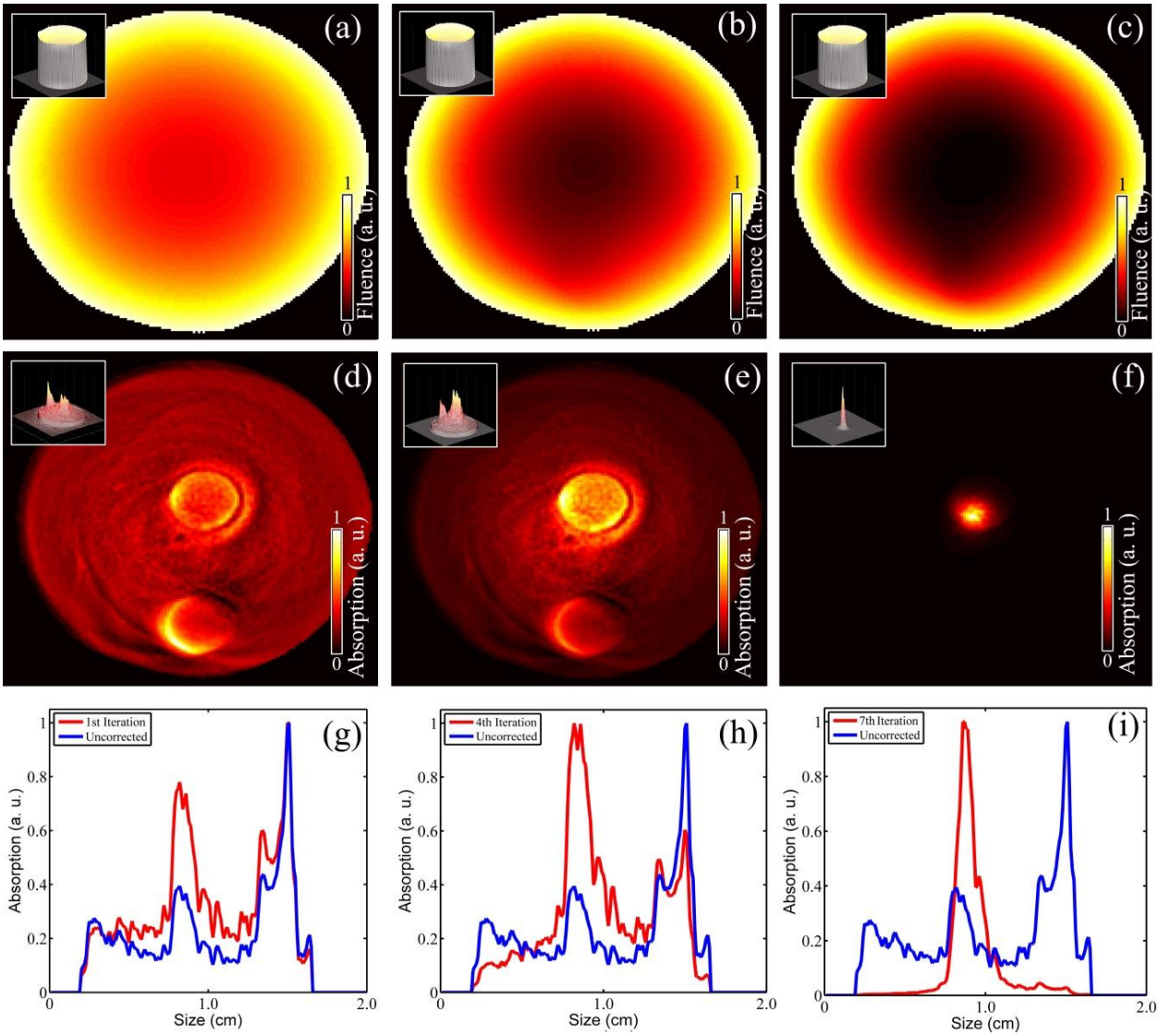

Figure 53: Normalization for back-projection reconstructed images: light fluence modeled for the (a) 1st iteration, (b) for the 4th iteration and (c) for the 7th iteration (c) OAT image normalized by fluence 1st(d), 4th(e) and 7th(f) iteration of the normalization algorithm; (g)profile for corrected and uncorrected optoacoustic images for the 1st iteration, (h) the 4th iteration and (i) the 7th iteration; all profiles were selected along the dashed line of Figure 47a(the red graph shows the corrected profile the blue graph is the uncorrected profile)

Again the IMMI based reconstructions show the same performance as the back-projection based reconstructions (Figure 54). All these results demonstrate that, potentially, iterative image normalization based on finite-element modeling of excitation light propagation can greatly improve the quality and overall quantification performance of the optoacoustic images in the presence of highly inhomogeneous light distribution.

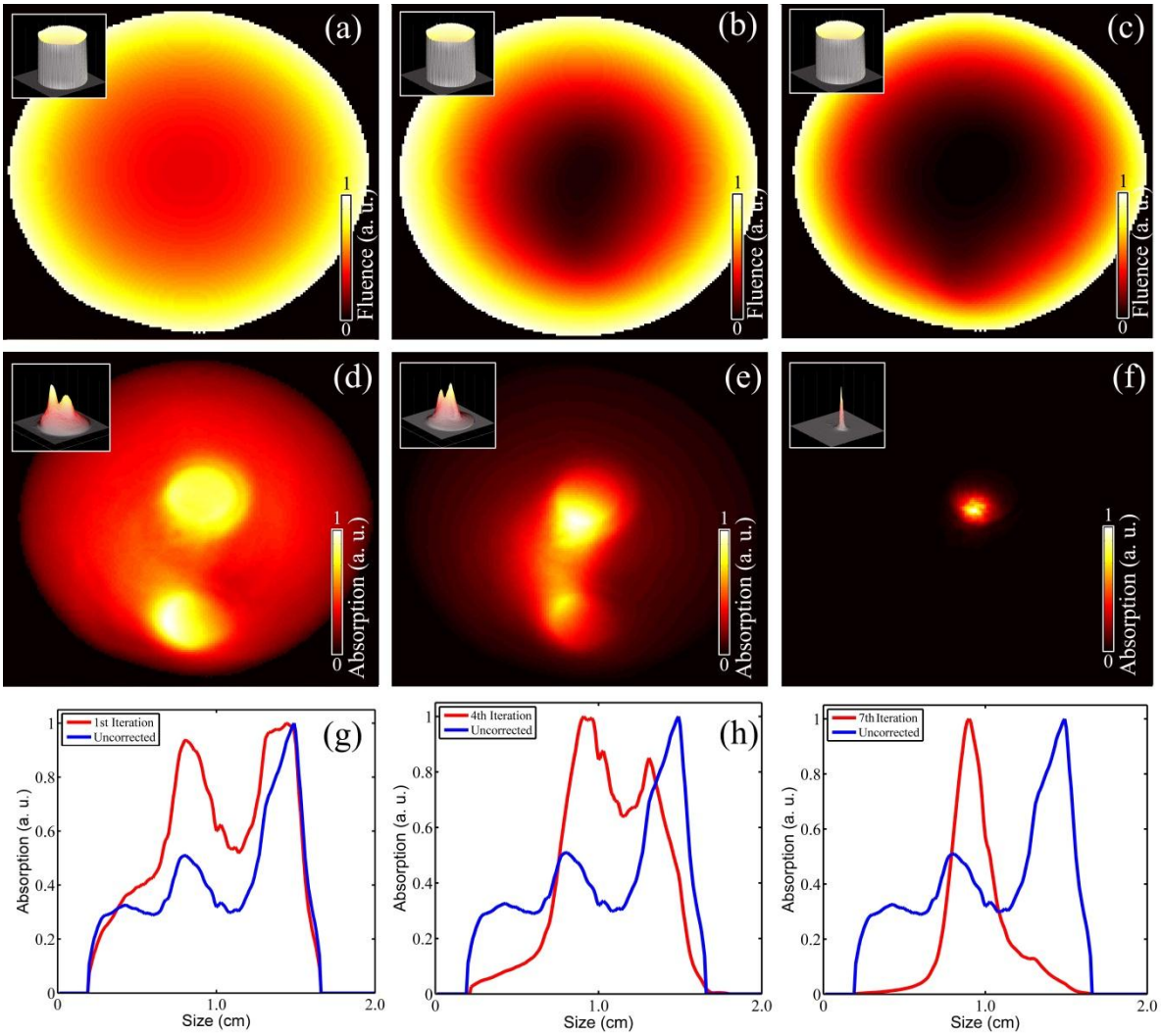

Figure 54 Normalization for IMMI reconstructed images: light fluence modeled for the (a) 1st iteration, (b) for the 4th iteration and (c) for the 7th iteration (c) OAT image normalized by fluence 1st(d), 4th(e) and 7th(f) iteration of the normalization algorithm; (g)profile for corrected and uncorrected optoacoustic images for the 1st iteration, (h) the 4th iteration and (i) the 7th iteration; all profiles were selected along the dashed line of Figure 47a

However, its robustness is highly dependent on both image irregularities (e.g. noise, reconstruction artifacts etc) as well as the selection of parameters assumed in the light distribution modeling steps Ref. [70]. As a result, the quality of the normalized image will normally improve only for the first few iterations. Although the use of a regularization parameter can increase robustness, as it prevents the normalized image from diverging at high iterations, it still cannot assure ideal and robust quantification performance for all different realistic imaging scenarios. These problems are more dominant in animal images, because the variations of the optical properties of the background are much higher. Figure 55 shows, that

no improvement could be achieved beyond the first iteration, which corresponds to the results of previous subchapter. The reason is also, that an animal has a highly heterogeneous structure in terms of optical properties. As stated in the previous subchapter it is also difficult to model exactly the surface and the beam profile in the employed setups. These errors are naturally amplified during the iterative process, which results in heavily biased fluence models corrupting the images in higher iterations.

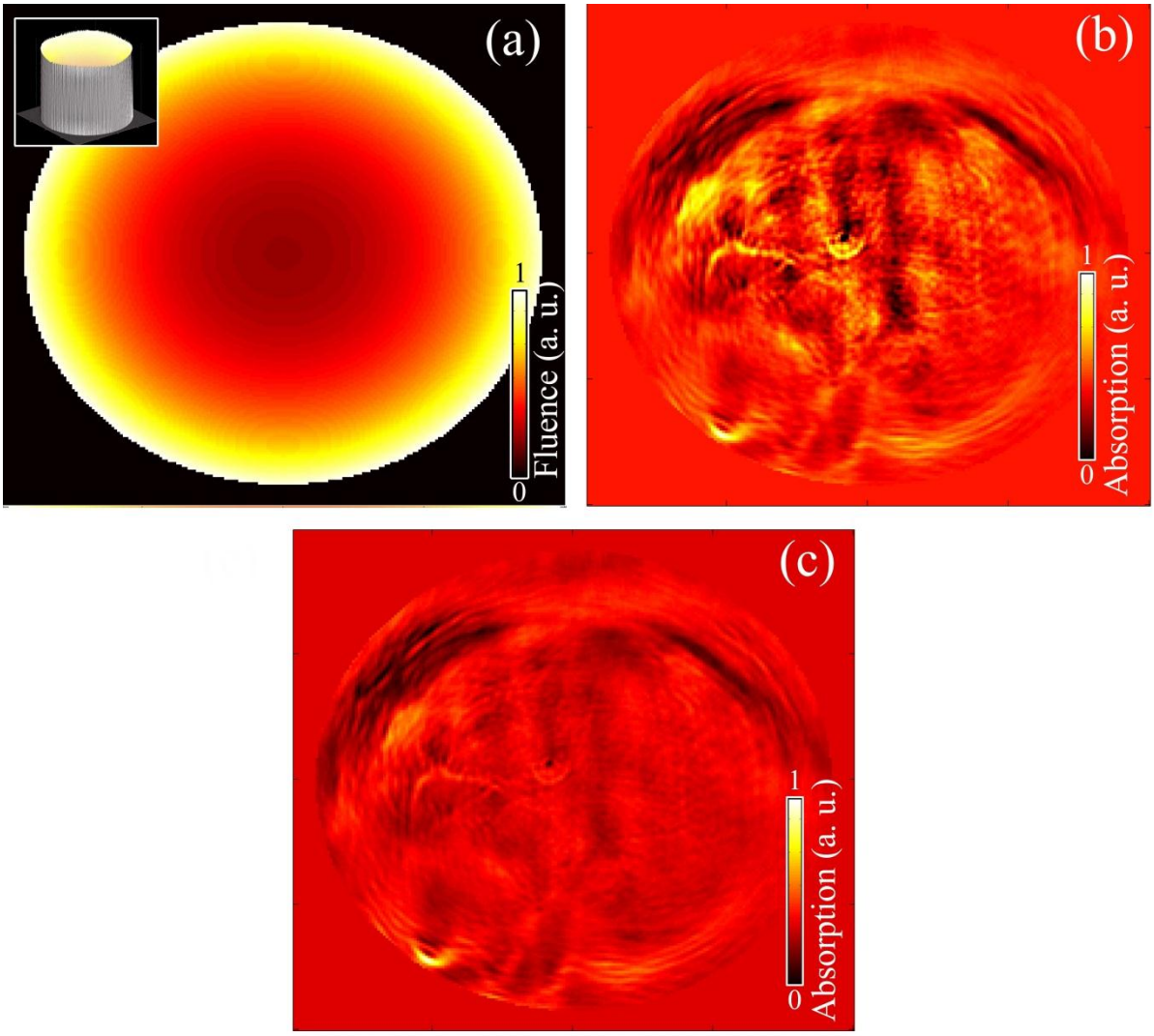

Figure 55: Normalization for IMMI reconstructed animal images (a) light fluence model for the 1st iteration, (b) corrected optoacoustic image using (a) (c) third iteration showing a decrease in image quality.

5.3.4 Normalization by spectral means

The previous chapters demonstrated the disadvantages of analytical and numerical models to correct for the light attenuation. My suggested ratiometric approach promises a better performance by avoiding analytical and numerical models. No additional assumption about unknown scattering coefficients, inhomogeneous illumination or the geometry of the measured object must be made. This method has its limitation, especially when the background itself has a strong spectral dependence. Therefore this method works best in the near infrared region (NIR), where the absorption spectrum is relatively flat.

The proposed method is again tested for the phantom dataset. The properties for the phantom are briefly repeated. The phantom contained two round inclusions with reduced scattering coefficient of $\mu_s' = 10\ cm^{-1}$. The lesion close to the boundary had an absorption coefficient of $\mu_a = 2.2\ cm^{-1}$ at $\lambda_1 = 580$ nm and $\mu_a = 2.4\ cm^{-1}$ at $\lambda_2 = 560$ nm whereas the lesion at the center attained $\mu_a = 2.2\ cm^{-1}$ and 2.6 at $\lambda_1 = 580$ nm, 560 nm respectively. Images were reconstructed using the recently introduced interpolated model-matrix inversion (IMMI) algorithm [31] and the back-projection algorithm. Figure 47c/d show the reconstructed optoacoustic image for $\lambda_{1/2}$ using the back-projection inversion scheme. Figure 56a shows the difference between the two back-projection reconstructed images for $\lambda_{1/2}$. Even for the huge noise level of the difference image the bias introduced by the light attenuation is visible. By using the ratiometric approach an improvement could be observed as showcased in Figure 56b. The improvement can only be seen on a close inspection of the corrected images, shown in profiles along the dashed line of Figure 47a in Figure 56f. The high noise level of back-projection reconstructed images makes it difficult to apply the ratiometric approach to optoacoustic images. Image reconstruction artifacts and the erroneous low frequency components of back-projected images are also amplified by the ratiometric normalization scheme resulting in a bad signal to noise ratio.

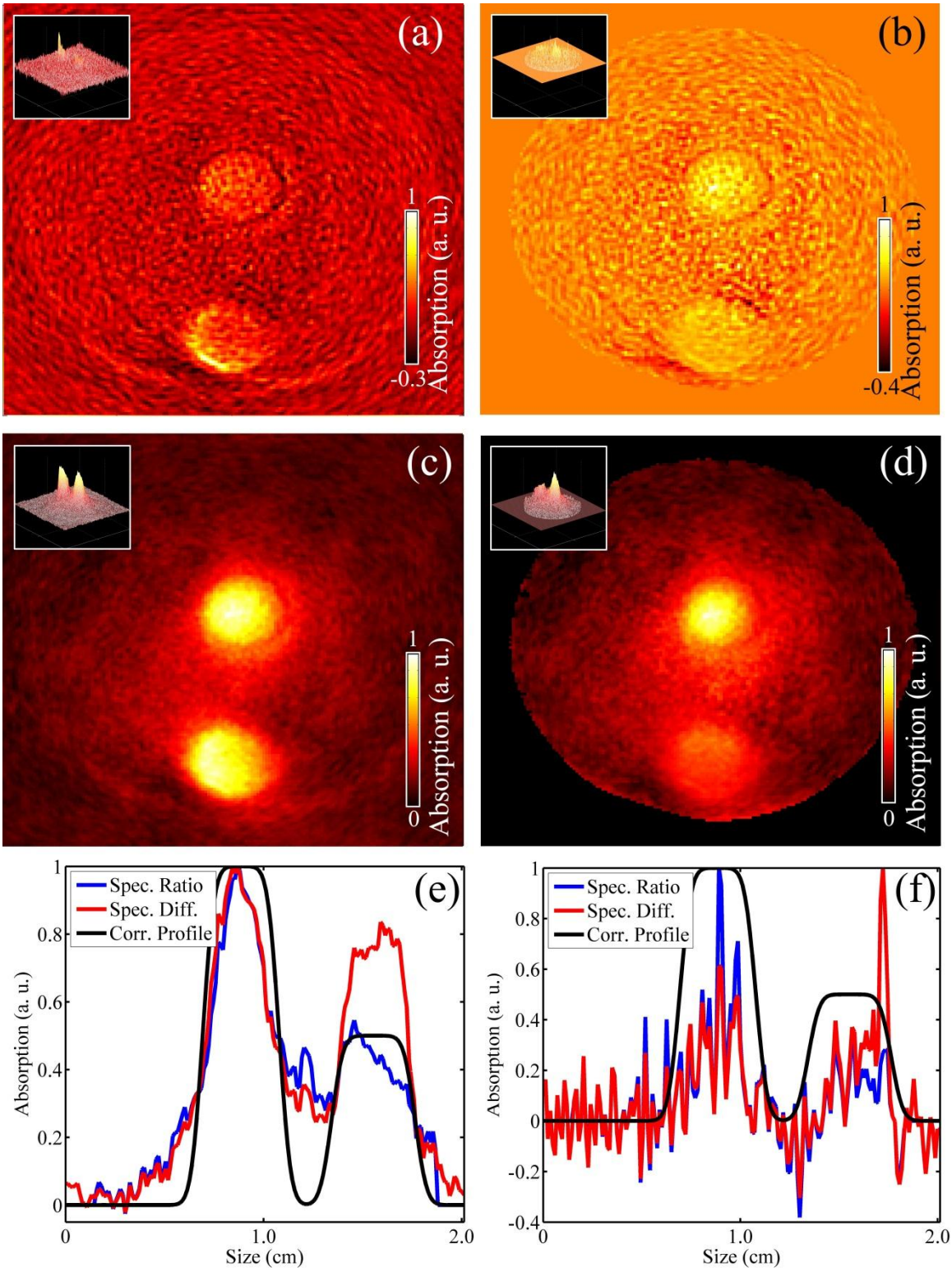

Figure 56: Experimental measurements from a tissue mimicking phantom (a) Spectral difference and (b) spectral ratio using the back-projection method. (c) Spectral difference and (d) spectral ratio using the IMMI method (e) plot along the dashed line of Figure 47a for the IMMI based images (f) plot along the dashed line of Figure 47a for the back-projection based images (Reprinted with permission from [74]. Copyright 2011, Optical Society of America)

In general IMMI reconstructed images show a better performance in terms of visual quality and quantification [75]. By using IMMI on the phantom data, reconstruction artifacts could be significantly reduced. The reconstructed images for both wavelengths are shown in Figure 47e/f for $\lambda_{1/2}$. Following calculation of the spectral difference, it can be seen that the noise level is significantly lower compared to the back-projection images. This is revealed in the form of a better visual image quality due to the effect of the light attenuation in optoacoustic tomography. While the central insertion was of higher absorption, the insertion close to the boundary appears of similar absorption on the difference image (Figure 56c). In contrast, the ratio image shown on Figure 56d accurately reveals the correct concentration of absorption in the two insertions. To show the performance of the ratiometric algorithm in more detail for IMMI and back-projection, profiles along the dashed line of Figure 47a are again provided (Figure 56e). The profiles of the ratiometric corrected images based on IMMI reveal the correct probe concentration of the phantom´s lesions (Figure 56e). The spectral difference based on IMMI shows more clearly the bias caused by the light attenuation (Figure 56c). The corresponding profiles for back-projection contain a high noise level, which makes it difficult to detect the real probe concentration (Figure 56f).

Finally, the acquired mouse data with the *post-mortem* implanted tubes containing Indocyanine Green (ICG) of μ_a = 1.6 cm^{-1} at λ= 800nm (Figure 48) were normalized by spectral ratio to examine it for complex objects. Imaging was performed by using the MSOT II systems as described in Ref. [36]. Images were acquired at 800 nm and 880nm, where ICG has no relevant absorption.

Figure 57a/b depict the spectral difference and the spectral ratio images respectively. The tube close to the surface of the mouse is visible on Figure 57a, however the other two deeper seated tubes are barely visible. In contrast, the spectral ratio image clearly identifies all three

tubes, as shown in the profiles in Figure 57c. Figure 57d superimposes the tubes on the anatomical mouse image.

In conclusion, the ratio method proposed herein offers a simple but efficient method to correct for a challenging aspect of volumetric optoacoustic imaging, namely the depth-dependent light attenuation. The method improves the reconstruction accuracy by using information on optical fluence heterogeneity already contained in the experimental measurements. In this manner, the ratio method offers an effective alternative to correction methods that propose the use of complex calculations for fluence estimation inside tissues. Theoretical estimation of photon fluence may amplify the errors in the image due to the general unavailability of accurately determined optical absorption and scattering properties inside complex optically diffusive media such as tissues. The proposed ratio method has nevertheless inherent limitations. Being a ratio method it may increase the noise in the resulting image. For this reason, it was shown that the use of physically accurate inversion methods, such as IMMI [31], are important for the efficient application of the method.

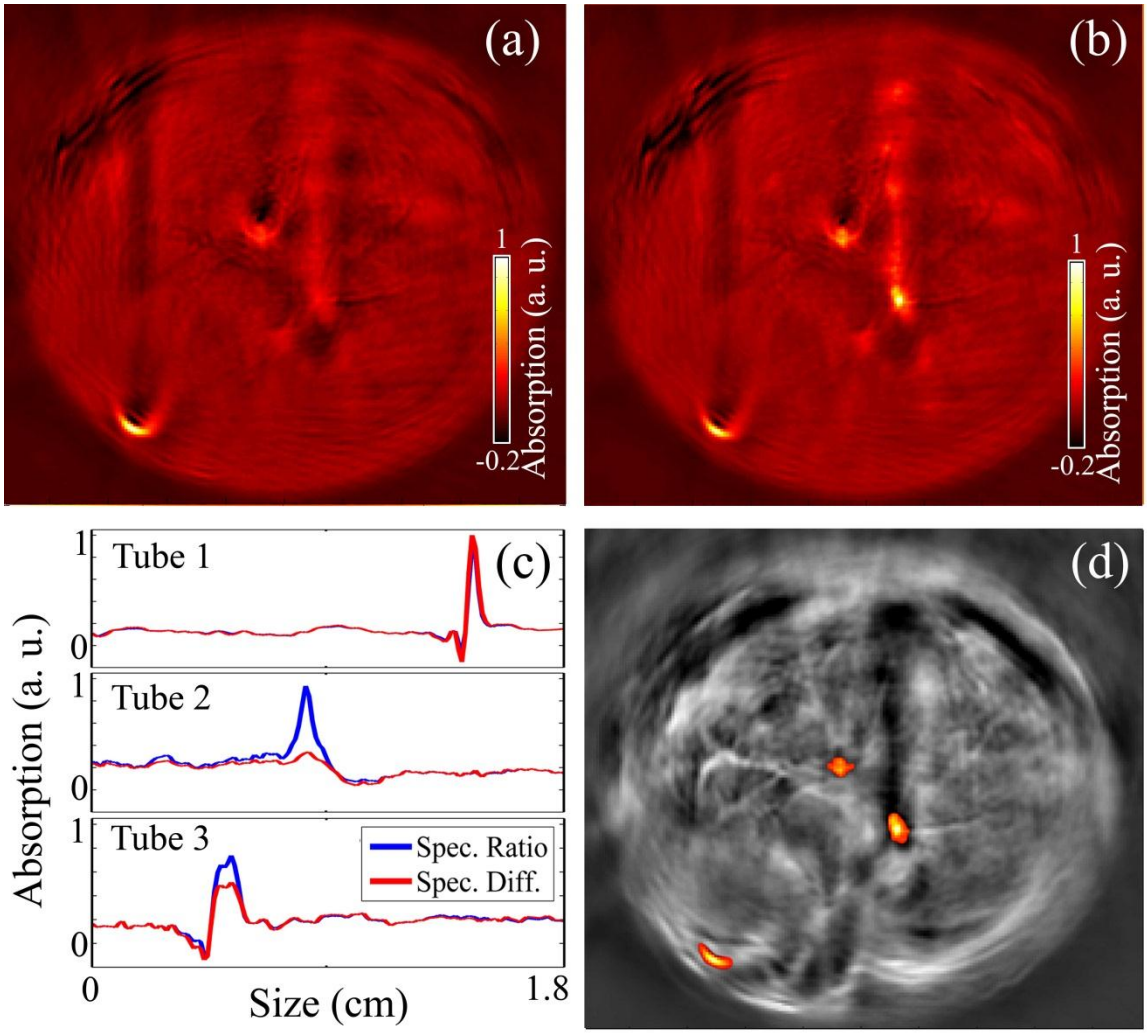

Figure 57: (a) spectral difference (b) spectral ratio (c) profiles along the dashed lines of Figure 48a (d) superimposed image of (d) on (a) after application of a threshold at I=0.5 (Reprinted with permission from [74]. Copyright 2011, Optical Society of America).

6. Discussion and Outlook

6.1 Discussion

Optoacoustic tomography is a promising imaging modality providing ultra-sound resolution with optical contrast. It covers the macroscopic, mesoscopic and microscopic ranges and allows imaging of anatomical, functional and molecular targets in real-time at several wavelengths. The strength of the measured acoustic responses is directly related to the laser power reaching optical absorbers. This dependence introduces quantification issues, when the surface illumination is not homogeneous and in situations where light attenuation is present.

This work presents methods for correcting for the influence of inhomogeneous surface illumination and light attenuation for optoacoustic tomography. The algorithms were examined for simulations, phantom and animal experiments.

For the first time, to the author‘s best knowledge, a comparative study between methods for the correction of the light attenuation in optoacoustic tomography is also given in consideration of image reconstruction artifact-related issues introduced by the used inversion scheme. It is again shown that the commonly used back-projection algorithm is artifact-rich and should not be used in situations where quantification with high sensitivity is desired. The identified artifacts are negative absorption, arc artifacts and meaningless textures, which massively reduce the ability to quantify optoacoustic images. The source of this problem was also identified, and it relates to the pure analytical description of the sound propagation and the not correct treatment of low frequency components in back-projection. The recently introduced IMMI algorithm in general shows a better performance in terms of visual quality and quantification. Modification can be easily introduced in the IMMI approach covering additional experimental parameters.

The showcased methods for image normalization were studied in detail for simulated data, phantom and animal experiments. In simulations where all parameters are known, all methods show a good performance. For experimental data the performance of methods using analytical or numerical descriptions for the light fluence is lower. The sensitivity of these methods suffers from unknown experimental parameters or physical properties of the imaged target. These methods show a comparable quality for back-projection and IMMI based reconstructions. To overcome the limitations inherited by using diffusion models, a ratiometric approach was presented. It can resolve small concentrations of molecular probes in difficult imaging scenarios. Also, it provides a good sensitivity by not relaying on analytical or numerical descriptions of the light fluence. It relies on an artifact-free description of the light fluence acquired by multispectral optoacoustic tomography on different wavelengths. The artifact-free reconstructions are provided by the recently introduced IMMI method. Back-projected images can also be used for the ratiometric approach, though they provide much less image quality. The ratiometric method holds also limitations. It can only correct for the spectrally independent light fluence and therefore works best in the near infrared spectrum. To minimize errors related to spectral variations of the background, there is a need for molecular dyes with a sharp absorption peak and no absorption at other wavelengths.

Nevertheless, all shown methods can be used for normalization of light attenuation. Analytical and numerical methods can be used in less sensitive scenarios to increase the visual quality and quantification of reconstructed images. The ratiometric algorithm fits best for sensitive scenarios where other methods fail. It can be used as long as the target is small so that the contribution of the spectrally dependent light fluence is negligible.

6.2 Outlook

Optoacoustic tomography is a young imaging modality in the field of biomedical research which provides high resolution and good contrast. Due to the direct relationship of the acoustic response and light absorption, optoacoustic tomography holds great promise for quantification. Additionally, the introduction of multispectral optoacoustic tomography has opened the door for more detailed investigations. One of the most challenging aspects of optoacoustic tomography is still the correction of illumination-inherited side effects. This work showed methods to correct for these effects.

Nevertheless this is only a first step to fully quantitative optoacoustic images. There is still a need to better characterize and model the components used in the experimental setup. IMMI provides the necessary basis allowing the modeling of experimentally-related effects like the inhomogeneous surface illumination. The attenuation of high acoustic frequencies must be accounted for, especially for high resolution microscopic images and signals traveling long distances through tissue.

Although the presented implementation of IMMI provides a good performance, it is only a two-dimensional solution for solving the problem of optoacoustic imaging. Future three-dimensional implementations of IMMI would provide a better ability to quantify molecular targets. This can be achieved my modeling transducer characteristics in three dimensions or the surface illumination for the whole volume. Only by covering all experimental setup-related biasing effects in optoacoustic tomography can there be a true quantification of molecular targets.

7. References

[1] V. Ntziachristos, *et al.*, *Textbook of in vivo imaging in vertebrates*. Chichester, England ; Hoboken, NJ: J. Wiley & Sons, 2007.

[2] V. Ntziachristos, "Going deeper than microscopy: the optical imaging frontier in biology," *Nat Methods,* vol. 7, pp. 603-14, Aug 2010.

[3] S. J. Gould, *The lying stones of Marrakech : penultimate reflections in natural history*, 1st ed. New York: Harmony Books, 2000.

[4] R. K. Jain, *et al.*, "Dissecting tumour pathophysiology using intravital microscopy," *Nature Reviews Cancer,* vol. 2, pp. 266-276, Apr 2002.

[5] A. F. Fercher, *et al.*, "In vivo optical coherence tomography," *Am J Ophthalmol,* vol. 116, pp. 113-4, Jul 15 1993.

[6] M. Wojtkowski, *et al.*, "In vivo human retinal imaging by Fourier domain optical coherence tomography," *Journal of Biomedical Optics,* vol. 7, pp. 457-463, Jul 2002.

[7] V. Ntziachristos, *et al.*, "Small-animal optical imaging," *J Biomed Opt,* vol. 13, p. 011001, Jan-Feb 2008.

[8] V. Ntziachristos, *et al.*, "Fluorescence imaging with near-infrared light: new technological advances that enable in vivo molecular imaging," *Eur Radiol,* vol. 13, pp. 195-208, Jan 2003.

[9] V. Ntziachristos and R. Weissleder, "Experimental three-dimensional fluorescence reconstruction of diffuse media by use of a normalized Born approximation," *Opt Lett,* vol. 26, pp. 893-5, Jun 15 2001.

[10] V. Ntziachristos, *et al.*, "In vivo tomographic imaging of near-infrared fluorescent probes," *Mol Imaging,* vol. 1, pp. 82-8, Apr-Jun 2002.

[11] V. Ntziachristos, *et al.*, "Fluorescence molecular tomography resolves protease activity in vivo," *Nature Medicine,* vol. 8, pp. 757-760, July 2002.

[12] A. Ale, *et al.*, "Imaging performance of a hybrid x-ray computed tomography-fluorescence molecular tomography system using priors," *Med Phys,* vol. 37, pp. 1976-86, May 2010.

[13] R. B. Schulz, *et al.*, "Hybrid system for simultaneous fluorescence and x-ray computed tomography," *IEEE Trans Med Imaging,* vol. 29, pp. 465-73, Feb 2010.

[14] J. Sharpe, "Optical projection tomography," *Annu Rev Biomed Eng,* vol. 6, pp. 209-28, 2004.

[15] D. A. Boas, *et al.*, "Imaging the body with diffuse optical tomography," *Ieee Signal Processing Magazine,* vol. 18, pp. 57-75, Nov 2001.

[16] A. A. Oraevsky, *et al.*, "Laser based optoacoustic imaging in biological tissues," *Proc. SPIE,* vol. 2134A, pp. 122-128, 1994.

[17] R. A. Kruger, "Photoacoustic ultrasound (PAUS)—Reconstruction tomography," *Medical Physics,* vol. 22, p. 1605 1995.

[18] L. Wang, *Photoacoustic imaging and spectroscopy*: CRC Press 2009.

[19] V. Ntziachristos and D. Razansky, "Molecular Imaging by Means of Multispectral Optoacoustic Tomography (MSOT)," *Chemical Reviews,* vol. 110, pp. 2783-2794, 2010.

[20] A. Rosencwaig, "Photoacoustics and Photoacoustic Spectroscopy," *Chemical Analysis,* p. 12, 1980.

[21] A. Rosencwaig and A. Gersho, "Theory of the photoacoustic effect with solids," *Journal of Applied Physics,* vol. 47, pp. 64-69, 1976.

[22] P. A. Fomitchov, *et al.*, "Photoacoustic Probes for Nondestructive Testing and Biomedical Applications," *Appl. Opt.,* vol. 41, pp. 4451-4459, 2002.

[23] X. Wang, *et al.*, "Photoacoustic tomography of biological tissues with high cross-section resolution: Reconstruction and experiment," *Medical Physics,* vol. 29, p. 2799 2002.

[24] A. A. Oraevsky, *et al.*, "Laser-based optoacoustic imaging in biological tissues," *Proc. SPIE,* vol. 2134A, pp. 122-128, 1994.

[25] C. Bremer, *et al.*, "Optical-based molecular imaging: contrast agents and potential medical applications," *Eur Radiol,* vol. 13, pp. 231-43, Feb 2003.

[26] K. P. Köstli, *et al.*, "Temporal backward projection of optoacoustic pressure transients using Fourier transform methods," *Physics in Medicine and Biology,* vol. 46, pp. 1863-1872 2001.

[27] M. Jaeger, *et al.*, "Fourier reconstruction in optoacoustic imaging using truncated regularized inverse k-space interpolation," *Inverse Problems,* vol. 23, pp. S51-S63 2007.

[28] H. Jiang, *et al.*, "Spatially varying optical and acoustic property reconstruction using finite-element-based photoacoustic tomography," *Journal of the Optical Society of America A,* vol. 23, pp. 878-888, 2006.

[29] M. Xu and L. V. Wang, "Universal back-projection algorithm for photoacoustic computed tomography," *Physical Review E,* vol. 71, 2005.

[30] G. Paltauf, *et al.*, "Iterative reconstruction algorithm for optoacoustic imaging," *The Journal of the Acoustical Society of America,* vol. 112, p. 1536 2002.

[31] A. Rosenthal, *et al.*, "Fast semi-analytical model-based acoustic inversion for quantitative optoacoustic tomography," *IEEE Transactions on Medical Imaging,* vol. 29, pp. 1275-1285, 2010.

[32] T. Jetzfellner, *et al.*, "Optoacoustic tomography with varying illumination and non-uniform detection patterns," *J Opt Soc Am A Opt Image Sci Vis, Under Review,* 2010.

[33] J. Laufer, *et al.*, "Quantitative spatially resolved measurement of tissue chromophore concentrations using photoacoustic spectroscopy: application to the measurement of blood oxygenation and haemoglobin concentration," *Physics in Medicine and Biology,* vol. 52, pp. 141-168, 2007.

[34] J. Jose, *et al.*, "Imaging of tumor vasculature using Twente photoacoustic systems," *Journal of Biophotonics,* vol. 2, pp. 701-717, Dec 2009.

[35] L. Song, *et al.*, "Section-illumination photoacoustic microscopy for dynamic 3D imaging of microcirculation in vivo," *Optics letters,* vol. 35, pp. 1482-1484, May 1 2010.

[36] A. Buehler, *et al.*, "Video rate optoacoustic tomography of mouse kidney perfusion," *Opt Lett,* vol. 35, pp. 2475-7, Jul 15 2010.

[37] A. Taruttis, *et al.*, "Real-time imaging of cardiovascular dynamics and circulating gold nanorods with multispectral optoacoustic tomography," *Opt. Express,* vol. 18, pp. 19592-19602, 2010.

[38] L. Li, *et al.*, "Photoacoustic imaging of lacZ gene expression in vivo," *J Biomed Opt,* vol. 12, p. 020504, Mar-Apr 2007.

[39] D. Razansky, *et al.*, "Multispectral photoacoustic imaging of fluorochromes in small animals," *Optics Letters,* vol. 32, p. 2891 2007.

[40] D. Razansky, *et al.*, "Multispectral opto-acoustic tomography of deep-seated fluorescent proteins in vivo," *Nat Photon,* vol. 3, pp. 412-417, 2009.

[41] A. G. Bell, "The Production of Sound by Radiant Energy," *Science,* vol. 2, pp. 242-53, May 28 1881.

[42] J. R. Albani, *Structure and Dynamics of Macromolecules: Absorption and Fluorescence Studies*. Lille: ELSEVIER, 2004.

[43] R. Kneuer, *et al.*, *In Vivo Fluorescence Optical and Multi-Modal Imaging in Pharmacological Research: From Chemistry to Therapy Monitoring* vol. Biomedical Imaging London: Royal Society of Chemistry, 2011.

[44] L. B. Kreuzer, "Ultralow Gas Concentration Infrared Absorption Spectroscopy," *Journal of Applied Physics,* vol. 42, pp. 2934-2943, 1971.

[45] V. E. Gusev and A. A. Karabutov, *Laser optoacoustics*. New York: American Institute of Physics 1993.

[46] T. H. Maugh, 2nd, "Photoacoustic spectroscopy: new uses for an old technique," *Science,* vol. 188, pp. 38-9, Apr 4 1975.

[47] A. A. Karabutov, *et al.*, "Time-resolved laser optoacoustic tomography of inhomogeneous media," *Applied Physics B-Lasers and Optics,* vol. 63, pp. 545-563, Dec 1996.

[48] L. H. V. Wang, *et al.*, "Microwave-induced acoustic imaging of biological tissues," *Review of Scientific Instruments,* vol. 70, pp. 3744-3748, Sep 1999.

[49] F. J. M. Harren, *et al.*, *Photoacoustic Spectroscopy in Trace Gas Monitoring*: John Wiley & Sons, Ltd, 2006.

[50] J. A. Giordmaine and R. C. Miller, "Tunable Coherent Parametric Oscillation in LiNbO3 at Optical Frequencies," *Physical Review Letters,* vol. 14, p. 973, 1965.

[51] F. Schäfer, *et al.*, "Organic Dye Solution Laser," *Applied Physics Letters,* vol. 9, 1966.

[52] A. Rosenthal, *et al.*, "Optoacoustic methods for frequency calibration of ultrasonic sensors," *IEEE Transactions on Ultrasonics, Ferroelectrics and Frequency Control,* vol. 58, pp. 316-326, 2011.

[53] A. Rosenthal, *et al.*, "Model-Based optoacoustic inversion with arbitary-shape detectors," *Medical Physics,* vol. 38, p. in print, 2011.

[54] G. J. Diebold, *et al.*, "Photoacoustic monopole radiation in one, two, and three dimensions," *Physical Review Letters,* vol. 67, p. 3384, 1991.

[55] R. Ma, *et al.*, "Multispectral optoacoustic tomography (MSOT) scanner for whole-body small animal imaging," *Opt. Express,* vol. 17, pp. 21414-21426, 2009.

[56] Y. Wang, *et al.*, "Photoacoustic Tomography of a Nanoshell Contrast Agent in the in Vivo Rat Brain," *Nano Letters,* vol. 4, pp. 1689-1692 2004.

[57] H. P. Brecht, *et al.*, "Whole-body three-dimensional optoacoustic tomography system for small animals," *Journal of Biomedical Optics,* vol. 14, pp. -, Nov-Dec 2009.

[58] X. Wang, *et al.*, "Noninvasive laser-induced photoacoustic tomography for structural and functional in vivo imaging of the brain," *Nature Biotechnology,* vol. 21, pp. 803-806, 2003.

[59] M.-L. Li, *et al.*, "Simultaneous Molecular and Hypoxia Imaging of Brain Tumors In Vivo Using Spectroscopic Photoacoustic Tomography," *Proceedings of the IEEE,* vol. 96, pp. 481-489, 2008.

[60] J. Laufer, *et al.*, "Quantitative spatially resolved measurement of tissue chromophore concentrations using photoacoustic spectroscopy: application to the measurement of blood oxygenation and haemoglobin concentration," *Physics in Medicine and Biology,* vol. 52, pp. 141-168 2006.

[61] R. I. Siphanto, *et al.*, "Serial noninvasive photoacoustic imaging of neovascularization in tumor angiogenesis," *Optics Express,* vol. 13, p. 89 2005.

[62] D. Razansky, *et al.*, "Mesoscopic imaging of fluorescent proteins using multi-spectral optoacoustic tomography (MSOT)," ed. San Jose, CA, USA, 2009, pp. 71770D-71770D-6

[63] M. Luukkala and A. Penttinen, "Photoacoustic microscope," *Electronics Letters,* vol. 15, pp. 325-326, 1979.

[64] H. F. Zhang, *et al.*, "Functional photoacoustic microscopy for high-resolution and noninvasive in vivo imaging," *Nature Biotechnology,* vol. 24, pp. 848-851 2006.

[65] J. J. Niederhauser, *et al.*, "Combined ultrasound and optoacoustic system for real-time high-contrast vascular imaging in vivo," *IEEE Trans Med Imaging,* vol. 24, pp. 436-40, Apr 2005.

[66] A. Dima and V. Ntziachristos, "Optoacoustic imaging for clinical applications: devices and methods," *Expert Opinion on Medical Diagnostics,* vol. 5, pp. 263-272, 2011.

[67] R. G. Kolkman, *et al.*, "Real-time in vivo photoacoustic and ultrasound imaging," *J Biomed Opt,* vol. 13, p. 050510, Sep-Oct 2008.

[68] C. Haisch, *et al.*, "Combined optoacoustic/ultrasound system for tomographic absorption measurements: possibilities and limitations," *Anal Bioanal Chem,* vol. 397, pp. 1503-10, Jun 2010.

[69] C. Kim, *et al.*, "Deeply penetrating in vivo photoacoustic imaging using a clinical ultrasound array system," *Biomed Opt Express,* vol. 1, pp. 278-284, 2010.

[70] T. Jetzfellner, *et al.*, "Performance of iterative optoacoustic tomography with experimental data," *Applied Physics Letters,* vol. 95, pp. 013703-1-013703-3, 2009.

[71] B. T. Cox, *et al.*, "Estimating chromophore distributions from multiwavelength photoacoustic images," *Journal of the Optical Society of America A,* vol. 26, p. 443 2009.

[72] B. T. Cox, *et al.*, "Two-dimensional quantitative photoacoustic image reconstruction of absorption distributions in scattering media by use of a simple iterative method," *Applied Optics,* vol. 45, p. 1866, 2006.

[73] D. Razansky and V. Ntziachristos, "Hybrid photoacoustic fluorescence molecular tomography using finite-element-based inversion," *Medical Physics,* vol. 34, p. 4293, 2007.

[74] T. Jetzfellner*, et al.*, "Multispectral optoacoustic tomography by means of normalized spectral ratio," *Optics Letters, Under Review,* 2011.

[75] T. Jetzfellner*, et al.*, "Interpolated model-matrix optoacoustic tomography of the mouse brain " *Applied Physics Letters,* vol. 98, 2011.

[76] T. Jetzfellner*, et al.*, "Optoacoustic tomography with varying illumination and non-uniform detection patterns," *J Opt Soc Am A Opt Image Sci Vis,* vol. 27, pp. 2488-95, Nov 1 2010.

[77] A. Dima, "A New Model-Based Image Reconstruction Algorithm for Photoacoustic Tomography," Institute for Biological and Medical Imaging, Technische Universität München 2009.

[78] G. Golub, *Matrix computations*. Baltimore: Johns Hopkins University Press, 3rd ed., 1996.

[79] C. C. Paige and M. A. Saunders, "LSQR: An Algorithm for Sparse Linear Equations and Sparse Least Squares," *ACM Trans. Math. Softw.,* vol. 8, pp. 43-71, 1982.

[80] B. T. Cox*, et al.*, "Estimating chromophore distributions from multiwavelength photoacoustic images," *Journal of the Optical Society of America a-Optics Image Science and Vision,* vol. 26, pp. 443-455, 2009.

[81] D. Razansky and V. Ntziachristos, "Hybrid photoacoustic fluorescence molecular tomography using finite-element-based inversion.," *Med Phys,* vol. 34, pp. 4293-301, Nov 2007.

[82] A. Conjusteau*, et al.*, "Characterization of optoacoustic transducers through the analysis of angular-dependent frequency response," *Proc. SPIE,* vol. 7177, pp. 71770-71778, 2009.

[83] R. Ma*, et al.*, "Multispectral optoacoustic tomography (MSOT) scanner for whole-body small animal imaging," *Optics Express,* vol. 17, pp. 21414-21426, 2009.

[84] H. Zhang*, et al.*, "Functional photoacoustic microscopy for high-resolution and noninvasive in vivo imaging.," *Nat Biotechnol,* vol. 24, pp. 848-51, Jul 2006.

[85] P. Burgholzer*, et al.*, "Compensation of acoustic attenuation for high-resolution photoacoustic imaging with line detectors," *Proc. SPIE,* vol. 6437, pp. 643724-1, 2007.

[86] T. Jetzfellner*, et al.*, "Performance of iterative optoacoustic tomography with experimental data," *Applied Physics Letters,* vol. 95, pp. -, JUL 6 2009 2009.

[87] M. Schweiger*, et al.*, "The finite element method for the propagation of light in scattering media: Boundary and source conditions," *Medical Physics,* vol. 22, pp. 1779-1792 1995.

[88] W. Bangerth*, et al.*, "deal. II - A general-purpose object-oriented finite element library," *Acm Transactions on Mathematical Software,* vol. 33, 2007.

[89] A. Rosenthal*, et al.*, "Quantitative Optoacoustic Signal Extraction Using Sparse Signal Representation," *IEEE Transactions on Medical Imaging,* vol. 28, pp. 1997-2006, 2009.

[90] G. Zacharakis, *et al.*, "Fluorescent protein tomography scanner for small animal imaging," *IEEE Transactions on Medical Imaging,* vol. 24, pp. 878-885 2005.

[91] R. A. Kruger, *et al.*, "Thermoacoustic optical molecular imaging of small animals," *Molecular Imaging,* vol. 2, pp. 113-123, 2003.

[92] A. Sarantopoulos, *et al.*, "Imaging the Bio-Distribution of Fluorescent Probes Using Multispectral Epi-Illumination Cryoslicing Imaging," *Mol Imaging Biol,* Sep 14 2010.

8. Appendix

8.1 List of Figures

8.2 List of symbols and abbreviations

8.2.1 Abbreviations

ANSI	American National Standards Institute
BP	Back-projection
CLSM	Confocal laser scanning microscopes
CT	Computer tomography
DOT	Diffuse optical tomography
FEM	Finite element methods
FFT	Fast Fourier transform
fMRT	Functional magnet resonance tomography
FMT	Fluorescence molecular tomography
FVM	Finite volume methods
FWHM	Full width half maximum
Hb	Deoxygenized hemoglobin
HbO2	Oxygenized hemoglobin
ICG	Indocyanine green
IMMI	Interpolated model matrix inversion
LSQR	Least squares QR decomposition
MPE	Maximum permissible exposure
MPLSM	Multiphoton laser scanning microscope
MRT	Magnet resonance tomography

MSOT	Multi spectral optoacoustic tomography
NIR	Near infrared
NIRS	Near infrared spectroscopy
OAT	Optoacoustic tomography
OCT	Coherence tomography
OPO	Optical parametric oscillator
OPT	Optical projection tomography
PAM	Photoacoustic microscopy
PAT	Photoacoustic tomography
PET	Positron emission tomography
PD	Photo diode
PSF	Point spread functions
SPECT	Single-photon emission computed tomography
TAT	Thermoacoustic tomography

8.2.2 General notation

A, …, Z	Matrices
a, …, z	Vectors in $\mathbb{R}^N$, N arbitrary (depending on context)
A^T	Matrix transpose of A
A^{-1}	Matrix inverse of A

8.2.3 Greek symbols

β	Isobaric volume expansion coefficient
δ	Dirac delta function
ε	Measure of the machine precision
λ_c	Acoustic wavelength relating to an optoacoustic source
λ_n	Wavelength of the light, n numbering of the wavelength
μ_a	Absorption coefficient (cm^{-1})
μ_s'	Reduced scattering coefficient (cm^{-1})
κ	Isothermal compressibility
Γ	Grüneisen coefficient
Ω_0	Spatial domain enclosing the imaging target
$\partial\Omega_0$	Boundary of Ω

8.2.4 Latin symbols

A	Spatial absorption function
c	Propagation speed of the pressure wave
C_p	Heat capacity
D	Spatial dependent diffusion coefficient
f_c	Cut off frequency
$\tilde{H}$	Hankel Transform for even functions
$\hat{H}$	Heating function
H	Optoacoustic image
M	Model matrix for IMMI
n_0^s	Vector normal of S_0
O	Origin of the coordinate system
p_0	Initial optoacoustic pressure
p	Measured signals
p^k	Column vector representing the acoustic fields measured for projection k at r_k (k=1…K),
R	Distance between source and detector
r	Arbitary *p*osition in the imaging plane
r'	Position of a specific source in the imaging domain
r_0	Detector position in the imaging plane
S_0	Circular scanning geometry

T	Temperature rise
t	Time
$t´$	Time when heating occurs
U	Photon fluence
u	Unknowns, calculated by matrix inversion
W	Weight matrix

8.3 List of publications

Kneuer R., Gremlich H.-U., Beckmann N., Ntziachristos V., and Jetzfellner T.,
"*In Vivo* Fluorescence Optical and Multi-Modal Imaging in Pharmacological Research: From Chemistry to Therapy Monitoring"
Biomedical Imaging (Book), Royal Society of Chemistry, London, (publication scheduled for October 2011)

Jetzfellner T., and Ntziachristos V.,
"Performance of blind deconvolution in optoacoustic tomography"
Journal of Innovative Optical Health Sciences, under review

Jetzfellner T., Ntziachristos V., Rozenthal A., Englmeier K.-H., and Razansky D.,
"Quantification of molecular probes in optoacoustic tomography using spectral ratio", *Optics Letters, under review*

Jetzfellner T., Rosenthal A., Englmeier K.-H., Razansky D., and Ntziachristos V.,
"Interpolated model-matrix optoacoustic tomography of small animal brain", *Applied Physics Letters (2011),*

Jetzfellner T., Rosenthal A., Buehler A., Dima A., Englmeier K.-H., Ntziachristos V., and Razansky D.,
"Tomographic optoacoustic inversion in dynamic illumination scenarios"
Proceedings SPIE Photonics West (2011)

Rosenthal A., Razansky D., Jetzfellner T., and Ntziachristos V.,
"Fast semi-analytical acoustic inversion for quantitative optoacoustic tomography"
Proceedings SPIE Photonics West (2011)

Buehler A., Rosenthal A., Jetzfellner T., Dima A., Razansky D., and Ntziachristos V.,
"Model-Based Optoacoustic Inversions with Incomplete Projection Data", *Medical Physics 38, 1694 (2011)*

Jetzfellner T, Rosenthal A, Buehler A, Dima A, Englmeier K.-H., Ntziachristos V., and Razansky D.,
"Optoacoustic tomography with varying illumination and non-uniform detection patterns"
Journal of the Optical Society of America A, Vol. 27, Issue 11, pp. 2488-2495 (2010)

Jetzfellner T., Razansky D., Rosenthal A., Schulz R., Englmeier K.-H., and Ntziachristos V.,
"Performance of iterative optoacoustic tomography with experimental data"
Applied Physics Letters. 95, 013703 (2009)

Jetzfellner T., Razansky D., Rosenthal A., Schulz R., Englmeier K.-H., and Ntziachristos V.,
"Iterative finite-element-based inversion for quantified detection of molecular targets using optoacoustic tomography"
Proceedings Vol. 7258, Medical Imaging 2009: Physics of Medical Imaging (2009)

Jetzfellner T., Razansky D., Englmeier K.-H., and Ntziachristos V.,
"Quantification of Molecular probe detection by optoacoustic tomography using a finite-element based inversion."
Proceedings, World Molecular Imaging Conference, 10.-13.09.2008, Nice, France (2008)